Measuring Inflation through Precision Cosmology

Alexey Makarov

A Dissertation
Presented to the Faculty
of Princeton University
in Candidacy for the Degree
of Doctor of Philosophy

Recommended for Acceptance
by the Department of
Physics

September, 2006

Abstract

In this work we study inflation from both theoretical and observational perspectives. In the first chapter we investigate the accuracy of the slow-roll approximation given current observational constraints. We find that the first order slow-roll approximation works better than expected and that the higher order corrections do not improve the results as compared to the exact numerical solutions.

In the second and third chapters we explore the current constraints on the cosmological parameters using Markov Chain Monte Carlo method. We show, that for the first year WMAP data, one should perform full marginalization over the foregrounds and exact calculation of the likelihood function for low multipoles. Neglecting this produces significant inaccuracy in determination of basic cosmological parameters and prefers unnatural running of the primordial power spectrum from inflation. We also study the level of Sunyaev-Zel'dovich effect in WMAP data and how it affects the cosmological parameters. In the third chapter we perform joint analysis of Ly-alpha forest data with other available cosmological datasets.

In the last chapter of this thesis we report our progress towards measuring the probability distribution function of Ly-alpha forest flux from SDSS quasars. Combined together with Ly-alpha forest flux power spectrum it can improve cosmological parameters that constrain inflationary models.

Acknowledgements

First, I would like to thank my advisor Uroš Seljak for his invaluable guidance and help over the past years. A large part of this thesis is about ly-alpha forest analysis, which has been done in a very close collaboration with Pat McDonald. I also thank Lyman Page for being my experimental project advisor and agreeing to read this thesis.

I am indebted to the following people with whom I had a lot of very important discussion on cosmology and physics in general: Sergei Bashinsky, Latham Boyle, Steven Gratton, Kevin Huffenberger, Nikhil Padmanabhan.

A lot of computations in this thesis have been done on clusters of physics and astrophysics departments. I would like to thank system administrators Vinod Gupta, Neel Arora and Steve Huston for keeping the clusters up and running and for their fast response to the problems which appeared sometimes.

I couldn't imagine my life here at Princeton without my friends: Sandrine Anthoine, Sasha Baitine, Pavel Batchourine, Andiy Didovyk, Anatoly Dymarsky, Joelle and Dave Escoffery, Karol Gregor, Karen Jeng, Nick Kuzma, Iveta Lukosiute and Gherman Mustuk, Darya Nachinkina, Sasha Ovetsky, Vasily Pestun, Anna Pierrehumbert, Sri Raghu, Dima Sarkisov, Vassos Soteriou, Peter Svrček, Fumin Zhang, Olga Zhilyaeva and many others whom I did not mention here.

Special thanks to Patricia Li simply for sharing best moments with me.

I would especially like to thank my parents and my brother, whose constant support was invaluable.

Contents

Abstract **iii**

Acknowledgements **iv**

Contents **v**

List of Figures **viii**

List of Tables **x**

1 Introduction **1**

2 Accuracy of Slow-Roll Inflation Given Current Observational Constraints **5**

2.1 Introduction 6

2.2 Inflationary basics 7

2.3 Quadratic potential 12

2.4 Potential with a bump in the second derivative 16

2.5 Flow equations simulations 20

2.6 Is truncated Taylor expansion good? 25

2.7 Conclusions 26

3 Markov Chain Monte Carlo in Application to Estimation of Cosmological Parameters **29**

3.1 Introduction 30

3.2 Method 31
3.3 Effects on cosmological parameters of proper likelihood evaluations of low multipole first year WMAP data 33
3.4 Effect on cosmological parameters of Sunyaev-Zel'dovich effect in WMAP . 40

4 Cosmological parameter analysis including Ly-alpha forest 44
4.1 Introduction 44
4.2 Method 49
4.3 Results 52
4.3.1 Amplitude of fluctuations 53
4.3.2 Optical depth 58
4.3.3 Neutrino mass 60
4.3.4 Tensors 63
4.3.5 Spectral index 63
4.3.6 Running of the spectral index 64
4.3.7 Matter density and Hubble parameter 68
4.3.8 Dark energy 70
4.4 Implications for inflation 77
4.4.1 Large field models 79
4.4.2 Large positive curvature models 82
4.4.3 Large negative curvature models 83
4.5 Conclusions 85

5 Progress in Measuring the Probability Distribution Function of Ly-α forest flux from SDSS quasars sample 88
5.1 Introduction 88
5.2 Theoretical PDF of Ly-α forest 89
5.3 Reconstruction technique 90
5.4 Smoothing the spectra 90

5.5 Subtracting the noise through maximizing the likelihood 93
5.5.1 Parameterization of PDF 93
5.6 Corrections to the likelihood function 94
5.7 Results 95

A Inflationary Equations **99**
A.1 Non-perturbed inflationary equations 100
A.2 Perturbation equations 103
A.2.1 Scalar mode 103
A.2.2 Tensor mode 106

References **107**

List of Figures

1.1 Different types of experiments let us probe different scales. 2

2.1 The current constraints in n_s–α_s plane from current data 11
2.2 Behavior of slow-roll parameters for potential $V = m^2\phi^2/2$ 14
2.3 Power spectrum produced by $V = m^2\phi^2/2$ 15
2.4 Behavior of slow-roll parameters for potential (2.26) 18
2.5 Power spectrum produced by potential (2.26) 19
2.6 Behavior of slow-roll parameters for flow-equations reconstructed potential . 23
2.7 Power spectrum produced by potential reconstructed from flow-equations simulations 24
2.8 Comparison of AKS approximation to Taylor series approximation 27

3.1 Effects of proper likelihood calculation on Ω_m constraints 34
3.2 Change in constraints on running α_s 35
3.3 Two dimensional contours in (α_s, τ) and $(\alpha_s, z_{\rm ri})$ planes 36
3.4 Likelihood cotours in τ and α_s plane 37
3.5 Two-dimensional contours in (ω_b, B) plane 42

4.1 Contours in the planes of τ versus Ω_m, h, σ_8 and n_s 59
4.2 Constraints in the $(r = T/S, n_s)$ plane with and without SDSS-lya 64
4.3 Contours in the (α_s, n_s) plane 66
4.4 Contours in the (α_s, r) plane 67
4.5 Contours in the (Ω_m, σ_8) plane 69

4.6 Contours in the (Ω_m, h) plane 70
4.7 Contours in the (Ω_m, w) plane 72
4.8 Contours in the (w, r) plane 73
4.9 Contours in the (w_0, w_1) plane 74
4.10 Constraints on $w(z)$ versus redshift z 75
4.11 Same as Figure 4.10 but for MCMC with tensors. 76
4.12 Contours in the (ϵ_V, η_V) plane 80
4.13 Contours in the (η_V, ξ_V) plane 81
4.14 Scatter plot of MCMC solutions with $n_s < 1$ converted into the (p, N) plane assuming relations valid for chaotic inflation models 82

5.1 An example of correlations between different pdf bins within one redshift bin 97
5.2 Reconstruction results for the first redshift bin 98

List of Tables

3.1 Cosmological parameters we use to run the MCMCs. 32

3.2 Constraints on cosmological parameters from WMAP data alone 38

3.3 Constraints on cosmological parameters from WMAP+SDSS analysis . . . 39

3.4 Constraints on cosmological parameters with and without Sunyaev-Zeldovich component 43

4.1 Constraints on basic 6 parameters and tensors 54

4.2 Constraints on running 55

4.3 Neutrino mass constraints 56

4.4 Dark energy constraints 57

Chapter 1

Introduction

Inflation is currently the leading paradigm explaining the initial conditions for our Universe. Right after the Big Bang the Universe started exponentially expanding, which caused the Universe to become approximately flat, homogeneous and isotropic. During this rapid expansion stage the initial quantum fluctuations transformed into classical fluctuations when they crossed the horizon. The prediction for the produced fluctuations is that their spectrum is nearly scale-invariant with very little deviations. The deviations from the scale-invariant Harrison-Zel'dovich spectrum depend on the so called inflationary potential, which governed the accelerated expansion of the universe. Primordial fluctuations after reheating transformed into photon and matter fluctuations, which later caused the Cosmic Microwave Background anisotropy and the structure formation.

By measuring the fluctuations (e.g. from CMB, galaxy clustering, Ly-alpha forest etc.) at the later times of the history of the Universe, going backwards in time we can get all the way back to the initial inflationary potential. In this thesis we show some of the steps which are directed towards learning more about the inflationary potential.

After WMAP [2] released their first-year data in 2003 an era of precision cosmology came. Indeed, the accuracy of the measurements of most of the cosmological parameters has enormousle increased. We learnt about the contents of our universe: that regular baryonic matter composes only about 4% of the total mass of the Universe, some 22% is

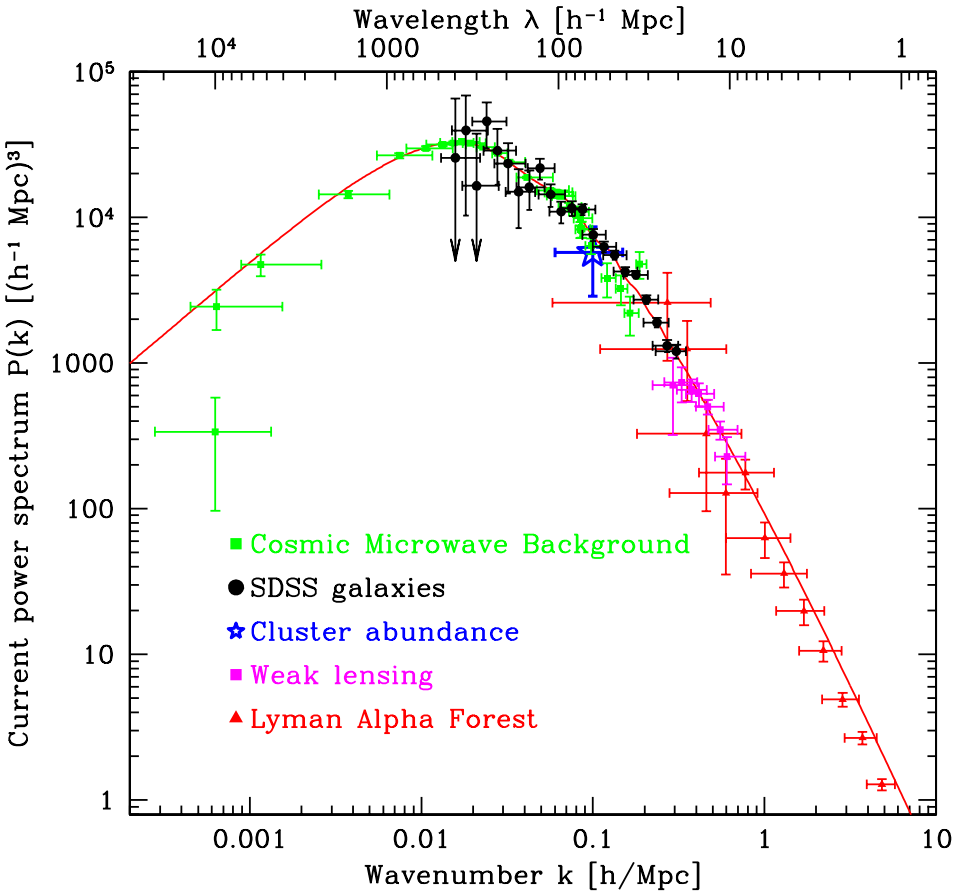

Figure 1.1: Different types of experiments let us probe different scales. The figure is taken from Ref. [1].

taken by invisible dark matter and the rest of 74% is covered by mysterious "dark energy", that acts as a sort of an anti-gravity.

Original first-year WMAP analysis included joint analysis of early Ly-α forest power spectrum analysis, which detected 3σ deviation of the running of the primordial power spectrum from the inflationary prediction of zero running. Seljak, McDonald and Makarov [3] showed that more rigorous analysis of the same Ly-α forest data reduced the significance of the running discovered earlier.

A year later Slosar, Seljak and Makarov [4] demonstrated that a more accurate analysis of low-multipole WMAP data further diminishes the running. They received this result after proper foreground marginalization and more accurate likelihood function calculation than in the original WMAP analysis.

Figure 1.1 shows how different experiments probe different scales. Thus, Cosmic Microwave Backgrounds measures the fluctuations at large scale of 10^2–$10^4 h^{-1}$Mpc, galaxy clustering works at the scale of $10^2 h^{-1}$Mpc and Ly-alpha forest probes small scale fluctuations at the scale of $10 h^{-1}$Mpc.

The initial WMAP analysis underestimated the fluctuations at both the smallest (low-multipole CMB) and the largest scales (from early Ly-alpha forest), therefore getting significant negative running of the slope of the primordial power spectrum of fluctuations. This means that we have to be precise in our calculations, otherwise it can lead us to improper conclusions. In this thesis, we present some of the necessary steps for more precise measurement of the primordial fluctuations and other cosmological parameters.

In the second chapter, we look at the inflationary models that produce large negative running. We look at how accurately slow-roll approximation can describe the primordial spectrum of fluctuations for such models and whether we need more precise exact numerical solutions of the inflationary equations.

In the third chapter of this thesis we look at how full foreground marginalization and exact likelihood calculation of low-multipole data from WMAP affects the estimation of the cosmological parameters. We also investigate how the level of Sunyaev-Zel'dovich effect in

WMAP maps modifies our estimates.

In the fourth chapter, we present results of joint analysis of Ly-alpha forest power spectrum together with CMB and galaxy clustering data. We find improved constraints on the mass of neutrinos, the equation of state of the dark energy and the slope and the running of primordial power spectrum.

In the last chapter, we report our progress towards measuring the probability distribution function of Ly-alpha forest flux from SDSS data sample. The pdf knowledge should help improve measurement of the mean flux of Ly-alpha forest, and, therefore, to give better estimates of the flux power spectrum. This technique should produce more precise determination of the amplitude of the primordial fluctuations on small scales. Combining with future CMB experiments we will be able to determine the exact form of the inflationary potential corresponding to the wide range of scales.

Chapter 2

Accuracy of Slow-Roll Inflation Given Current Observational Constraints

This chapter has been published as: A. Makarov, "On the accuracy of slow-roll inflation given current observational constraints," Phys. Rev. D **72**, 083517 (2005) [5]

Original abstract: We investigate the accuracy of slow-roll inflation in light of current observational constraints, which do not allow for a large deviation from scale invariance. We investigate the applicability of the first and second order slow-roll approximations for inflationary models, including those with large running of the scalar spectral index. We compare the full numerical solutions with those given by the first and second order slow-roll formulae. We find that even first order slow-roll is generally accurate; the largest deviations arise in models with large running where the error in the power spectrum can be at the level of 1-2%. Most of this error comes from inaccuracy in the calculation of the slope and not of the running or higher order terms. Second order slow-roll does not improve the accuracy over first order. We also argue that in the basis $\epsilon_0 = 1/H$, $\epsilon_{n+1} = d\ln|\epsilon_n|/dN$, introduced by Schwarz et al. (2001), slow-roll does not require all of the parameters to be small. For example, even a divergent ϵ_3 leads to finite solutions which are accurately described by a

slow-roll approximation. Finally, we argue that power spectrum parametrization recently introduced by Abazaijan, Kadota and Stewart does not work for models where spectral index changes from red to blue, while the usual Taylor expansion remains a good approximation.

2.1 Introduction

Inflation is a theory which postulates that a rapid expansion of the universe occurred right after the Big Bang [6, 7, 8, 9]. Most inflationary models can be represented by an effective single field model with effective potential V. The inflaton with mass m rolls down the potential until the kinetic energy of the inflaton is greater than half of its potential energy. At this point the inflationary expansion of the universe stops and the next phase of reheating occurs. During the inflationary expansion, the initial quantum fluctuations exponentially increase and become classical [10, 11, 12, 13, 14, 15]. These classical fluctuations also seed the subsequent growth of large scale structure. There is a well defined procedure which allows us to find the spectrum of the fluctuations given the inflationary potential. Because exact solutions are numerically intensive several appoximations have been developed. The most common approximation is the slow-roll approximation. Recently the so-called uniform approximation was suggested [16, 17]. Reference [18] developed improved WKB-type approximation.

If the kinetic energy of the inflaton is much smaller than its potential energy, we say that the inflaton is slowly rolling down its potential. In this slow-roll approximation we can obtain analytical formulae for the produced power spectrum in the form of a Taylor series expansion in a set of slow-roll parameters. The coefficients in the Taylor expansion of the logarithm of the power spectrum in $\ln k$ effectively define the slope $n_s - 1$, running α_s and higher derivatives. We usually derive the slow-roll formulae through the time delay formalism or Bessel function approximation. Therefore there are some implied conditions on the accuracy of the slow-roll approximation depending upon the slow-roll parameters. References [19, 20] found that there are areas in the slow-roll parameter space where the accuracy of slow-roll approximation is questionable. This usually requires a large deviation

of n_s from 1. However it contradicts the latest observations [2, 21, 22].

Recently there has been a lot of renewed interest in models with large running of the scalar index [23, 24, 25]. It is not clear whether slow-roll approximation is accurate in this area of parameter space, as in some expansions one of the slow roll parameters becomes large and the expansion is no longer well controlled [20]. Another issue is the question of where to stop the expansion. Although it is often assumed that the running is $O\left((n_s-1)^2\right)$, reference [26] found that there are cases where it can be as large as $n_s - 1$. In this case one should also consider the effect of including the running of the running of n_s, i.e. the second derivative of n_s over $\ln k$. These are the issues addressed in this paper. We begin with a short review of the basic physics of inflation and the algorithm of numerical solutions to the inflationary equations, with more details given in appendix. We continue by comparing the numerical solutions to those given by slow-roll approximations and finally we present our conclusions.

In this paper we use a standard convention for reduced Planck mass $m_{\rm pl} = G_N^{-1/2}$.

2.2 Inflationary basics

In the "Hamilton-Jacobi" formulation, the evolution of the Hubble parameter $H(\phi)$ during inflation with potential $V(\phi)$ is given by (e.g. see [27])

$$\left[H'(\phi)\right]^2 - \frac{12\pi}{m_{\rm pl}^2} H^2(\phi) = -\frac{32\pi^2}{m_{\rm pl}^4} V(\phi). \tag{2.1}$$

The number of e-folds N since some initial time is related to the value of the scalar field ϕ by

$$\frac{dN}{d\phi} = -\frac{4\pi}{m_{\rm pl}^2} \frac{H(\phi)}{H'(\phi)}. \tag{2.2}$$

We will consider the situation when the value of the scalar field is growing in time, $d\phi/dt > 0$. Then by our convention dN/dt is also positive, $dN/dt > 0$.

In the literature, different sets of slow-roll parameters are used. Reference [28] introduce potential slow-roll parameters which are constructed on the basis of the derivatives of the

inflationary potential $V(\phi)$. Authors of [29] define Hubble slow-roll parameters through the derivatives of the Hubble parameter $H(\phi)$ with respect to the field ϕ during inflation

$$\epsilon_H(\phi) = \frac{m_{\rm pl}^2}{4\pi}\left(\frac{H'(\phi)}{H(\phi)}\right)^2, \tag{2.3}$$

$$\eta_H(\phi) = \frac{m_{\rm pl}^2}{4\pi}\frac{H''(\phi)}{H(\phi)}, \tag{2.4}$$

$${}^n\xi_H(\phi) = \left(\frac{m_{\rm pl}^2}{4\pi}\right)^n \frac{(H')^{n-1}H^{(n+1)}}{H^n}\,. \tag{2.5}$$

In this parameterization when the inequality $\epsilon_H(\phi) < 1$ fails, the inflation immediately stops. Sometimes ${}^2\xi_H$ is also denoted ξ_H or ξ_H^2 though it can take negative values. In this paper we will use $\xi_H \equiv {}^2\xi_H$.

Reference [30] introduces another basis of "horizon-flow" slow-roll parameters through the logarithmic derivative of the Hubble distance $\epsilon_0 = d_H = 1/H(N)$ with respect to the number of e-folds N to the end of inflation

$$\epsilon_{n+1} = \frac{d\ln|\epsilon_n|}{dN}. \tag{2.6}$$

The connection between any two of these sets can be found in e.g. [30]. Thus the first three horizon-flow slow-roll parameters are connected to the first three Hubble slow-roll parameters as [29, 31, 20]

$$\epsilon_1 = \epsilon_H, \tag{2.7}$$

$$\epsilon_2 = 2\epsilon_H - 2\eta_H, \tag{2.8}$$

$$\epsilon_2\epsilon_3 = 4\epsilon_H^2 - 6\epsilon_H\eta_H + 2\xi_H. \tag{2.9}$$

There is an analytical connection between Hubble slow-roll parameters and potential slow-roll parameters [29].

References [32, 33, 34, 35] use differently defined sets of slow-roll parameters, but they still can be converted to the ones we have described here (e.g. see [30]).

Thus any inflationary model can be completely described by the evolution of one of the sets of the parameters.

The condition for the inflation to occur is $\epsilon_1 = \epsilon_H < 1$ or $\epsilon_V \lesssim 1$ since $\epsilon_H = \epsilon_V$ to first order.

To find the power spectrum of the perturbations produced by a single field inflation, one can follow the prescription of Grivell and Liddle [36]. One solves the equation [37, 38, 33]

$$\frac{d^2 u_k}{d\tau^2} + \left(k^2 - \frac{1}{z}\frac{d^2 z}{d\tau^2}\right) u_k = 0 \tag{2.10}$$

for each mode with wavenumber k and initial condition $u_k(\tau) \to \frac{1}{\sqrt{2k}} e^{-ik\tau}$ as $\tau \to -\infty$. Then the spectrum of curvature perturbations is given by

$$\mathcal{P}_{\mathcal{R}}(k) = \frac{k^3}{2\pi^2}\left|\frac{u_k}{z}\right|^2. \tag{2.11}$$

The quantity z in equation (2.10) is defined as $z = a\dot{\phi}/H$ for scalar modes and $z = a$ for tensor modes. Then for scalar modes [36]

$$\frac{1}{z}\frac{d^2 z}{d\tau^2} = 2a^2 H^2 \left[1 + \epsilon_H - \frac{3}{2}\eta_H + \epsilon_H^2 - 2\epsilon_H \eta_H + \frac{1}{2}\eta_H^2 + \frac{1}{2}\xi_H\right]. \tag{2.12}$$

One can parametrize the power spectrum of the scalar and tensor modes of the fluctuations amplified by the inflation as

$$\ln \frac{\mathcal{P}(k)}{\mathcal{P}_0} = (n-1)\ln\frac{k}{k_*} + \frac{\alpha}{2}\ln^2\frac{k}{k_*} + \frac{\beta}{6}\ln^3\frac{k}{k_*} + \ldots \tag{2.13}$$

around some conventional pivot point k_*. Leach et al. [20] give expressions for the scalar spectral index n_s, the running of the scalar spectral index α_s, the tensor spectral index n_t and the running of the tensor spectral index α_t in terms of the horizon-flow parameters. Here we reproduce their second order formulae for $n_s - 1$ and α_s

$$\begin{aligned} n_s - 1 &= -2\epsilon_1 - \epsilon_2 - 2\epsilon_1^2 \\ &\quad -(2C+3)\epsilon_1\epsilon_2 - C\epsilon_2\epsilon_3, \end{aligned} \tag{2.14}$$

$$\alpha_s = -2\epsilon_1\epsilon_2 - \epsilon_2\epsilon_3, \tag{2.15}$$

where $C = \gamma_{\mathrm{E}} + \ln 2 - 2 \approx -0.7296$.

Reference [20] also analyzes the accuracy of the approximation (2.13) for parameterizing the inflationary power spectrum of fluctuations with $\beta = 0$ for different values of the parameters r, n_s and α_s.

In this paper we will also compare the second order formulae (2.14, 2.15) to the first order formulae given by

$$n_s - 1 = -2\epsilon_1 - \epsilon_2, \tag{2.16}$$

$$\alpha_s = -2\epsilon_1\epsilon_2 - \epsilon_2\epsilon_3. \tag{2.17}$$

The expression for α_s is the same as in the second order formula because the expression for α_s is derived using only first order expression for n_s. Thus the main difference between first and second order formulae comes from the extra terms in the expression for $n_s - 1$.

Current observational constraints on r, n_s and α_s are given by [39, 22, 4]. At 95% confidence level, the tensor to scalar ratio is $R < 0.50$, which implies that the first horizon-flow parameter ϵ_1 is much smaller than one. Current constraints on the scalar spectral index give us $n_s = 0.98 \pm 0.02$, which in turn means that the second horizon-flow slow-roll parameter is much smaller than one.

Present data does not require the presence of running in the primordial power spectrum [40], but running as large as ± 0.03 is still allowed at 3-σ [22]. Regular inflationary models usually predict $|\alpha_s| \sim (n_s - 1)^2$ and so the running is of the order of 10^{-3}, as is the case for the minimally-coupled $V(\phi) = \lambda\phi^4$ model with 60 e-folds remaining.

But it is possible that $|\alpha_s| \gg (n_s - 1)^2$ and $\alpha_s < 0$, which means that the main part in the running of the spectral index (2.15) is determined not by the first term $-2\epsilon_1\epsilon_2$, but by the second term $-\epsilon_2\epsilon_3$. It happens when $|\epsilon_3| \gg |\epsilon_1|$, and therefore there might be a situation when $|\epsilon_3| > 1$.

To summarize, if $n_s \approx 1$ and α_s is a small negative number, at some scale we might have $\epsilon_1 \ll 1$, $\epsilon_2 \ll 1$ and $|\epsilon_3| > 1$. Leach et al. [20] define inflation satisfying slow-roll under the condition $|\epsilon_n| \ll 1$, for all $n > 0$. In our case $\epsilon_3 > 1$, so the question arises as to whether slow-roll in this case is accurate or whether the approximation breaks down and one must also include terms with higher powers in ϵ_3. Does it mean that the inflation is not slow-roll and one must use full numerical solutions instead? And does it mean that one must also include the running of the running? These are the main questions we address in this paper. To address them we have developed the numerical code described in appendix A.

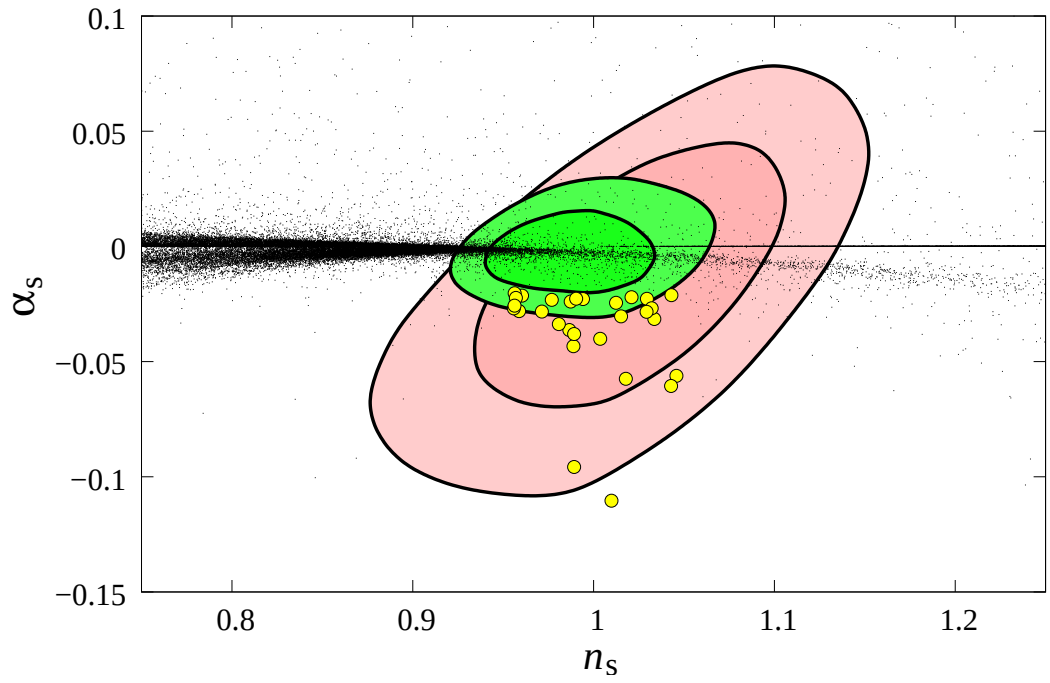

Figure 2.1: The current constraints (68% and 95% confidence level contours) in the n_s–α_s plane from WMAP+SDSSgal (bigger, red) and WMAP+SDSSlya (smaller, green) data [22, 4, 39, 21]. The constrained region clearly allows the value of the spectral scalar index n_s to be around 1 and the running α_s of the scalar spectral index to be significantly non-zero for either combination of the experiments.

How natural is it for inflation with a given number from 50 to 70 e-folds remaining to produce a power spectrum with a changing tilt? In the absence of theoretical guidance on the inflationary space we cannot address this question simply. Authors of [23] have produced about 200,000 simulations of the inflationary flow equations for more or less "random" potentials, and calculated the observable parameters (n_s, α_s, r, n_t, α_t) of the resulting power spectra about 40 to 70 e-folds before the end of the inflation for each potential. About 80,000 of them fall into the area plotted on Fig. 2.1 and are marked as black dots. Only the fifteen marked with larger yellow circles give a significant change in the tilt from red to blue, i.e. $n_s \sim 1$, $\alpha_s < -0.02$.

Choosing the Hubble parameter to be represented by a Taylor expansion in ϕ with uniformly distributed coefficients, as done in [23], does not necessarily correspond to the real inflationary priors [41]. We do not address this issue here; instead we want to simply stress that possibility of constructing a potential with a large running in the scalar power spectrum 40-70 e-folds before the end of the inflation exists.

2.3 Quadratic potential

As a test of our code, in this section we investigate how well the slow-roll formulae work in the slow-roll regime for one of the usual potentials that do not predict large running. As an example we will consider a simple quadratic potential, $V = m^2\phi^2/2$, which is a classic example of chaotic inflation. The second panel from the bottom in Fig. 2.2 effectively shows the dependence of z''/z on the number of the e-folds for inflation with such a potential. The behavior is monotonic and very smooth, which is due to the smoothness of the derivatives of the potential. Since z''/z scales as $2a^2H^2$, we plot the quantity

$$\frac{1}{2a^2H^2}\frac{z''}{z} - 1 \tag{2.18}$$

instead (compare to equation (2.12)).

The top two panels show the dependence of ϵ_H, η_H and ξ_H on the number of e-folds. The only significantly non-zero term is ϵ_H, which gradually grows to 1 at the end of inflation.

The values of η_H and ξ_H are typically smaller by roughly 10^3 and 10^4 respectively.

Figure 2.3 shows the primordial power spectrum produced by the quadratic potential. The second panel from the bottom describes the error produced by the slow-roll approximations. The first order approximation gives less than 0.2% error in the observed range of wavenumbers k. The second order approximation works slightly better; the error is just above 0.1%. Both of these numbers are likely to be good enough for the upcoming experiments. This is because the accuracy at large scales is limited by the finite number of modes, while at small scales it is limited by the nonlinear evolution. So, while the overall amplitude could in principle be determined to an accuracy of 0.1% when CMB and lensing information is combined, it is unlikely that such a precision will be achieved separately at two widely separated length scales.

Taking a more careful look at the error plot, one sees that the error curve in the observed area is basically a straight line, meaning that the main source of error is not the imprecise value of α_s but the error in n_s. Let us estimate now how precisely we need to know n_s to get an error of, say 0.2%, in the observed range. The imprecision δn_s in n_s will give us the uncertainty

$$\delta n_s \frac{1}{2} \ln \frac{k_{\max}}{k_{\min}} = 0.002. \tag{2.19}$$

Taking the observed range of k's to be from 10^{-3} Mpc^{-1} to 1 Mpc^{-1}, we find that one needs to find n_s with the precision of $\delta n_s = 6 \cdot 10^{-4}$.

The same allowed uncertainty $\delta\alpha_s$ in α_s is estimated from

$$\frac{1}{2}\delta\alpha_s \left(\frac{1}{2} \ln \frac{k_{\max}}{k_{\min}}\right)^2 = 0.002. \tag{2.20}$$

Therefore $\delta\alpha_s = 3 \cdot 10^{-4}$ is the error which we can make in determining α_s in order to get an error in the power spectrum of 0.2% at the edges of the observed range of k's.

The two top panels of Fig. 2.3 compare the numerically found dependence of n_s and α_s on k to the one found from the slow-roll approximation with the first order α_s and either the first or second order for n_s. One should compare the discrepancies between these to the values of δn_s and $\delta\alpha_s$. The characteristic value of n_s is .964 and the discrepancy between

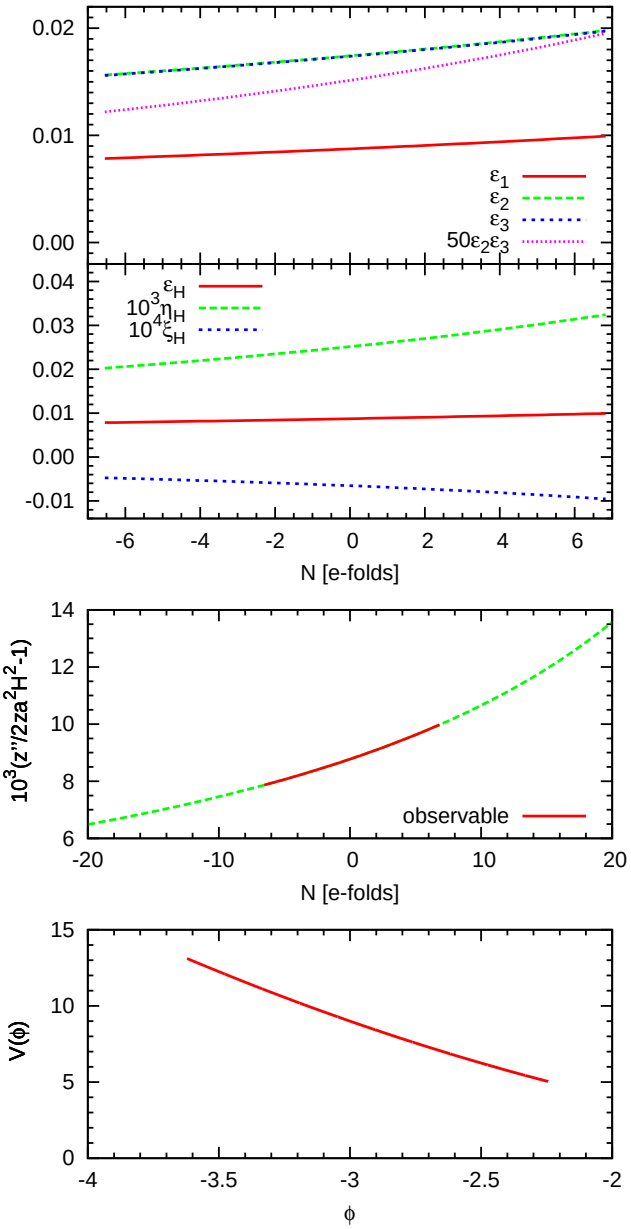

Figure 2.2: Panels from the bottom to the top: 1. Potential $V = m^2\phi^2/2$ in the range of ϕ's where the inflation occurs around 50 e-folds before the end of inflation. The scale in V is not COBE-normalized on this plot. 2. The dependence of z''/z on the number of the e-folds during the inflation. Number of e-folds $N = 0$ corresponds to our arbitrarily chosen pivot scale of $k = 0.05$/Mpc. 3. Plots of Hubble slow-roll parameters ϵ_H, η_H, ξ_H. The value of ϵ_H is non-negligible whereas η_H and ξ_H are essentially zeros. 4. Plots of horizon-flow slow-roll parameters ϵ_1, ϵ_2, ϵ_3 and the product of $\epsilon_2\epsilon_3$ for the same inflationary model. Since in this case $\epsilon_H \gg \eta_H, \xi_H$, the value of ϵ_1 is essentially $\epsilon_1 \approx \epsilon_H$ and $\epsilon_2 \approx \epsilon_3 \approx 2\epsilon_H$. Nothing unexpected is going on here for this model.

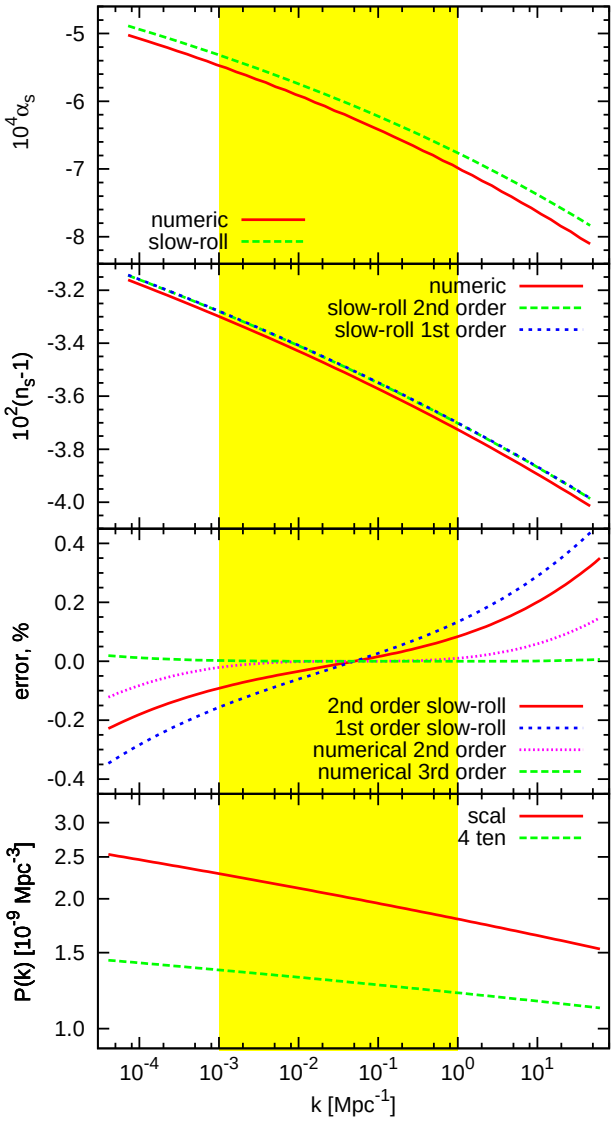

Figure 2.3: Panels from the bottom to the top: 1. Power spectrum produced by inflation with potential $V = m^2\phi^2/2$. 2. Errors made by approximating the true scalar power spectrum by (2.13) with calculating n_s and α_s from first order slow-roll formulae (2.16, 2.17), second order slow-roll formulae (2.14, 2.15) and calculating them through numerical derivatives. Numerical third order takes into account third logarithmic derivative of the power spectrum β_s in parameterization (2.13). 3. The evolution of $n_s - 1$ is calculated numerically and by the first and second order slow-roll formulae. 4. The evolution of α_s is calculated numerically and by the slow-roll formulae (first and second order slow-roll are the same for α_s). The error plot clearly shows that the main error comes from the imprecision of $n_s - 1$, whereas the approximation for the α_s works well enough. One can also see that in the case of this potential both first and second order slow-roll formulae for $n_s - 1$ overestimate the real value of $n_s - 1$.

the exact value and the one found from the slow-roll approximation is comparable to δn_s. Running α_s takes values around $-6.5 \cdot 10^{-4}$. The discrepancy between the exact and the slow-roll values is very small in comparison to $\delta\alpha_s$. One can also notice that in this case $|\alpha_s| \approx 2\delta\alpha_s$. Thus, even if we assigned $\alpha_s = 0$, we would not get a significant error in the approximation of the primordial power spectrum of the scalar perturbations.

To summarize this section, for standard inflationary potentials, the slow-roll approximation suffices even at first order when compared to the expected accuracy of existing and future experiments. The second order approximation, while improving the accuracy, is not really necessary. The main error of slow-roll when considered in contrast to the numerical solutions is the inaccuracy in the slope n_s; inaccuracies in higher order expansion terms, such as the running, are less important and can even be ignored.

2.4 Potential with a bump in the second derivative

We want to construct a potential which will give us a strong running and crossing of the point $n_s = 1$ in the observable power spectrum. We want to have $n_s > 1$ at earlier times in inflation, while at later times we want to have $n_s < 1$. To get the desired result, one can take two different potentials producing such features and smoothly connect them.

One can rewrite slow-roll formulae (2.14,2.15) through the potential slow-roll parameters as

$$n_s - 1 = -6\epsilon_V + 2\eta_V, \tag{2.21}$$

$$\alpha_s = 16\epsilon_V\eta_V - 24\epsilon_V^2 - 2\xi_V. \tag{2.22}$$

Now let us just choose our potential to be

$$V(\phi) = 1 - 0.01\phi - 1.20\phi^2 \tag{2.23}$$

for all $\phi > 0$. This choice provides about 50 e-folds of inflation after $\phi = 0$. Since the local properties of the power spectrum are mostly determined by the local "history" of the slow-roll parameters at the moment of the horizon crossing, we can get a red tilt of the

scalar power spectrum $n_s \approx 0.80$ in the area where the "history" before point $\phi = 0$ is not very important. To get an approximately symmetric shape of the power spectrum we choose $V(\phi)$ to be

$$V(\phi) = 1 - 0.01\phi + 1.20\phi^2 \tag{2.24}$$

for all $\phi < 0$. In this case for wave modes which cross the horizon far before the moment when the scalar field takes the value of $\phi = 0$, the spectral index of the primordial power spectrum has a blue tilt $n_s \approx 1.20$. Thus between these two regions the spectral index changes from 1.20 to 0.80. We can unite formulae (2.23) and (2.24) into

$$V(\phi) = 1 - 0.01\phi - 1.20\phi^2 \operatorname{sign}\phi. \tag{2.25}$$

This potential has continuous first and second derivatives, but has a bump in its third derivative. This makes $\dfrac{1}{z}\dfrac{d^2z}{d\tau^2}$ in (2.12) discontinuous around $\phi = 0$. According to [42] this produces oscillations in the power spectrum, which we can indeed see for the potential (2.25). To avoid the oscillations we smooth out the $\operatorname{sign}\phi$ function, changing it to $\dfrac{2}{\pi}\arctan(200\phi)$. In this case (2.25) changes to

$$V(\phi) = 1 - 0.01\phi - 1.20\phi^2 \frac{2}{\pi}\arctan(200\phi), \tag{2.26}$$

which is shown on Fig. 2.4. We have chosen 200 as the coefficient in front of ϕ in the arctan function so that the produced power spectrum has a nice shape as in Fig. 2.5.

The two top panels of Fig. 2.4 show the behavior of the slow-roll parameters ϵ_H, η_H, ξ_H and ϵ_1, ϵ_2, ϵ_3, $\epsilon_2\epsilon_3$ correspondingly. While nothing unexpected happens to the behavior of the conventional Hubble slow-roll parameters ϵ_H, η_H and ξ_H, there appears to be a singularity for the horizon-flow parameter ϵ_3. However, notice that the product $\epsilon_2\epsilon_3$ behaves smoothly and remains small due to the fact that the parameter ϵ_2 is changing its sign and therefore crossing through zero. Thus the parameterization of equation (2.6) introduces a singularity which is not physically present in the model.

Figure 2.5 shows the power spectrum produced by the model of inflation with the potential (2.25). The second panel from the bottom shows the errors made by different approximations. We again observe a similar picture for the slow-roll formulae. The main source

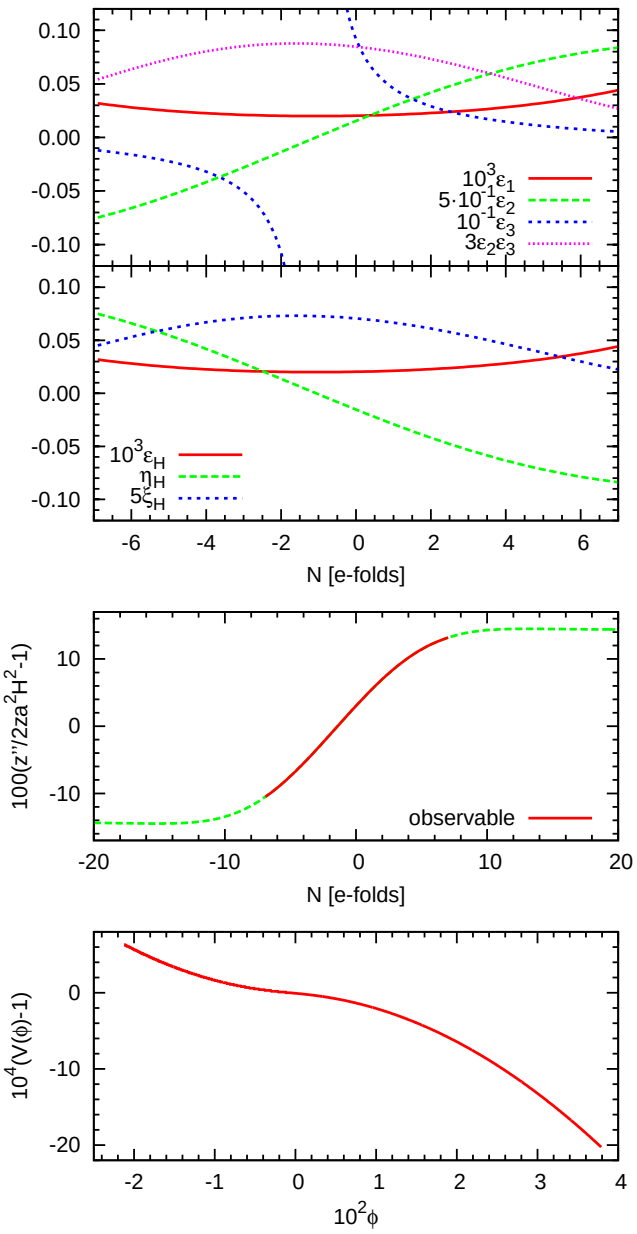

Figure 2.4: Panels from the bottom to the top: 1. Potential (2.26). 2. Effectively this plot shows the dependence of z''/z on the number of the e-folds during the inflation. 3. Plots of Hubble slow-roll parameters ϵ_H, η_H, ξ_H. Though the potential has a singular behavior, all the flow parameters are smooth. 4. Plots of horizon-flow slow-roll parameters ϵ_1, ϵ_2, ϵ_3 and the product of $\epsilon_2\epsilon_3$ for the same inflationary model. While everything is fine with ϵ_1, ϵ_2 and $\epsilon_2\epsilon_3$, the value of ϵ_3 indeed flips over infinity.

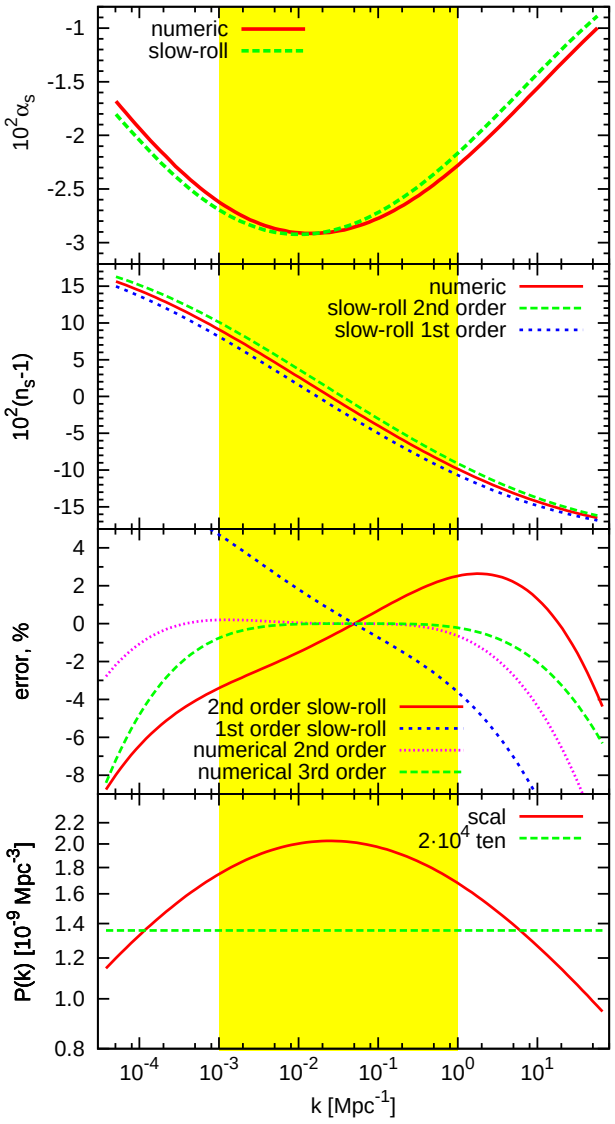

Figure 2.5: Panels from the bottom to the top: 1. Power spectrum produced by (2.26). 2. Errors made by approximating the true scalar power spectrum by (2.13) with calculating n_s and α_s from first order slow-roll formulae (2.16, 2.17), second order slow-roll formulae (2.14, 2.15) and calculating them through numerical differentiation. Numerical third order takes into account third logarithmic derivative of the power spectrum β_s in parameterization (2.13). 3. The evolution of $n_s - 1$ is calculated numerically and by the first and second order slow-roll formulae. 4. The evolution of α_s is calculated numerically and by the slow-roll formulae (first and second order slow-roll are the same for α_s). The error plot clearly shows that the main error comes from the imprecision of $n_s - 1$, whereas the approximation for the α_s works well enough. We see that in the case of this potential, first order slow-roll formula for $n_s - 1$ underestimates the real value, while the second order formula overestimates it.

of error for either the first or second order approximations comes not from the value of α_s but from the error in the value of n_s. From the second panel from the top, we can estimate that the discrepancy is of the order of 0.01 for

$$\delta n_s = n_s^{\rm exact} - n_s^{\rm approx} \tag{2.27}$$

which gives an error of

$$\delta n_s \frac{1}{2} \ln \frac{k_{\rm max}}{k_{\rm min}} \approx 4\% \tag{2.28}$$

in the produced power spectrum at the edges of the observed range. Both the first and second order slow-roll approximations for n_s work somewhat unsatisfactory. The first order slow roll underestimates n_s and the second order overestimates it by about the same amount.

On the other hand, if our goal is to focus on running alone regardless of the slope and use just that property to deduce something about the potential, then the slow-roll does very well, since the differences between the slow-roll and numerical value of running are very small even at the lowest order in slow-roll. Extra terms in the expansion (2.13) further improve the accuracy. Adding running of the running improves the accuracy over the observed range from 1% to 0.2%.

In summary, for potentials that lead to large running, slow-roll does not estimate the slope n_s very accurately at either first or second order, while the accuracy of the running α_s suffices for the existing and future experiments. If we observe over a wide range of scales then it is useful to add the cubic term. Second order slow-roll does not seem to improve the accuracy.

2.5 Flow equations simulations

Kinney [43] introduced a formalism based on the so-called flow equations, further discussed in [41]. The basic idea is that if one fixes the Hubble slow-roll parameters (2.5) at some point in time for ϵ_H, η_H and ${}^{\ell}\xi_H$ up to $\ell = M$ and assumes that all the other Hubble slow-roll parameters are small enough that one can neglect them in one's calculations (i.e. ${}^{\ell}\xi_H = 0$ for all $\ell \geq M+1$) then, without any other assumptions about inflation being

slow-roll, one can find the Hubble slow-roll parameters at any other moment of time using the following hierarchy of linear ordinary differential equations:

$$\frac{d\epsilon}{dN} = -2\epsilon(\eta - \epsilon), \tag{2.29}$$

$$\frac{d\eta}{dN} = \epsilon\eta - {}^{2}\xi, \tag{2.30}$$

$$\frac{d\,{}^{\ell}\xi}{dN} = [\ell\epsilon - (\ell-1)\eta]\,{}^{\ell}\xi - {}^{\ell+1}\xi \tag{2.31}$$

for all $\ell = 2 \ldots M$ assuming ${}^{M+1}\xi = 0$.

Usually when we set up an inflationary problem, we choose a potential $V(\phi)$ and then reconstruct the form of the Hubble parameter during inflation using the main nonperturbed Hamilton-Jacobi inflationary equation (2.1), which gives us an attractor solution $H(\phi)$ which in the inflationary class of problems almost does not depend on the initial condition.

By following the method prescribed by [43] one avoids solving the main attractor inflationary equation (2.1), as pointed out by [41]. Indeed, the assumption ${}^{\ell}\xi_H = 0$ for all $\ell \geq M+1$ requires that $H^{(\ell)}(\phi) = 0$ for all $\ell \geq M+2$. Consequently, $H(\phi)$ is a polynomial of order $M+1$:

$$H(\phi) = H_0(1 + A_1\phi + A_2\phi^2 + A_3\phi^3 + \cdots + A_{M+1}\phi^{M+1}). \tag{2.32}$$

In this case the function $H(\phi)$ is an attractor solution of equation (2.1) with a potential in the form

$$\begin{aligned} V(\phi) = -\frac{m_{\rm pl}^4}{32\pi^2}\left([H'(\phi)]^2 - \frac{12\pi}{m_{\rm pl}^2}H^2(\phi)\right) \\ = -\frac{m_{\rm pl}^4}{32\pi^2}H_0^2\Bigg[\left(A_1 + \cdots + (M+1)A_{M+1}\phi^M\right)^2 \\ - \frac{12\pi}{m_{\rm pl}^2}\left(1 + A_1\phi + \cdots + A_{M+1}\phi^{M+1}\right)^2\Bigg]. \end{aligned} \tag{2.33}$$

Thus the only differential equation one needs to solve in order to match up the number of e-folds and the value of the scalar field ϕ is

$$\frac{dN}{d\phi} = \frac{2\sqrt{\pi}}{m_{\rm pl}}\frac{1}{\sqrt{\epsilon(\phi)}}. \tag{2.34}$$

Here again $\epsilon(\phi)$ is defined as in the equation (2.5):

$$\epsilon(\phi) = \frac{m_{\rm pl}^2}{4\pi}\left(\frac{H'(\phi)}{H(\phi)}\right)^2 = \frac{m_{\rm pl}^2}{4\pi}\left(\frac{A_1 + 2A_2\phi + \cdots + (M+1)A_{M+1}\phi^M}{1 + A_1\phi + A_2\phi^2 + \cdots + A_{M+1}\phi^{M+1}}\right)^2. \quad (2.35)$$

We do not have to numerically solve the hierarchy of M differential flow equations. Instead we have analytical expressions for $V(\phi)$ and $H(\phi)$.

The late attractor $\epsilon = {}^{\ell}\xi = 0$ and $\eta = \text{const}$, found by [43], corresponds to the situation where the inflation proceeds to the value of the scalar field ϕ, which is a solution of the equation $\epsilon = 0$

$$A_1 + 2A_2\phi + \cdots + (M+1)A_{M+1}\phi^M = 0. \quad (2.36)$$

At this point if $A_2 \neq 0$, then $\eta = \text{const} \neq 0$ due to the definition of η, which does not involve ϵ at all. All the other ${}^{\ell}\xi = 0$ since any of them is a product of the first derivative of the Hubble parameter (which is zero) with some higher order derivatives.

Peiris et al. [23] made $M = 9$-th order flow equation simulations; about $40,000$ are shown as black dots on Fig. 2.1. Fifty points fall into the range $|n_s - 1| < 0.05$ and $\alpha_s < -0.02$; these are shown in yellow. Among these point we have chosen 13 which fall into the narrow interval $|n_s - 1| < 0.02$, and we have reconstructed the corresponding inflationary potentials for the inflationary models which give such significant running, together with n_s extremely close to 1.

The bottom panel in Fig. 2.6 shows a potential from such a model with an unusually high value of the running α_s. We notice that there is a small dip in the potential. Some of the potentials with high α_s from the simulations had unrealistically high values of the tensor to the scalar ratio, but all of them had quite similar shapes. The second from the bottom panel of Fig. 2.6 shows the characteristic behavior of the function z''/z which influences the scalar power spectrum as we have seen earlier. The top two panels show the dependence of the slow-roll parameters on the number of e-folds. As in the other case with large running, we find a singularity for the horizon-flow slow-roll parameter ϵ_3, while the product $\epsilon_2\epsilon_3$ behaves smoothly and ϵ_2 crosses zero.

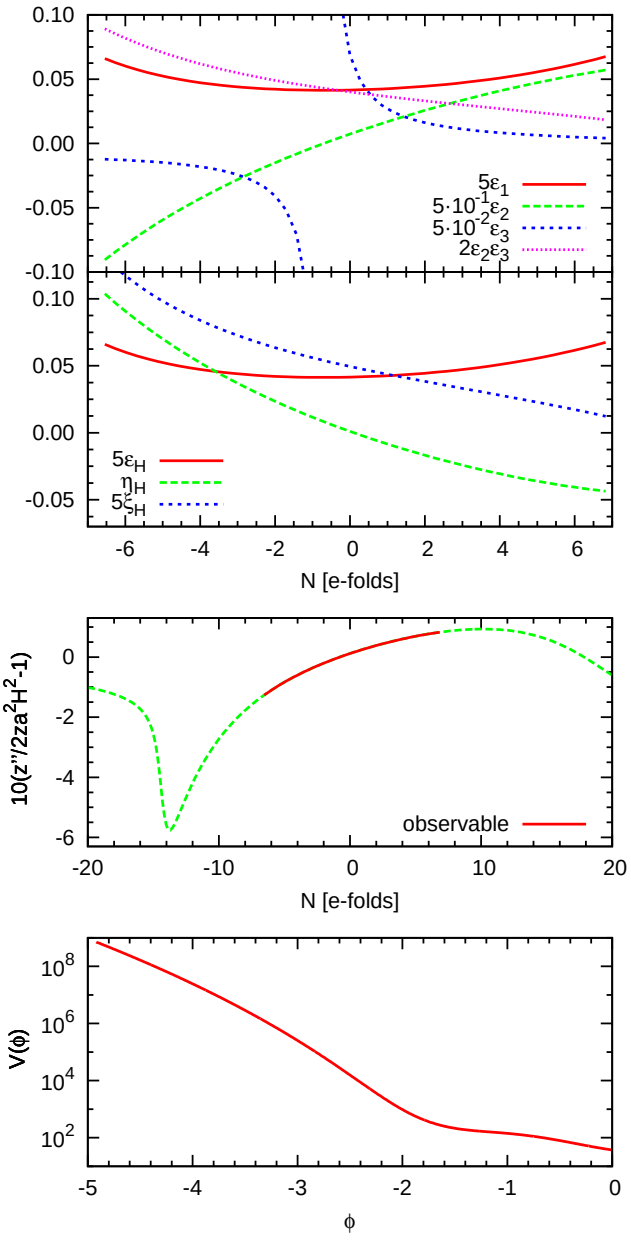

Figure 2.6: Panels from the bottom to the top: 1. Potential reconstructed from one of the flow equations simulations. 2. Effectively this plot shows the dependence of z''/z on the number of the e-folds during the inflation for this potential. 3. Plots of Hubble slow-roll parameters $\epsilon_H, \eta_H, \xi_H$. All of them are smooth. 4. Plots of horizon-flow slow-roll parameters ϵ_1, ϵ_2, ϵ_3 and the product of $\epsilon_2\epsilon_3$ for the same inflationary model. While everything is fine with ϵ_1, ϵ_2 and $\epsilon_2\epsilon_3$, the value of ϵ_3 again flips over infinity.

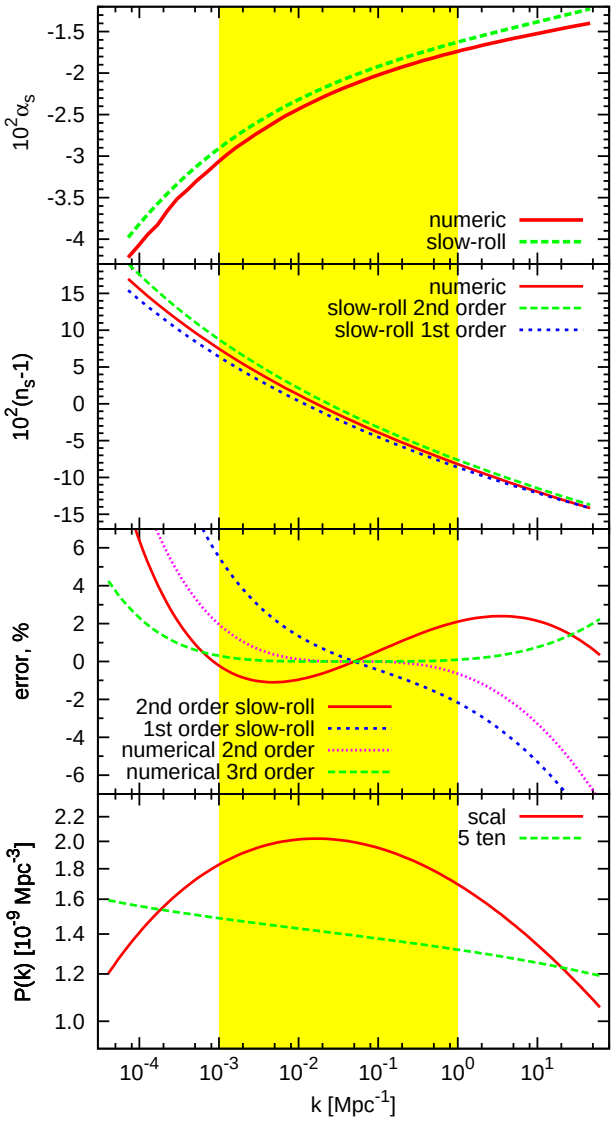

Figure 2.7: Panels from the bottom to the top: 1. Power spectrum produced by potential on Fig. 2.6. 2. Errors made by approximating the true scalar power spectrum by (2.13) with calculating n_s and α_s from first order slow-roll formulae (2.16, 2.17), second order slow-roll formulae (2.14, 2.15) and calculating them through numerical differentiation. Numerical third order takes into account third logarithmic derivative of the power spectrum β_s in parameterization (2.13). 3. The evolution of $n_s - 1$ is calculated numerically and by the first and second order slow-roll formulae. 4. The evolution of α_s is calculated numerically and by the slow-roll formulae (first and second order slow-roll are the same for α_s). The error plot clearly shows that the main error comes from the imprecision of $n_s - 1$, whereas the approximation for the α_s works well enough. One can also see that in the case of this potential first order slow-roll formula for $n_s - 1$ underestimates the real value, while the second order formula overestimates it.

The bottom panel in Fig. 2.7 shows the power spectrum of scalar and tensor perturbations produced by inflation with the potential under consideration. The second from the bottom panel shows the error produced by every one of the approximations for the power spectrum. We again see that both first and second order slow-roll formulae do not give a satisfactory result for n_s. One of them again overestimates n_s; the other underestimates it. The error for either of the approximations is about 2–4%.

The error introduced by the approximate formula for the running α_s is a bit smaller than the one for n_s, but it is somewhat larger compared to the quadratic potential we considered in the previous section.

Chen et al. [44] perform a similar analysis of slow-roll approximation. Using the flow-equations technique, they found discrepancy of larger than 0.01 for n_s between second and third order slow-roll approximations for some of the models. Based on this fact they conclude that third order slow-roll is better. For the model we considered in this section we have found that the third order slow-roll does not improve the results of the second order approximation. In our calculations both formulas give identical results leading to approximately the same order of error as the first order approximation.

2.6 Is truncated Taylor expansion good?

Recently Abazajian, Kadota and Stewart [45] have argued that if

$$|\alpha_s \ln(k/k_*)| \gtrsim |n_s - 1|, \tag{2.37}$$

then the traditional truncated Taylor series parameterization is inconsistent, and hence it can lead to incorrect parameter estimations. One can notice that Taylor expansions $P(x) = \sum a_i x^i$ of functions x^2 or $\cos x$ around $x = 0$ also violates the condition $a_1 \gtrsim a_2 x$, but no one argues that these expansions are not valid. Abazajian et al. propose to use the parameterization

$$\ln \mathcal{P}(k) = \ln \mathcal{P}_0 + \frac{(n_s - 1)^2}{\alpha_s} \left[\left(\frac{k}{k_*} \right)^{\frac{\alpha_s}{n_s - 1}} - 1 \right] \tag{2.38}$$

instead.

There is one significant disadvantage of this approach. In particular, using this parameterization to describe $\mathcal{P}$ as a function of k, one is able to describe only a growing or decreasing function, which can be easily seen from the form of the function. The models we study in this paper produce scalar power spectra which are not purely growing or decreasing (e.g. see Fig. 2.7).

In the previous section we have considered the potential which produces power spectrum satisfying equation (2.37). On Fig. 2.8 we compare the traditional truncated to second and third order Taylor expansion and the parameterization (2.38). We find that the parameterization (2.38) gives a significantly larger error than, e.g. the second order Taylor expansion.

Thus we found that in this particular case though equation (2.37) holds, truncated Taylor expansion is a good approximation and the AKS approach does not improve it. There might be models for which equation (2.38) works better than Taylor expansion, but it is definitely not an improvement for a general case and should be used with caution, if at all.

2.7 Conclusions

In this paper we have explored the accuracy of the slow-roll approximation given the observational constraints on the primordial scalar and tensor power spectra. The current constraints can be roughly described by the tensor to scalar ratio $r < 1$, small deviation from the scale invariance of the scalar power spectrum, $|n_s - 1| < 0.05$ and small but possibly nontrivial running, $|\alpha_s| < 0.03$. These constraints allow for the particular case where $n_s \sim 1$ and $|\alpha_s| > 0.01$, which has previously been argued to not satisfy the slow-roll condition. We have computed exact numerical solutions for the considered potentials and compared them to those obtained from the first and second order slow-roll approximations.

We have found that for the potentials explored here, there is no substantial difference when using first or second order slow-roll formulae for the power spectrum index n_s. Both of them either work well in the case of small running or have a comparable error in the case

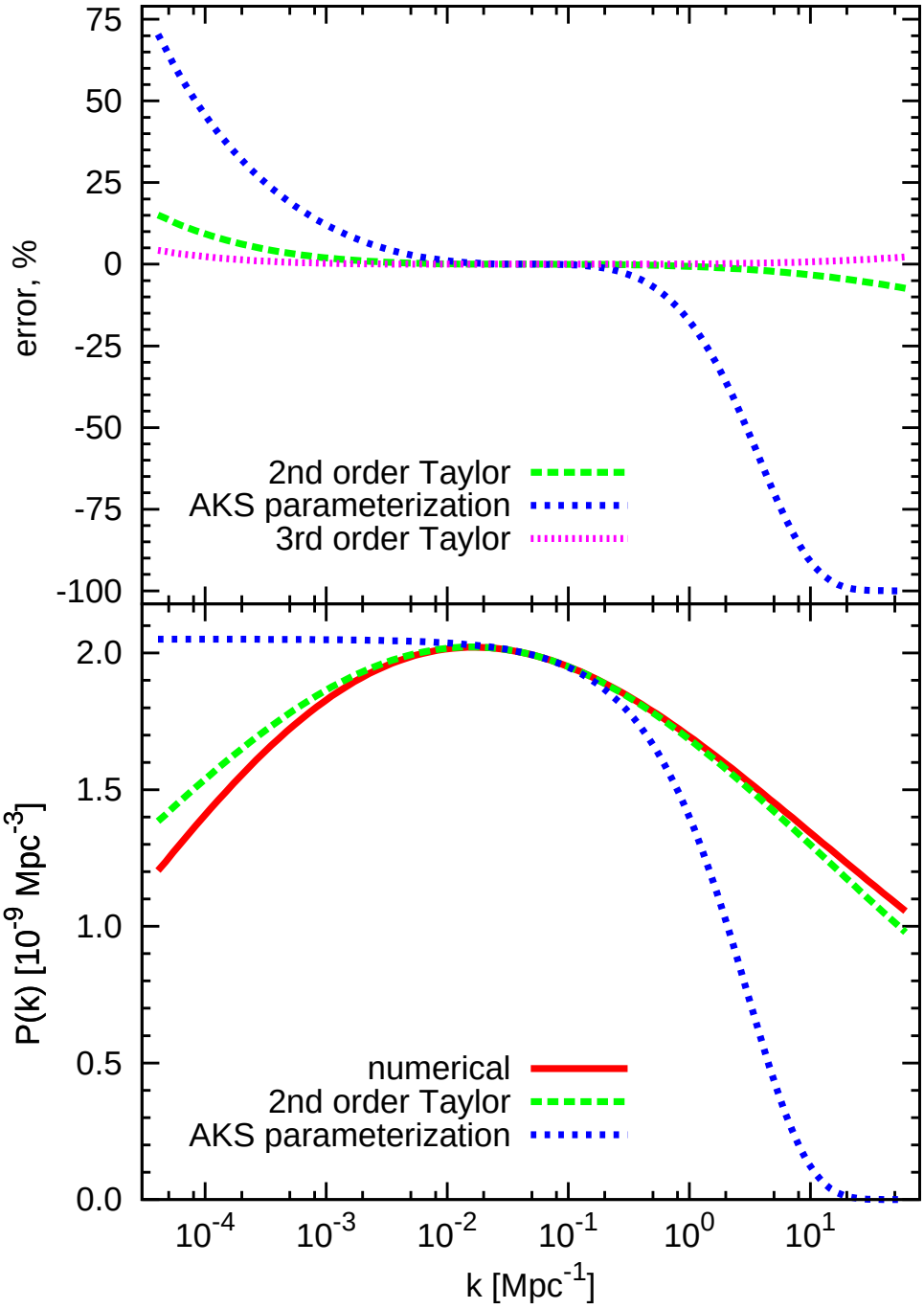

Figure 2.8: The bottom panel shows the numerically calculated power spectrum of the potential we used in section 2.5 and it's approximations by the second order Taylor expansion and by Abazajian, Kadota and Stewart (AKS) parameterization (2.38). The top panel shows the error produced by each of the parameterizations. We have also added the error produced by the third order Taylor expansion here. AKS parameterization acceptably describes the true power spectrum in a very narrow range of k's around the pivot point $k = 0.05$ Mpc^{-1}. It does not improve the truncated Taylor expansion over the wider range of k's.

of non-negligible running. Adding extra (cubic in $\ln k$) terms in the approximation for the scalar power spectrum extends the accuracy to a larger range of scales, but this accuracy is most likely not necessary for existing and near future experiments. If the values of n_s and α_s are known with the precision $\delta n_s = 6 \cdot 10^{-4}$ and $\delta\alpha_s = 3 \cdot 10^{-4}$, then the scalar power spectrum will have an error of about 0.2% at the edge of the observable range of wavenumbers k's.

The horizon-flow basis $\epsilon_{n+1} = d \ln |\epsilon_n| / dN$ introduces an artificial singularity for inflationary models with negative running and the value of the spectral index crossing 1. Such a divergence in one of the horizon-flow parameters does not indicate that the slow-roll approximation has been badly broken. We find that the slow-roll is still accurate at the 1-2% level and most of the error comes from inaccuracies in the evaluation of the slope itself, and not the running. Thus the first order slow-roll approximation is sufficiently accurate for the current observations. Only if the running turns out to be large, while the slope remains close to scale-invariant, are exact numerical calculations required to achieve sub-percent accuracy. In the appendix we present a short guideline on performing such calculations. One can request the code directly from the author.

Chapter 3

Markov Chain Monte Carlo in Application to Estimation of Cosmological Parameters

This and the next chapters are based on the work I have done in the following publications:

- U. Seljak, P. McDonald and A. Makarov, "Cosmological constraints from the CMB and Ly-alpha forest revisited," Mon. Not. Roy. Astron. Soc. **342**, L79 (2003) [3]
- A. Slosar, U. Seljak and A. Makarov, "Exact likelihood evaluations and foreground marginalization in low resolution WMAP data," Phys. Rev. D **69**, 123003 (2004) [4]
- K. M. Huffenberger, U. Seljak and A. Makarov, "Sunyaev-Zeldovich effect in WMAP and its effect on cosmological parameters," Phys. Rev. D **70**, 063002 (2004) [46]
- U. Seljak, A. Makarov *et al.*, "SDSS galaxy bias from halo mass-bias relation and its cosmological Phys. Rev. D **71**, 043511 (2005) [47]
- U. Seljak, A. Makarov *et al.* [SDSS Collaboration], "Cosmological Parameter Analysis Including Sdss Ly-Alpha Forest And Galaxy Bias: Constraints On The Primordial

Spectrum Of Fluctuations, Neutrino Mass, And Dark Energy," Phys. Rev. D **71**, 103515 (2005) [22]

- U. Seljak, A. Makarov, P. McDonald and H. Trac, "Can Sterile Neutrinos Be The Dark Matter?," arXiv:astro-ph/0602430 [48]
- N. Padmanabhan *et al.*, "The Clustering of Luminous Red Galaxies in the Sloan Digital Sky Survey Imaging Data," [49]

3.1 Introduction

Very often in cosmological applications we need to find best fit cosmological parameters to a combination of different datasets. Usually we have to deal with at least 6 parameters, in one of our applications we were working in about 50 dimensions. For apparent reasons, regular grid method for exploring the likelihood surfaces does not work. Indeed, if we had to have 10 points in each of N dimensions, it would take us 10^N likelihood evaluations. Taking into account that the modern datasets require heavy numerical calculations to find the likelihood, the problem becomes almost impossible to solve. Markov Chain Monte Carlo approach drastically decreses the required number of calculations, for most of our applications we did not more than $100,000$ likelihood function evaluations.

Markov Chain Monte Carlo approached is based on rejection Metropolis-Hastings algorithm. By comparing likelihood of the current chain position to the likelihood of a randomly chosen "candidate", we either accept or reject it depending on the likelihood ratio of these two points. Finally we end up with a chain of points which are distributed with proportionally to the likelihood of the datasets of the interest. Markov Chain Monte Carlo method has been widely used in biological applications for estimation of parameters, it was first applied to cosmology in Ref. [50]. Later it became very popular [51, 52] and now it is one of the primary methods used for estimation of the cosmological parameters.

3.2 Method

We use Markov Chain Monte Carlo method in order to analyze the likelihood surfaces in many dimensional paremeter space. We use the custom developed code which was also used in [22, 47, 46, 4, 3]. A typical chain run consists of 15 or 31 independent chains. The effective combined chain length is at least 3,000 and usually of the order of 5,000 – 10,000 noncorrelated chain elements. The acceptance rate varies depending on the dimensionality of the parameter space and the datasets used and usually is about 30-60%. We also check the sufficient convergence and mixing of the chains in terms of Gelman and Rubin $\hat{R}$ statistics [53]; in particular we require for all the chains to have at least $\hat{R} < 1.05$.

The most common parameter space we explore is

$$\mathbf{p} = \{\omega_b,\ \omega_m,\ \Omega_\Lambda,\ \tau,\ n_s,\ A_s, \alpha_s,\ r,\ w,\ \Omega_t,\ \sum m_\nu,\ b\}, \tag{3.1}$$

where $\omega_b = \Omega_b h^2$, where Ω_b is baryon density in units of critical density and h is the Hubble constant in units of 100 km/s/Mpc; $\omega_m = \Omega_m h^2$ where Ω_m is matter density in units of critical density; Ω_Λ is the dark energy today and w is its equation of state; Ω_t is the total density of the universe; τ is the optical depth; $\sum m_\nu$ is the mass of massive neutrino masses (we consider either 3 degenerate neutrino families or 1 massive in addition to 3 massless); A_s, n_s and α_s are used to describe the primordial power spectrum of scalar perturbations around pivot point $k_0 = 0.05$/Mpc

$$\mathcal{P}_0(k) = A_s \exp\left[(n_s - 1)\ln\frac{k}{k_0} + \frac{1}{2}\alpha_s \ln^2\frac{k}{k_0}\right]. \tag{3.2}$$

We calculate the linear power spectrum and Cosmic Microwave Background anisotropy via CMBFAST [54].

For the chains including tensors, we parametrize them through their amplitude $A_t = rA_s$ at the same pivot point $k_0 = 0.05$/Mpc. We fix the the tensor slope to be $n_t = -r/8$. We summarize this information in Table 3.1.

In fact to optimize the MCMC production we use the standard approach of selecting the orthogonal set of the appropriate combinations of cosmological parameters (e.g., see

Parameter	Description	Comment	Prior
ω_b	Physical baryon density	$\omega_b = \Omega_b h^2$	
ω_m	Physical matter density	$\omega_m = \Omega_m h^2$	
Ω_Λ	Dark energy density		
h	Hubble constant in units of 100 km/s/Mpc	$h^2 = \omega_m/(\Omega_t - \Omega_\Lambda)$	$0.45 \leq h \leq 0.90$
τ	Reionization optical depth		$0.0 \leq \tau \leq 0.8$
A_s	Scalar fluctuation amplitude	$\mathcal{P}_0(k)$ at $k_0 = 0.05$/Mpc	
n_s	Scalar spectral index	$n_s = d\ln\mathcal{P}_0(k)/d\ln k$ at $k = k_0$	$0.4 \leq n_s \leq 1.6$
α_s	Running of spectral index	$\alpha_s = d^2\mathcal{P}_0(k)/d\ln k^2$ at $k = k_0$	
r	Tensor to scalar ratio	$r = A_t/A_s$	$r \geq 0$
w	Dark energy equation of state		
Ω_t	Total desity of the universe	$\Omega_t = \Omega_m + \Omega_\Lambda$	$0.5 \leq \Omega_t \leq 1.5$
$\sum m_\nu$	Sum of neutrino masses	3 massive, or 1 massive + 3 massless	$\sum m_\nu \geq 0$
b	Galaxy bias factor	$P_{\rm gal}(k) = b^2 P_{\rm lin}(k)$	$b > 0$

Table 3.1: Cosmological parameters we use to run the MCMCs.

[55, 56]) as acoustic peak scale θ_s, CMB peak suppression factor $e^{-2\tau}$, etc. This parameters effectively diagonalize the covariance matrix of the original parameter set. We do not report the values of these parameters in our results. Also we do not report them for A_s; we present the value of the amplitude of fluctuations σ_8 instead.

3.3 Effects on cosmological parameters of proper likelihood evaluations of low multipole first year WMAP data

This section primarily presents the results of reference [4]. When the WMAP [57, 21] released it first-year data, a question arose about the abnormally low value of the quadrupole, which was also observed by COBE. As was pointed out in [58, 4], it can be explained by the inaccuracy in the calculation of the likelihood function for low WMAP multipoles because of approximate calculation of the tails of the liklihood function away from its peak. Reference [4] also tries to show the effects of the full marginalization of the foreground contamination.

In this section we show the effect on the determination of the cosmological parameters after proper treatment of the above problems.

Figure 3.1 shows the effect of the proper treatment of WMAP likelihood evaluation on the constraint of the matter density Ω_m. We can see that more accurate consideration of the likelihood evaluation prefers a slightly lower value of Ω_m. Thus Table 3.2 shows that the original WMAP analysis gives $\Omega_m = 0.29^{+0.08}_{-0.06}$, whereas e.g. VKP2 mask analysis gives $\Omega_m = 0.24^{+0.07}_{-0.05}$.

Figures 3.2 and 3.3 show the change in the constraints on the slope n_s and running α_s from WMAP analysis together with SDSS galaxies clustering. One can see that the main result here is that the new preferred value of the running is only half a sigma away from zero, as opposed to the original WMAP analysis finding two-sigma deviation of the running from zero. Actually, the simplest Harrison-Zel'dovich power spectrum of primordial fluctuations with $n_s = 1$ and $\alpha_s = 0$ lies in the center of the preferred region. Indeed, there

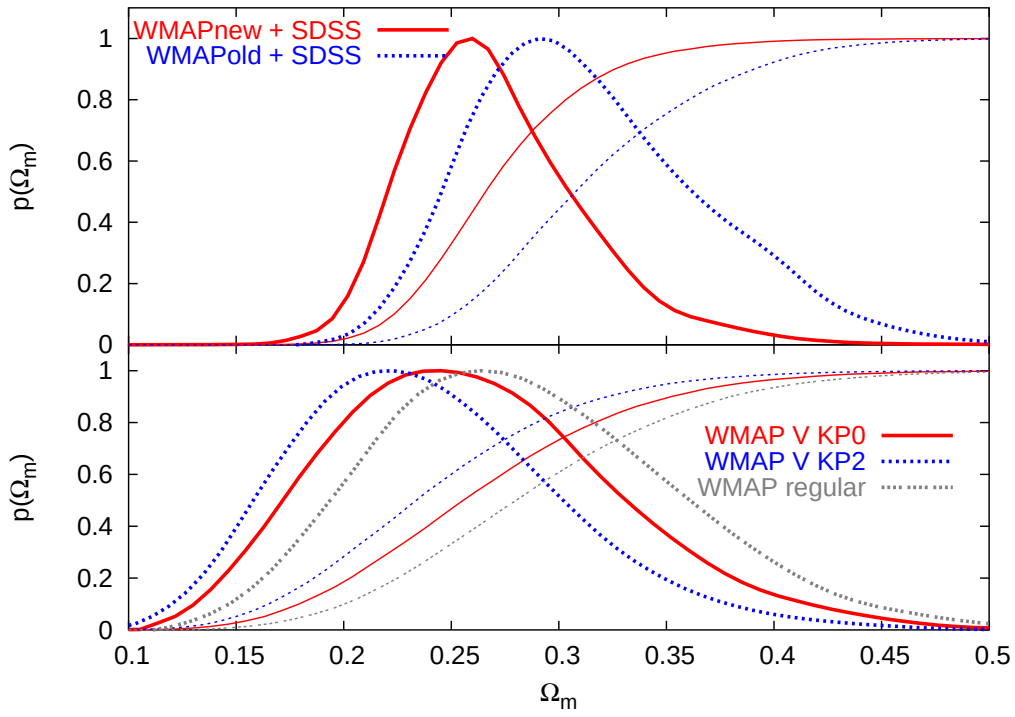

Figure 3.1: Probability distribution $p(\Omega_m)$ and its cumulative value $\int_{-\infty}^{\Omega_m} p(\Omega'_m)d\Omega'_m$ for 5-parameter MCMCs of WMAPext data (bottom) and for 8-parameter MCMCs of WMAPext+SDSS data (top). We present V frequency map and both KP0 and KP2 mask results for the full likelihood analysis of 5-parameters MCMCs of WMAPext data and V KP2 for full likelihood analysis of 8-parameter MCMCs of WMAPext+SDSS data. Also shown for comparison are the results using regular (old) WMAP analysis routine.

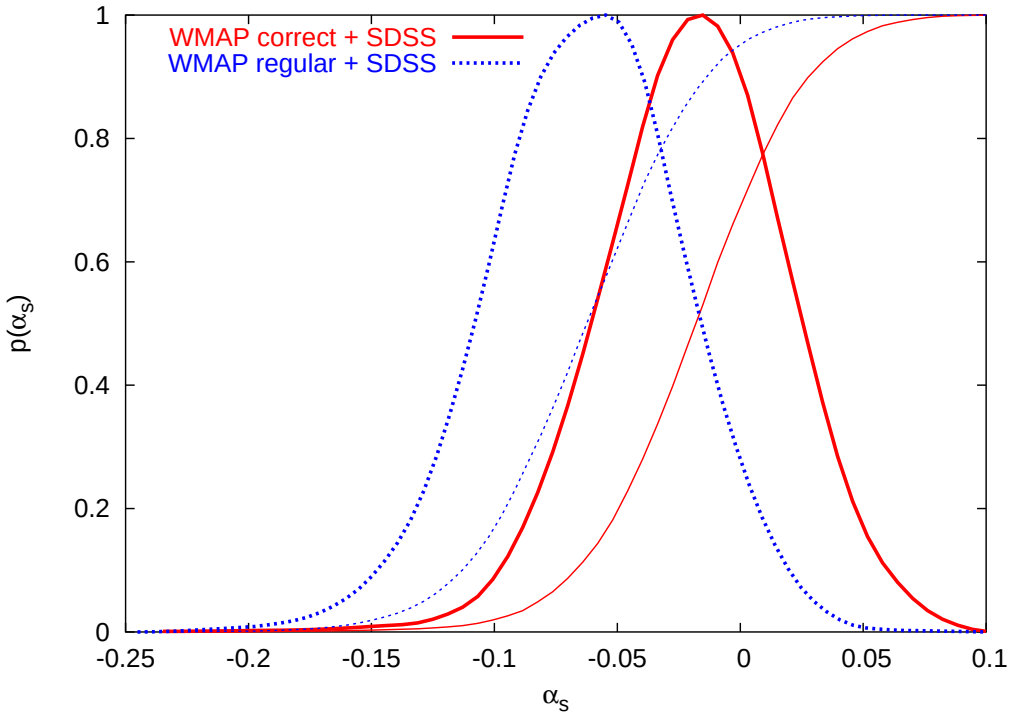

Figure 3.2: Probability distribution $p(\alpha_s)$ and its cumulative value $\int_{-\infty}^{\alpha_s} p(\alpha_s')d\alpha_s'$ for old and new MCMCs using WMAPext+SDSS data. We use V frequency map and KP2 mask in the full likelihood analysis.

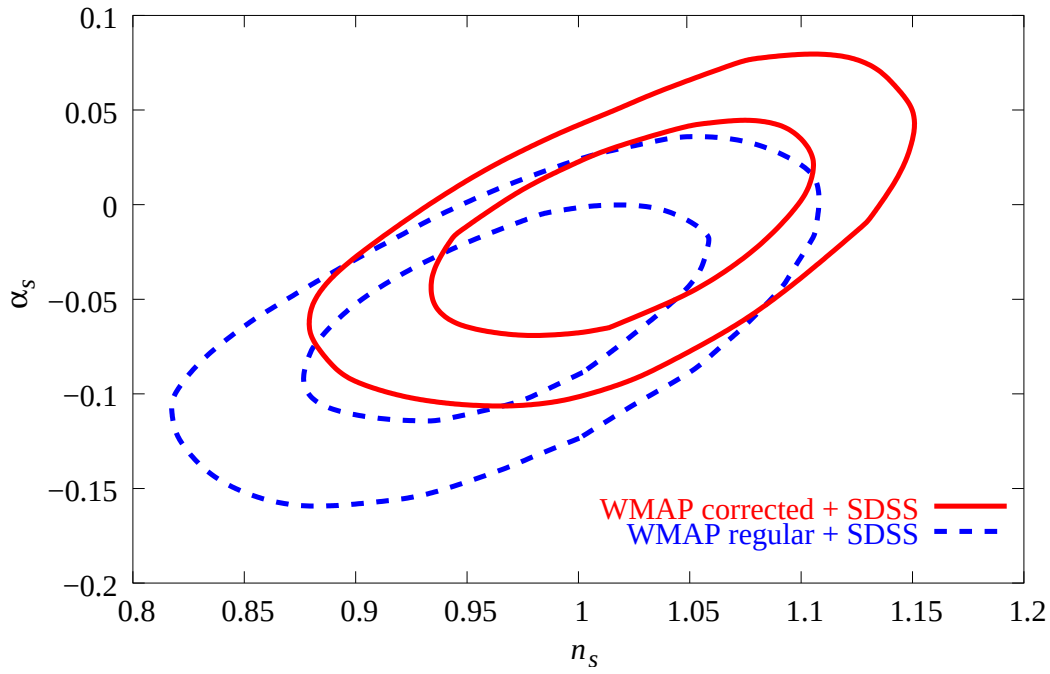

Figure 3.3: Two dimensional contours of 68% and 95% probability in (α_s, τ) and $(\alpha_s, z_{\rm ri})$ plane from WMAP+VSA and WMAP+VSA+SDSS data.

is a degeneracy between spectral index n_s and running α_s in CMB data. By reducing the value of α_s we also shift the preferred value of n_s closer to 1.

Figure 3.4 shows the two-dimensional contours in $\alpha_s - \tau$ and $\alpha_s - z_{\rm ri}$ plane with just CMB data and CMB and SDSS data together. One can see that without the galaxy clsutering data there is a strong degeneracy between the running α_s and the optical depth to reionization τ which doesn't allow us to constrain either of them. Addition of the SDSS galaxy information helps us to resolve the degeneracy and allows us to forbid the area with extremely high running of $\alpha_s \sim -0.15$.

Tables 3.2 and 3.3 show the constraints on the rest of the parameters. One can see that the effect on most other parameters is within one-sigma of the original value. For example constraint on tensor component from the original analysis is $T/S < 0.76$ at 95% confidence level, it changes to $T/S < 0.81$ for the new modified likelihood calculation.

To conclude, we have shown that the effects of the proper likelihood evaluation and marginalization are really important for estimating the cosmological parameters from WMAP

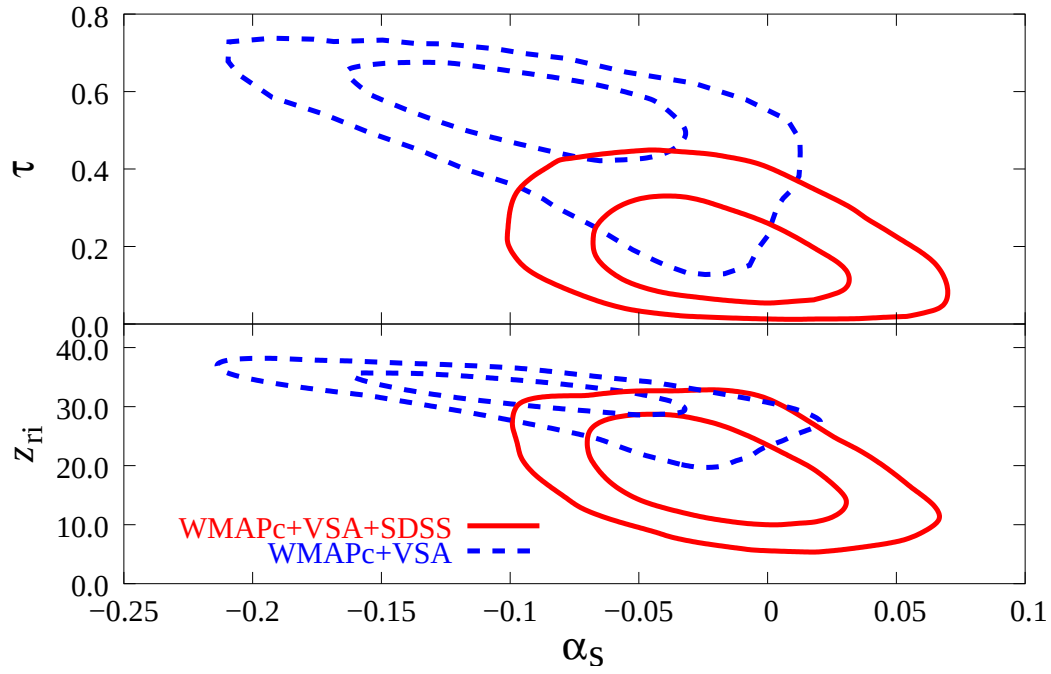

Figure 3.4: Blue dashed contours show 1 and 2-σ contours for the CMB data in τ and α_s plane. One can see that the addition of the small scale information from the clustering of galaxies from SDSS (red solid contours) significantly affects the location of the countours in this plane. This is mostly due to the fact that CMB alone (first year WMAP and VSA) does not constrain reionization well.

	5p old	5p VKP2	5p VKP0	8p old	8p VKP2
$10^2\omega_b$	$2.40^{+0.06\ +0.12}_{-0.06\ -0.13}$	$2.38^{+0.06\ +0.13}_{-0.07\ -0.13}$	$2.39^{+0.06\ +0.13}_{-0.06\ -0.13}$	$2.37^{+0.17\ +0.35}_{-0.16\ -0.32}$	$2.49^{+0.19\ +0.39}_{-0.17\ -0.34}$
Ω_m	$0.29^{+0.08\ +0.16}_{-0.06\ -0.11}$	$0.24^{+0.07\ +0.15}_{-0.05\ -0.10}$	$0.26^{+0.07\ +0.16}_{-0.06\ -0.11}$	$0.20^{+0.07\ +0.16}_{-0.06\ -0.10}$	$0.15^{+0.06\ +0.13}_{-0.04\ -0.07}$
$\omega_{\rm cdm}$	$0.12^{+0.017\ +0.03}_{-0.017\ -0.03}$	$0.11^{+0.016\ +0.03}_{-0.016\ -0.03}$	$0.11^{+0.017\ +0.03}_{-0.016\ -0.03}$	$0.10^{+0.017\ +0.03}_{-0.017\ -0.03}$	$0.09^{+0.016\ +0.03}_{-0.015\ -0.03}$
τ	$0.17^{+0.04\ +0.08}_{-0.04\ -0.09}$	$0.21^{+0.04\ +0.07}_{-0.04\ -0.08}$	$0.19^{+0.04\ +0.08}_{-0.04\ -0.08}$	$0.23^{+0.05\ +0.07}_{-0.08\ -0.16}$	$0.24^{+0.05\ +0.06}_{-0.08\ -0.17}$
σ_8	$0.94^{+0.07\ +0.13}_{-0.08\ -0.17}$	$0.90^{+0.08\ +0.15}_{-0.09\ -0.19}$	$0.92^{+0.08\ +0.15}_{-0.09\ -0.19}$	$0.81^{+0.12\ +0.25}_{-0.13\ -0.26}$	$0.75^{+0.13\ +0.24}_{-0.13\ -0.25}$
h	$0.72^{+0.05\ +0.10}_{-0.05\ -0.08}$	$0.75^{+0.05\ +0.11}_{-0.05\ -0.09}$	$0.73^{+0.05\ +0.11}_{-0.05\ -0.09}$	$0.78^{+0.08\ +0.19}_{-0.07\ -0.13}$	$0.87^{+0.09\ +0.19}_{-0.08\ -0.15}$
T/S	0	0	0	< 0.76 (95%)	< 0.81 (95%)
n_s	1	1	1	$0.95^{+0.07\ +0.14}_{-0.07\ -0.15}$	$1.02^{+0.07\ +0.15}_{-0.07\ -0.15}$
α_s	0	0	0	$-0.08^{+0.05\ +0.10}_{-0.06\ -0.13}$	$-0.04^{+0.05\ +0.10}_{-0.06\ -0.13}$

Table 3.2: Median value, 1σ and 2σ constraints on cosmological parameters for various MCMCs based on WMAP data alone. 5p denotes varying 5 basic cosmological parameters in MCMCs, while 8p stands for 8 parameter chains. Old stands for the evaluation of the WMAP likelihood using the current WMAP provided software, VKP2 is our new exact likelihood evaluation analysis of V maps using KP2 mask and VKP0 is the same for KP0 mask.

	8p SDSS+old	8p SDSS+VKP2	8p SDSS+WKP2	7p SDSS+VSA+VKP2
$10^2\omega_b$	$2.40^{+0.16\ +0.32}_{-0.16\ -0.30}$	$2.48^{+0.16\ +0.30}_{-0.16\ -0.31}$	$2.47^{+0.16\ +0.31}_{-0.16\ -0.30}$	$2.34^{+0.18\ +0.52}_{-0.15\ -0.28}$
Ω_m	$0.31^{+0.06\ +0.13}_{-0.05\ -0.08}$	$0.27^{+0.05\ +0.11}_{-0.03\ -0.06}$	$0.28^{+0.05\ +0.11}_{-0.04\ -0.07}$	$0.30^{+0.06\ +0.12}_{-0.05\ -0.10}$
$\omega_{\rm cdm}$	$0.128^{+0.009\ +0.019}_{-0.008\ -0.016}$	$0.121^{+0.008\ +0.017}_{-0.007\ -0.014}$	$0.123^{+0.008\ +0.017}_{-0.007\ -0.014}$	$0.123^{+0.008\ +0.017}_{-0.008\ -0.018}$
τ	$0.20^{+0.07\ +0.09}_{-0.08\ -0.14}$	$0.20^{+0.07\ +0.09}_{-0.08\ -0.14}$	$0.20^{+0.07\ +0.09}_{-0.08\ -0.14}$	$0.19^{+0.11\ +0.26}_{-0.08\ -0.13}$
σ_8	$0.98^{+0.08\ +0.16}_{-0.09\ -0.16}$	$0.97^{+0.09\ +0.16}_{-0.09\ -0.16}$	$0.97^{+0.09\ +0.16}_{-0.09\ -0.16}$	$0.93^{+0.12\ +0.29}_{-0.08\ -0.13}$
h	$0.70^{+0.05\ +0.09}_{-0.05\ -0.09}$	$0.73^{+0.04\ +0.08}_{-0.04\ -0.09}$	$0.73^{+0.04\ +0.08}_{-0.04\ -0.09}$	$0.70^{+0.05\ +0.14}_{-0.05\ -0.08}$
T/S	< 0.46 (95%)	< 0.46 (95%)	< 0.47 (95%)	0
n_s	$0.97^{+0.06\ +0.11}_{-0.06\ -0.12}$	$1.01^{+0.05\ +0.10}_{-0.06\ -0.11}$	$1.02^{+0.05\ +0.10}_{-0.06\ -0.11}$	$0.97^{+0.06\ +0.16}_{-0.06\ -0.11}$
α_s	$-0.060^{+0.038\ +0.074}_{-0.039\ -0.083}$	$-0.015^{+0.036\ +0.072}_{-0.037\ -0.080}$	$-0.032^{+0.036\ +0.072}_{-0.038\ -0.080}$	$-0.022^{+0.034\ +0.069}_{-0.032\ -0.062}$

Table 3.3: Same as Table 3.2 for WMAP+SDSS (8-parameter MCMCs with regular (old) or corrected (exact likelihood) analysis). The new analysis uses V KP2 with full marginalization and W KP2 with dust marginalization only. We also give WMAP+SDSS+VSA (7-parameters). For the latter case we do not impose $\tau < 0.3$.

data. Thus the correct calculation prefers lower value for the matter density Ω_m, less significant running α_s and slightly higher value of the slope n_s.

3.4 Effect on cosmological parameters of Sunyaev-Zel'dovich effect in WMAP

In the literature, several groups [59, 60, 61, 62, 63, 64, 65, 66, 67, 68, 69, 70, 71] have tried to determine the level of Sunyaev-Zel'dovich (SZ) contamination in WMAP data. Most of them came to different conclusions, some of the recent ones (e.g. [69])found a high level of SZ and, therefore, questioned the validity of the WMAP cosmological parameter estimations.

We describe amplitude of SZ with B, the ratio of the SZ power spectrum and the predicted spectrum, assuming they have the same shape. Thus the SZ amplitude is dimensionless, and has a theoretically predicted value $B = 1$ for $\sigma_8 = 0.9$ using the halo models of [72].

In this section we estimate how much SZ signal is in the WMAP C_l power spectrum, and investigate the effect of SZ on the determination of the cosmological parameters. For this purpose we use the Markov Chain Monte Carlo (MCMC) approach, using software described in more detail elsewhere [3, 4].

We ran two MCMCs, one without SZ and one allowing for an unconstrained SZ contribution. We built a third chain from the second by importance sampling, allowing for an SZ component but constraining it to limits derived based on frequency information in the previous section. We used the WMAP likelihood routine [57, 21]. Each of the chains contains 100,000 total chain elements. The success rate is 45–55 percent, the correlation length is 13–20 elements, and the effective length is 5,000–10,000 elements. Each chain comprises 23 independent sub-chains and, in terms of Gelman and Rubin $\hat{R}$-statistics [53], we find the chains are sufficiently converged and mixed ($\hat{R} < 1.01$, compared to the recommended value of $\hat{R} < 1.2$).

In the second chain, we added to the power spectrum an SZ-shaped contribution, parameterized in terms of amplitude B. The WMAP power spectrum combines the Q, V and W bands in different ratios at each l, so the shape of the SZ contribution to the WMAP power spectrum is not exactly given by the single frequency SZ template, because the effective frequency for every l varies. This dependence is small and we ignore it here. We find that the SZ contribution to the WMAP combined temperature power spectrum, dominated by V and W channels, may be approximated as 75% the contribution in RJ. One could also add additional CMB experiments (e.g. CBI, VSA, *etc.*) into the analysis, but this would incur complications to account for the different frequencies of these experiments. In the third chain we add our multi-frequency analysis limit as an additional constraint.

We consider only the simplest model required by the data plus the SZ component, since we want to analyze the effect of the latter on the cosmological parameters. WMAP temperature data require neither tensor modes nor curvature nor running of the primordial power spectrum of the scalar perturbations, so we do not consider them.

We work in a seven parameter space:

$$\mathbf{p} = \{\omega_b,\ \omega_{\rm cdm},\ \Omega_m,\ \tau,\ A_s,\ n_s,\ B\}. \tag{3.3}$$

Here $\omega_b = \Omega_b h^2$ is the baryonic content of the universe, $\omega_{\rm cdm} = \Omega_{\rm cdm} h^2$ is the physical density of the cold dark matter content, $\Omega_m = \Omega_{\rm cdm} + \Omega_b = 1 - \Omega_\Lambda$ is the matter density today, τ is the optical depth to reionization, A_s is the amplitude of the primordial scalar perturbations, n_s is the primordial slope, and as before B is the amplitude of the SZ power spectrum.

To reduce the degeneracies while running the MCMCs, we use ω_b, $\omega_{\rm cdm}$, angular size of the sound horizon Θ_s, $\lg A_s$, n_s, $\lg A_s - \tau - 0.5\lg(\omega_b + \omega_{\rm cdm})$, and B, instead of the parameters in equation 3.3. We adopt broad flat priors on these parameters, and additionally require $\tau < 0.3$.

We find that the amplitude of an SZ-shaped component to the WMAP power spectrum is limited to $B < 7.1$ at 95 percent confidence. This limit means that the contribution to the WMAP temperature power spectrum at the first peak is below 5 percent. This is a

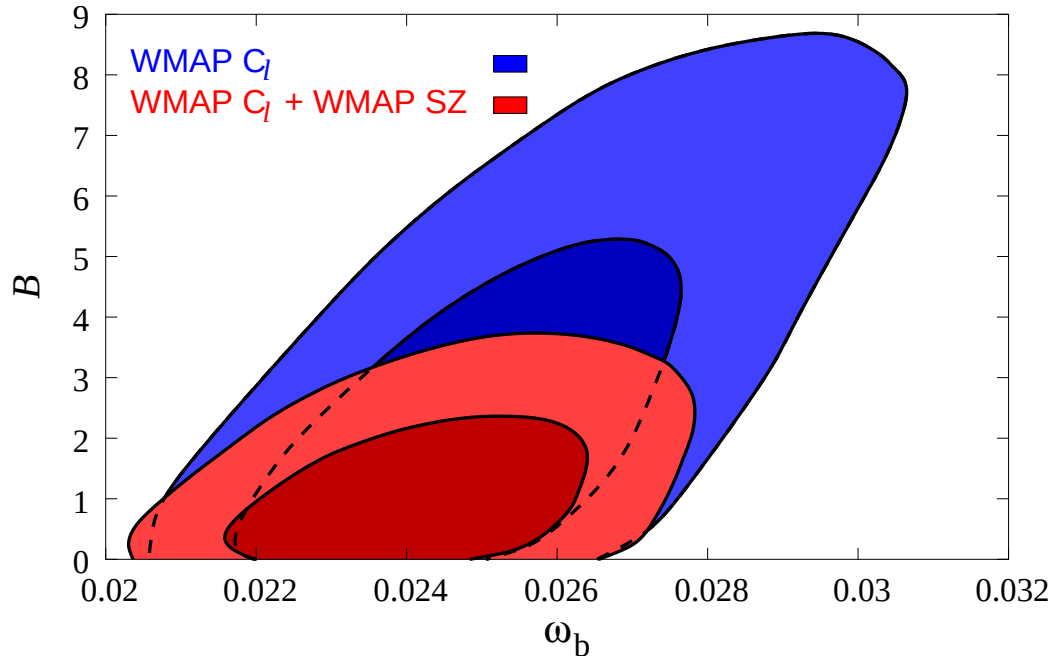

Figure 3.5: We show two-dimensional contours of 68% and 95% confidence levels in (ω_b, B) plane. The larger (blue) contours show the degeneracy using the WMAP combined temperature power spectrum without any prior on SZ. The smaller (red) contours include our multi-frequency cross-spectrum analysis as a prior. $B = 1$ is expected from halo models for SZ when $\sigma_8 = 0.9$.

weaker limit than from the combination of cross-spectra, where a factor of 2 better limit was found.

Table 3.4 shows the comparison of the two MCMCs, showing the effect of including SZ in the analysis. The inclusion of the additional parameter B into the likelihood analysis affects only the determination of the baryon physical density ω_b. Without SZ we find $\omega_b = 0.0235$, whereas with SZ we find $\omega_b = 0.0251$, which is shifted by about 1.5σ away from the earlier value. The confidence contours in the (ω_b, B) plane are shown in Figure 3.5, showing that there is a degeneracy between these two parameters. However, we can and should also use the constraint from our multi-frequency cross-spectrum analysis as a prior. We can include the Gaussian likelihood for B from reference [46], and perform importance sampling of the chain with SZ. We then find $\omega_b = 0.0243$, different from the case without SZ by 0.6σ. The likelihood contours including the prior are also shown in Figure 3.5. The other parameters

	no SZ	with SZ, no SZ prior	with SZ prior
B	0	< 7.1 (95%)	< 2.9 (95%)
$\omega_b \times 10^2$	$2.35^{+0.14\ +0.28}_{-0.13\ -0.26}$	$2.51^{+0.21\ +0.47}_{-0.18\ -0.33}$	$2.43^{+0.15\ +0.30}_{-0.15\ -0.29}$
Ω_m	$0.245^{+0.07\ +0.15}_{-0.06\ -0.10}$	$0.234^{+0.07\ +0.15}_{-0.06\ -0.10}$	$0.243^{+0.07\ +0.15}_{-0.06\ -0.10}$
$\omega_{\rm cdm}$	$0.111^{+0.016\ +0.033}_{-0.015\ -0.029}$	$0.111^{+0.016\ +0.033}_{-0.016\ -0.030}$	$0.111^{+0.016\ +0.033}_{-0.016\ -0.031}$
τ	$0.19^{+0.07\ +0.10}_{-0.08\ -0.14}$	$0.20^{+0.07\ +0.10}_{-0.08\ -0.14}$	$0.19^{+0.07\ +0.10}_{-0.08\ -0.14}$
σ_8	$0.88^{+0.12\ +0.25}_{-0.11\ -0.20}$	$0.86^{+0.12\ +0.24}_{-0.11\ -0.22}$	$0.87^{+0.12\ +0.23}_{-0.11\ -0.22}$
h	$0.74^{+0.06\ +0.12}_{-0.05\ -0.09}$	$0.76^{+0.07\ +0.14}_{-0.06\ -0.11}$	$0.75^{+0.06\ +0.13}_{-0.05\ -0.10}$
n_s	$0.99^{+0.04\ +0.07}_{-0.04\ -0.07}$	$0.99^{+0.04\ +0.07}_{-0.04\ -0.07}$	$0.99^{+0.04\ +0.07}_{-0.04\ -0.07}$

Table 3.4: The first two columns contain the median value and 1- and 2σ constraints on cosmological parameters for two MCMCs without and with a Sunyaev-Zeldovich component in the C_l power spectrum from WMAP data alone. For both chains there was an imposed prior of $\tau < 0.3$. The third column shows the constraints when the limit on SZ from our cross-spectrum estimator is applied as a prior.

are much less affected by the SZ.

The next largest deviation from the first chain to the second is a shift in the median h of about 0.3σ towards higher value, which is not statistically significant and the effect is even smaller if the constraints from previous section are added to the chains.

By searching for an SZ-shaped component in the WMAP combined spectrum with a Markov chain Monte Carlo we do not find any evidence of a signal, but we can only set a weak limit. Another method [46] sets a stronger limit, at 95% confidence the amplitude of SZ is below 2% of the CMB at the position of first peak in W band. Combining the analyses, we show that the cosmological parameters are not affected by the SZ within the range allowed by the multi-frequency analysis.

Chapter 4

Cosmological parameter analysis including Ly-alpha forest

4.1 Introduction

Many different cosmological observations over the past decade have helped build what is now called the standard cosmological model. These observations suggest that the universe is spatially flat, contains baryons, dark matter and dark energy. The primordial spectrum of fluctuations is approximately scale invariant and initial fluctuations are Gaussian and adiabatic. This standard cosmological model can be described in terms of only a few parameters, which explain a large number of observations, such as the cosmic microwave background (CMB), galaxy clustering, supernova data, Hubble parameter determinations, and weak lensing. The latest results come from Wilkinson Microwave Anisotropy Probe (WMAP) CMB measurements [73, 57, 74], Sloan Digital Sky Survey (SDSS) and Two degree Field (2dF) galaxy clustering analyses [1, 75, 76], and from the latest Supernovae type Ia (SNIa) data [77, 78].

While the standard model is observationally well justified, many theoretical models predict that there should be observable deviations from it. Perhaps the best motivated among these are the predictions of how the universe was seeded by initial fluctuations.

The standard paradigm is inflation, which predicts that the fluctuations should be almost, but not exactly, scale invariant [27]. A typical deviation for the slope of the primordial perturbations is predicted to be of order of a few parts in a hundred away from its scale invariant value $n_s = 1$ and could be of either sign. This should be observable with high precision cosmological observations. Despite tremendous progress over the past couple of years the current constraints do not yet distinguish between different inflationary models [23, 39]. Alternative models also predict deviations from scale invariance similar to inflation [79]. Another prediction of these models is that the rate of change of slope with scale is rather small, $\alpha_s = dn_s/d\ln k \sim (n_s - 1)^2 \sim 10^{-3}$, which should not be observable in the near future. A third prediction that can distinguish among the different models is the amount of tensor perturbations they predict. Some models predict no detectable tensor contribution [27, 80], while other models predict a tensor contribution to the large scale CMB anisotropies comparable to that from scalars. It is clear that determining the shape and amplitude of the scalar and tensor primordial power spectra will be one of the key tests of various models of structure formation.

Current observational constraints on the primordial power spectrum are mostly limited to scales larger than $10h^{-1}$Mpc. There are various reasons for this: CMB fluctuations are damped on small scales and their detection would require high resolution, low noise detectors, which are only now being built. Even with sufficient signal-to-noise and angular resolution there may be secondary anisotropies that may contaminate the signal from primary anisotropies. On small scales, matter undergoes strongly nonlinear evolution, which erases the initial spectrum of fluctuations and prevents galaxy clustering and weak lensing surveys from extracting this information. On the other end, the largest observable scale is the horizon scale seen by CMB fluctuations. The small number of available modes on the sky prevents one from accurately determining the primordial spectrum on these scales from the CMB. The largest scales probed by galaxy clustering are even smaller. As a result, the primordial power spectrum is currently probed over a relatively narrow range of scales and the shape of the primordial power spectrum cannot be accurately determined.

To improve these constraints one should determine the fluctuation amplitude on smaller scales. Nonlinear evolution prevents one from obtaining useful information at $z = 0$, so one must look for probes at higher redshift. Of the current cosmological probes, the Ly-α forest – the absorption observed in quasar spectra by neutral hydrogen in the intergalactic medium (hereafter IGM) – has the potential to give the most precise information on small scales [81]. It probes fluctuations down to megaparsec scales at redshifts between 2-4, so nonlinear evolution, while not negligible, has not erased all of the primordial information.

In this chapter we combine CMB/LSS constraints with the new analysis of the Ly-α forest from SDSS data [82]. The Sloan Digital Sky Survey [83] uses a drift-scanning imaging camera [84] and a 640 fiber, double spectrograph on a dedicated 2.5 m telescope. The SDSS data sample in data release two [85] consists of more than 3000 QSO spectra with $z > 2.2$, nearly two orders of magnitude larger than previously available [86, 87, 88]. This large data set allows one to determine the amplitude of the flux power spectrum to better than 1%. Theoretical analysis of this flux power spectrum shows that at the pivot point k=0.009 s/km in velocity coordinates, which is close to k=1h/Mpc in comoving coordinates for standard cosmological parameters, the power spectrum amplitude is determined to about 15% and the slope to about 0.05, with the error budget dominated by uncertainties in theoretical modelling [89, 90]. This is an accuracy comparable to that achieved by WMAP. More importantly, it is at a much smaller scale, so combining the two leads to a significant improvement in the constraints on primordial power spectrum shape over what can be achieved from each data set individually.

A second theoretical prediction where the basic cosmological model is expected to require modifications is that neutrinos have mass. Atmospheric mixing and solar neutrino results suggest that the total minimum neutrino mass is about 0.06eV [91, 92, 93]. These observations are only sensitive to relative neutrino mass differences and not to the absolute neutrino mass itself. Cosmology on the other hand can weigh neutrinos directly. Massive neutrinos slow down the growth of structure on small scales and modify the amplitude and shape of the matter power spectrum. They also modify the CMB power spectrum. If

one measures both the CMB and matter power spectra with high precision across a wide range of redshifts and scales then one can determine the neutrino mass with high accuracy [94]. The question of neutrino mass is also interesting in light of recent Los Alamos Liquid Scintillator Neutrino Detector (LSND) experimental results, which, if taken at a face value, suggest $m_\nu > 0.9$eV [95, 96], which should be observable by cosmological neutrino weighing.

A third theoretical prediction of departures from the standard model, and one whose consequences would be particularly far reaching, is that dark energy is not simply a cosmological constant introduced already by Einstein, but something more complicated and dynamical in nature. In the case where dark energy is a scalar field one would expect that it has a kinetic energy term in addition to the potential term, which modifies its equation of state. This is expected to evolve with time, but theoretical predictions are rather uncertain and are suggestive at best. A change in equation of state changes both the rate of growth of structure and the angular size of the acoustic horizon in the CMB. As a result these changes can be observed both through the CMB and by comparing the growth of structure at different redshifts.

Many different methods have been discussed in the literature on how to improve the current constraints from methods such as supernovae type Ia (SNIa), CMB, weak lensing, and cluster abundances. One method to constrain the nature of dark energy that has not attracted much attention, yet has the potential to produce results on a relatively short time scale, is comparing measurements of amplitude of fluctuations at high redshift from the Lyα forest and CMB to that at low redshift from galaxy clustering. Dark energy affects the rate of growth of structure, especially for $z < 1$ where dark energy is dynamically important. In this paper we combine WMAP and SDSS Lyα forest measurements at high redshifts, where dark energy is expected to be negligible, with the amplitude determination at $z = 0.1$ from the SDSS galaxy bias analysis [47]. In general, galaxy clustering is believed to be proportional to matter clustering on large scales up to a constant of proportionality. This constant, the so called bias, is a free parameter that cannot be determined from the clustering analysis itself. There are many different methods for how to determine the bias

and thus the amplitude of matter fluctuations such as redshift space distortions [97, 1], the bispectrum [98], or weak lensing [99, 100], but the current constraints are weak. A recent analysis of the luminosity dependence of galaxy clustering [1], combined with a determination of the halo mass distribution for these galaxies, provides a new constraint on the bias and amplitude of fluctuations in SDSS data [47].

One difference of the current paper in comparison with previous analyses of this type is that we present 68.32%, 95.5% and 99.86% confidence intervals (we denote these the 1, 2, and 3-σ intervals, but note that they do not depend on the assumption of Gaussianity in the error distribution) on all the parameters (or 95% and 99.9% confidence level upper limits in the case of no detections). Sometimes the 3-σ intervals can be significantly different from 3 times the corresponding 1-σ intervals. This can happen if there are degeneracies in the data that appear to be broken at 1-σ, but that the 2 or 3 σ contours allow. In this case the 3-σ constraints are weaker than the corresponding 1-σ intervals would suggest. The opposite can happen as well, especially if there is a natural boundary that the parameter cannot cross (such as a parameter being positive definite). More generally, presenting 1-σ contours alone is not very meaningful, since whatever is within 1-σ is essentially a good fit to the data. One can argue that the goal of observations is to exclude regions of parameter space and this is much better represented by reporting 2 and 3-σ contours than the best fit value and its 1-σ range.

Another issue that we address in detail is the robustness of the constraints against the number of parameters one is exploring. Sometimes the constraints change significantly if new parameters are added to the mix because these new parameters are degenerate with parameters one is interested in. However, often the quality of the fit is not improved at all and moreover these new parameters may not be well motivated from the perspective of fundamental theories or other considerations. In this case one is entitled to adopt an Occam's razor argument against the introduction of these parameters in the estimation. To some extent this is always a subjective procedure, since what is natural for one person may not be for someone else. It has also been argued that one should pay a penalty for each new

parameter that is introduced which does not improve the quality of the fit [40]. However, this procedure is also poorly defined and there is no unique choice for the penalty. In this paper we explore both the solutions with the minimum number of parameters as well as with several additional parameters. We believe that there is merit to the approach which parametrizes the constraints with as few parameters as possible, so our main results are given for this case. However, one also wants to know how robust and model independent are the constraints, which we explore by adding several additional parameters to the analysis.

The outline of this paper is as follows. We first present the method, then our basic results in several tables and then discuss them in detail. We focus particularly on the question of how have the new results improved upon the previous constraints and how robust are the conclusions upon removing one or more of the data ingredients. The latter is particularly interesting in light of possible systematic effects that may be present both in the new analyses of Lyα forest and bias as well as in previous analyses of WMAP, SDSS galaxy clustering, and SNIa.

4.2 Method

We combine the constraints from the SDSS Ly-α forest [82] with the SDSS galaxy clustering analysis [1], SDSS bias analysis [47], and CMB power spectrum observations from WMAP [73, 57, 74]. We verified that including CBI, VSA, and ACBAR [101, 102, 103] makes very little difference in the final results and we do not include them in the current analysis. Similarly, we verified that including the latest 2dF power spectrum analysis [76] in addition to SDSS does not make much difference, so we do not include those constraints either. We could have used 2dF constraints instead of SDSS, but we chose not to because for 2dF the bias constraints are somewhat weaker [98] and we would like to have an independent verification of results that use the 2dF bias [2]. We will thus refer to CMB constraints as WMAP, to LSS/galaxy clustering constraints as SDSS-gal, to SDSS bias constraints as SDSS-bias and to SDSS Ly-α forest constraints as SDSS-lya. We have added earlier Lyα forest constraints in a weak form [87, 104], which have a small, but not negligible effect. We

do not include more recent Lyα forest constraints [86, 105] since there are signs of systematic discrepancy and/or underestimation of errors when compared to SDSS Lyα forest data [82]. To this we add the latest supernova constraints as given in [77]. We do not use this full combination in all calculations, since we want to emphasize what the new constraints bring to the mix and we want to explore the sensitivity of the constraints to individual data sets. For example, for the investigation of the shape of the primordial power spectrum we perform the analysis using WMAP+SDSS-lya alone and show that this combination in itself suffices to constrain the running by a factor of 3 better than combining everything else together. We also perform several analyses by dropping one of the constraints and explore the robustness of the conclusions. For example, we explore the constraints on the dark energy equation of state with and without SNIa and with and without SDSS-bias and SDSS-lya.

Our implementation of the Monte Carlo Markov Chain (MCMC) method [3] uses CMBFAST [54] version 4.5.1[1] , outputting both CMB spectra and the corresponding matter power spectra $P(k)$. We evolve all the matter power spectra to a high k using CMBFAST and we do not employ any analytical approximations. We output the transfer functions at the redshifts of interest, between 2-4 for SDSS-Lyα forest and 0.1 for SDSS-gal. Note that for massive neutrinos the high precision (HP) option must be used to achieve sufficient accuracy in the transfer function.

A typical run is based on 16-24 independent chains, contains 50,000-200,000 chain elements and requires several days of running on a computer cluster in a serial mode of CMBFAST. The acceptance rate was of order 30-50%, correlation length 10-30 and the effective chain length of order 3,000-20,000 (see [39] for definitions of these terms). In terms of Gelman and Rubin $\hat{R}$-statistics [53] we find the chains are sufficiently converged and mixed, with $\hat{R} < 1.05$, significantly more conservative than the recommended value $\hat{R} < 1.2$.

Our most general cosmological parameter space is

$$\mathbf{p} = (\tau, \omega_b, \omega_m, \sum m_\nu, \Omega_\lambda, w, \Delta^2_{\mathcal{R}}, n_s, \alpha_s, r), \tag{4.1}$$

where τ is the optical depth, $\omega_b = \Omega_b h^2$, where Ω_b is baryon density in units of the critical

[1] available at cmbfast.org

density and h is the Hubble constant in units of 100km/s/Mpc, $\omega_m = \Omega_m h^2$ where Ω_m is matter density in units of the critical density, $\sum m_\nu$ is the sum of massive neutrino masses (assuming either 3 degenerate neutrino families or 1 massive neutrino family in addition to 3 massless), Ω_λ is the dark energy density today and w its equation of state (which is in general time dependent). Our pivot point for the primordial power spectrum parameterization is at $k_{\rm pivot} = 0.05$/Mpc and we expand the primordial power spectrum at that point, defining the amplitude of curvature perturbations $\Delta^2_{\mathcal{R}}$, slope n_s, and its running $\alpha_s = dn_s/d\ln k$. The choice of the pivot point is somewhat arbitrary, but is meant to represent the scale somewhere in the middle of the observational range. In this case the largest scales are probed by the CMB ($k \sim 10^{-3}$/Mpc) and the smallest scales are probed by the Lyα forest ($k \sim 1$/Mpc). In addition, this scale has been (arbitrarily) chosen as a pivot point in CMBFAST and has been used by previous analyses, which facilitates the comparison. Note that there is no Hubble parameter h in the definition of the pivot point: if CMB data are used there is no advantage in defining the scale by taking out the Hubble constant, unlike the case of galaxy clustering and Lyα forest.

We parametrize tensors in terms of their amplitude Δ^2_h, and define the ratio relative to scalars as $r = T/S = \Delta^2_h/\Delta^2_{\mathcal{R}}$. This is also defined at the pivot point $k = 0.05$/Mpc, just as for the scalar amplitude, slope and running. We fix the tensor slope n_T using $r = -8n_T$. We do not allow for non-flat models, since curvature is already tightly constrained by CMB and other observations [2]. In addition, we will be testing particular classes of models, such as inflation, which predict $K = 0$. For the more general models, such as those with freedom in the dark energy equation of state, relaxing this assumption can lead to a significant expansion of errors [39]. We are therefore testing a particular class of inflation inspired models with $K = 0$ and not presenting model independent constraints on the equation of state. Note that this assumption is implicit in most of the constraints published to date, including those from the SNIa teams, which often assume a CMB prior on Ω_m [77]. This prior is affected by the choice of parameter space one is working in and a self-consistent treatment is required. CMB constraints on Ω_m using an analysis where the equation of

state or curvature are not varied need not equal those where these are varied. We follow the WMAP team in imposing a $\tau < 0.3$ constraint. Upcoming polarization data from WMAP will allow a verification of this prior.

From this basic set of parameters we can obtain constraints on several other parameters, such as the baryon and matter densities Ω_b and Ω_m, Hubble parameter $h = H_0/(100\text{km/s/Mpc})$ and amplitude of fluctuations σ_8. Since we do not allow for curvature we have $\Omega_\lambda = 1 - \Omega_m$ and we use Ω_m in all tables. In fact, our primary parameter is the angular scale of the acoustic horizon, which is tightly constrained by the CMB. Similarly, although we use $\Delta^2_{\mathcal{R}}$ as the primary parameter in the MCMC we present the amplitude in terms of the more familiar σ_8. In addition to the cosmological parameters above we also keep track of several parameters related to the specific tracers, described below.

4.3 Results

The basic results for many different MCMC runs are given in Tables 4.1–4.4. We give results for many different parameter combinations and different experiment combinations, with the purpose of assessing the robustness of constraints on both the data and parameter space. For most of the parameters we quote the median value (50%), [15.84%,84.16%] interval ($\pm 1\sigma$), [2.3%,97.7%] interval ($\pm 2\sigma$) and [0.13%,99.87%] interval ($\pm 3\sigma$). These are calculated from the cumulative one-point distributions of MCMC values for each parameter and do not depend on the Gaussian assumption. For the parameters without a detection we quote a 95% confidence upper limit and a 99.9% confidence upper limit. We have found that our MCMC gives a reliable estimate of 3-sigma contours for one-dimensional projections. The corresponding 2-d projections are however very noisy and we do not plot 3-sigma contours in our 2-d plots.

All of the restricted parameter space fits are acceptable based on χ^2 values, starting from the basic 6-parameter model $\mathbf{p} = (\tau, \omega_b, \omega_m, \Omega_\lambda = 1 - \Omega_m, \Delta^2_{\mathcal{R}}, n_s)$. We denote this as 6-p in the tables. Introducing additional parameters such as tensors, running, equation of state, or neutrino mass does not improve the fits. We do not report the values of nuisance

parameters such as the galaxy bias or Lyα forest mean flux, temperature-density relation, or filtering length. Some of these are discussed elsewhere [47, 89]. When comparing the improvements over previous analyses we try to compare the results to our own MCMC analysis of previous data. This is because small changes in the treatment, such as assumed priors, can affect the parameters and so the constraints between different groups are not directly comparable. When comparing our analysis to [39] we find in general a very good agreement between the two, even though our MCMC implementation is independent. Our primary goal is to determine how much the new data improve over the previous situation and to answer this it is best to perform identical analyses with and without the new data. Below we discuss the results from these tables in more detail.

4.3.1 Amplitude of fluctuations

From Tables 4.1–4.4 one can see that the value of σ_8 is remarkably tight. For 6-p models (Table 4.1) we find

$$\sigma_8 = 0.897^{+0.033\ +0.065\ +0.097}_{-0.031\ -0.058\ -0.088} \tag{4.2}$$

This value does not change significantly when running, tensors and massive neutrinos are added to the mix, which shows that the constraint is model independent. In contrast, in an analysis without the Lyα forest and bias σ_8 changes from $\sigma_8 = 0.951^{+0.90}_{-0.079}$ (Table 4.1) to $\sigma_8 = 0.786^{+0.119}_{-0.100}$ (Table 4.3) when massive neutrinos are added as a parameter (see also [39]), so previous constraints were significantly more model dependent.

It is useful to analyze what drives the σ_8 determination. WMAP alone cannot provide a very tight determination, nor can the Lyα forest alone. But combining the two is extremely powerful: from Table 4.1 we see that just these two data sets alone give $\sigma_8 = 0.895^{+0.034}_{-0.032}$ even with running. So this combination in itself provides nearly all of the information on σ_8; galaxy clustering and bias do not constrain this parameter any further when added to the mix. They are however consistent with it: using WMAP and SDSS galaxy clustering with bias and *without* Lyα forest gives $\sigma_8 = 0.89 \pm 0.06$ [47], in remarkable agreement with the analysis of WMAP+SDSS-lya. Assuming that WMAP data are valid this implies that two

	6-p WMAP+gal	6-p WMAP+gal+lya	6-p all	6-p+r WMAP+gal+lya	6-p+r all
$10^2\omega_b$	$2.38^{+0.14\ +0.27\ +0.39}_{-0.12\ -0.23\ -0.33}$	$2.31^{+0.09\ +0.17\ +0.26}_{-0.08\ -0.17\ -0.24}$	$2.33^{+0.09\ +0.17\ +0.26}_{-0.08\ -0.17\ -0.25}$	$2.40^{+0.12\ \ +0.26\ +0.47}_{-0.105\ -0.19\ -0.30}$	$2.40^{+0.11\ +0.23\ +0.33}_{-0.10\ -0.19\ -0.27}$
Ω_m	$0.294^{+0.041\ +0.089\ +0.143}_{-0.034\ -0.061\ -0.082}$	$0.299^{+0.037\ +0.082\ +0.133}_{-0.032\ -0.061\ -0.084}$	$0.281^{+0.023\ +0.046\ +0.070}_{-0.021\ -0.040\ -0.061}$	$0.278^{+0.036\ +0.076\ +0.118}_{-0.033\ -0.062\ -0.094}$	$0.270^{+0.022\ +0.045\ +0.072}_{-0.021\ -0.041\ -0.060}$
n_s	$0.994^{+0.044\ +0.077\ +0.101}_{-0.035\ -0.060\ -0.080}$	$0.971^{+0.023\ +0.048\ +0.070}_{-0.019\ -0.038\ -0.055}$	$0.980^{+0.020\ +0.041\ +0.065}_{-0.019\ -0.037\ -0.051}$	$1.00^{+0.034\ +0.070\ +0.124}_{-0.028\ -0.050\ -0.076}$	$1.00^{+0.027\ +0.056\ +0.085}_{-0.024\ -0.045\ -0.063}$
τ	$0.176^{+0.078\ +0.117\ +0.124}_{-0.071\ -0.124\ -0.161}$	$0.133^{+0.052\ +0.104\ +0.148}_{-0.045\ -0.087\ -0.126}$	$0.160^{+0.040\ +0.079\ +0.117}_{-0.041\ -0.080\ -0.120}$	$0.138^{+0.050\ +0.096\ +0.151}_{-0.045\ -0.085\ -0.118}$	$0.155^{+0.040\ +0.078\ +0.112}_{-0.040\ -0.077\ -0.114}$
σ_8	$0.951^{+0.090\ +0.173\ +0.124}_{-0.079\ -0.142\ -0.161}$	$0.890^{+0.034\ +0.065\ +0.096}_{-0.032\ -0.060\ -0.089}$	$0.897^{+0.033\ +0.065\ +0.097}_{-0.031\ -0.058\ -0.086}$	$0.901^{+0.035\ +0.069\ +0.107}_{-0.033\ -0.062\ -0.096}$	$0.904^{+0.035\ +0.069\ +0.106}_{-0.031\ -0.059\ -0.094}$
h	$0.706^{+0.037\ +0.068\ +0.097}_{-0.034\ -0.065\ -0.091}$	$0.694^{+0.030\ +0.059\ +0.092}_{-0.028\ -0.057\ -0.086}$	$0.710^{+0.021\ +0.044\ +0.066}_{-0.021\ -0.040\ -0.061}$	$0.719^{+0.036\ +0.076\ +0.133}_{-0.032\ -0.061\ -0.091}$	$0.726^{+0.025\ +0.052\ +0.081}_{-0.023\ -0.045\ -0.068}$
r	0	0	0	$< 0.38(0.55)$	$< 0.36(0.51)$

Table 4.1: Constraints on basic 6 parameters and tensors. Median value, 1σ, 2σ and 3σ intervals on cosmological parameters combining WMAP, SDSS galaxies (gal), SDSS bias (bias), SDSS Lyα forest (lya) and SNIa (SN) data as derived from the MCMC analysis. In each case we list individual data sets. Note that WMAP is included in all the chains. In the absence of a detection we give 95% upper limit and (in brackets) 99.9% upper limit. All of the values are obtained from MCMC. The columns compare different theoretical priors and different data sets. The parameters for 6 parameter models 6-p are $\tau, \omega_b, \omega_m, \Omega_m = 1 - \Omega_\lambda, \sigma_8, n_s$.

	6-p+α_s WMAP	6-p+α_s WMAP+gal	6-p+α_s WMAP+lya	6-p+α_s all	6-p+$\alpha_s + r$ WMAP+gal+lya
$10^2\omega_b$	$2.33^{+0.16\ +0.33\ +0.50}_{-0.16\ -0.32\ -0.47}$	$2.30^{+0.14\ +0.29\ +0.45}_{-0.14\ -0.27\ -0.38}$	$2.36^{+0.11\ +0.22\ +0.32}_{-0.10\ -0.19\ -0.27}$	$2.33^{+0.09\ +0.18\ +0.28}_{-0.09\ -0.17\ -0.25}$	$2.42^{+0.12\ +0.24\ +0.39}_{-0.12\ -0.22\ -0.31}$
Ω_m	$0.246^{+0.072\ +0.159\ +0.263}_{-0.057\ -0.103\ -0.140}$	$0.269^{+0.041\ +0.091\ +0.156}_{-0.033\ -0.062\ -0.095}$	$0.257^{+0.055\ +0.105\ +0.151}_{-0.048\ -0.073\ -0.092}$	$0.281^{+0.022\ +0.045\ +0.067}_{-0.021\ -0.043\ -0.062}$	$0.273^{+0.037\ +0.077\ +0.119}_{-0.033\ -0.059\ -0.089}$
n_s	$0.977^{+0.061\ +0.122\ +0.181}_{-0.061\ -0.123\ -0.190}$	$0.959^{+0.052\ +0.104\ +0.164}_{-0.053\ -0.107\ -0.161}$	$0.990^{+0.032\ +0.063\ +0.090}_{-0.029\ -0.053\ -0.076}$	$0.977^{+0.025\ +0.052\ +0.083}_{-0.021\ -0.040\ -0.058}$	$1.00^{+0.034\ +0.070\ +0.102}_{-0.032\ -0.060\ -0.085}$
τ	$0.204^{+0.070\ +0.092\ +0.0957}_{-0.086\ -0.149\ -0.192}$	$0.195^{+0.065\ +0.097\ +0.103}_{-0.068\ -0.123\ -0.165}$	$0.188^{+0.078\ +0.108\ +0.111}_{-0.075\ -0.130\ -0.171}$	$0.163^{+0.041\ +0.083\ +0.123}_{-0.041\ -0.078\ -0.111}$	$0.142^{+0.0493\ +0.0979\ +0.143}_{-0.0465\ -0.0879\ -0.117}$
σ_8	$0.873^{+0.115\ +0.24\ +0.381}_{-0.107\ -0.201\ -0.297}$	$0.897^{+0.059\ +0.108\ +0.189}_{-0.059\ -0.104\ -0.137}$	$0.895^{+0.034\ +0.068\ +0.102}_{-0.032\ -0.064\ -0.094}$	$0.899^{+0.034\ +0.070\ +0.107}_{-0.030\ -0.058\ -0.085}$	$0.900^{+0.034\ +0.069\ +0.100}_{-0.032\ -0.063\ -0.094}$
h	$0.736^{+0.061\ +0.127\ +0.204}_{-0.054\ -0.103\ -0.146}$	$0.716^{+0.039\ +0.079\ +0.135}_{-0.040\ -0.080\ -0.121}$	$0.730^{+0.053\ +0.092\ +0.128}_{-0.046\ -0.080\ -0.107}$	$0.709^{+0.022\ +0.046\ +0.072}_{-0.021\ -0.040\ -0.059}$	$0.725^{+0.037\ +0.074\ +0.123}_{-0.035\ -0.066\ -0.094}$
r	0	0	0	0	$< 0.45(0.64)$
$10^2\alpha_s$	$-1.24^{+3.75\ +7.63\ +11.8}_{-3.63\ -7.23\ -11.1}$	$-2.41^{+3.07\ +6.24\ +9.45}_{-3.10\ -6.14\ -9.20}$	$-0.263^{+1.27\ +2.66\ +4.15}_{-1.13\ -2.21\ -3.22}$	$-0.29^{+1.08\ +2.35\ +3.63}_{-1.00\ -1.84\ -2.61}$	$-0.57^{+1.21\ +2.49\ +3.48}_{-1.14\ -2.26\ -3.39}$

Table 4.2: Constraints on running. Same format as for Table 4.1.

	6-p+3 × m_ν WMAP+gal	6-p+3 × m_ν WMAP+gal+lya	6-p+3 × m_ν all	6-p+3 × $m_\nu + \alpha_s + r$ all	6-p+1×m_ν all
$10^2\omega_b$	$2.41^{+0.16\ +0.31\ +0.46}_{-0.14\ -0.25\ -0.37}$	$2.34^{+0.08\ +0.17\ +0.25}_{-0.08\ -0.17\ -0.25}$	$2.36^{+0.09\ +0.19\ +0.32}_{-0.09\ -0.18\ -0.29}$	$2.47^{+0.13\ +0.26\ +0.38}_{-0.12\ -0.22\ -0.32}$	$2.35^{+0.12\ +0.25\ +0.36}_{-0.10\ -0.19\ -0.28}$
Ω_m	$0.352^{+0.131\ +0.241\ +0.334}_{-0.080\ -0.120\ -0.149}$	$0.316^{+0.029\ +0.067\ +0.124}_{-0.027\ -0.052\ -0.080}$	$0.284^{+0.025\ +0.05\ +0.079}_{-0.023\ -0.044\ -0.060}$	$0.277^{+0.025\ +0.051\ +0.086}_{-0.023\ -0.045\ -0.064}$	$0.287^{+0.028\ +0.060\ +0.103}_{-0.025\ -0.048\ -0.069}$
n_s	$1.00^{+0.051\ +0.098\ +0.131}_{-0.041\ -0.071\ -0.095}$	$0.978^{+0.023\ +0.051\ +0.069}_{-0.020\ -0.039\ -0.055}$	$0.989^{+0.026\ +0.053\ +0.076}_{-0.023\ -0.042\ -0.060}$	$1.020^{+0.033\ +0.066\ +0.094}_{-0.033\ -0.061\ -0.082}$	$1.00^{+0.032\ +0.061\ +0.083}_{-0.025\ -0.047\ -0.067}$
τ	$0.133^{+0.081\ +0.144\ +0.165}_{-0.060\ -0.101\ -0.128}$	$0.153^{+0.055\ +0.107\ +0.140}_{-0.042\ -0.075\ -0.101}$	$0.185^{+0.052\ +0.099\ +0.114}_{-0.046\ -0.089\ -0.125}$	$0.206^{+0.059\ +0.088\ +0.093}_{-0.058\ -0.105\ -0.143}$	$0.195^{+0.059\ +0.096\ +0.104}_{-0.055\ -0.102\ -0.147}$
σ_8	$0.786^{+0.119\ +0.230\ +0.301}_{-0.100\ -0.172\ -0.230}$	$0.873^{+0.035\ +0.066\ +0.099}_{-0.032\ -0.065\ -0.093}$	$0.890^{+0.035\ +0.071\ +0.098}_{-0.033\ -0.064\ -0.092}$	$0.882^{+0.032\ +0.069\ +0.107}_{-0.030\ -0.057\ -0.087}$	$0.895^{+0.035\ +0.067\ +0.10}_{-0.033\ -0.063\ -0.094}$
h	$0.663^{+0.070\ +0.117\ +0.164}_{-0.076\ -0.113\ -0.146}$	$0.684^{+0.023\ +0.047\ +0.070}_{-0.022\ -0.047\ -0.083}$	$0.710^{+0.023\ +0.047\ +0.075}_{-0.022\ -0.044\ -0.067}$	$0.723^{+0.027\ +0.054\ +0.082}_{-0.025\ -0.047\ -0.080}$	$0.744^{+0.024\ +0.050\ +0.078}_{-0.023\ -0.047\ -0.072}$
r	0	0	0	$< 0.47(0.63)$	0
$10^2\alpha_s$	0	0	0	$-0.18^{+1.23\ +2.46\ +3.78}_{-1.24\ -2.50\ -3.62}$	0
$\sum m_\nu$	1.54 (2.26) eV	0.54 (0.86) eV	0.42 (0.67) eV	0.66 (0.93) eV	0.84(1.61) eV

Table 4.3: Neutrino mass constraints. Same format as for Table 4.1. All except last column are for the case of 3 degenerate neutrino families. Last column is for 3 massless + 1 massive neutrino family.

	6-p+w WMAP+gal+SN	6-p+w all	6-p+w WMAP+gal+bias+lya	6-p+w+$\alpha_s + r$ WMAP+gal+bias+lya	6-p+$w_0 + w_1$ all
$10^2\omega_b$	$2.36^{+0.13\ +0.26\ +0.38}_{-0.11\ -0.21\ -0.31}$	$2.33^{+0.10\ +0.20\ +0.32}_{-0.09\ -0.18\ -0.27}$	$2.34^{+0.09\ +0.19\ +0.28}_{-0.09\ -0.16\ -0.25}$	$2.48^{+0.15\ +0.29\ +0.43}_{-0.13\ -0.24\ -0.34}$	$2.33^{+0.10\ +0.20\ +0.32}_{-0.09\ -0.17\ -0.25}$
Ω_m	$0.303^{+0.029\ +0.061\ +0.093}_{-0.028\ -0.052\ -0.072}$	$0.282^{+0.023\ +0.047\ +0.074}_{-0.023\ -0.044\ -0.067}$	$0.264^{+0.028\ +0.056\ +0.109}_{-0.025\ -0.046\ -0.062}$	$0.260^{+0.024\ +0.050\ +0.077}_{-0.022\ -0.040\ -0.056}$	$0.285^{+0.024\ +0.047\ +0.070}_{-0.023\ -0.045\ -0.066}$
n_s	$0.987^{+0.041\ +0.077\ +0.105}_{-0.030\ -0.054\ -0.075}$	$0.981^{+0.027\ +0.055\ +0.080}_{-0.023\ -0.042\ -0.062}$	$0.980^{+0.026\ +0.051\ +0.068}_{-0.020\ -0.038\ -0.059}$	$1.020^{+0.041\ +0.080\ +0.114}_{-0.037\ -0.068\ -0.096}$	$0.978^{+0.028\ +0.058\ +0.084}_{-0.022\ -0.041\ -0.059}$
τ	$0.160^{+0.082\ +0.130\ +0.139}_{-0.067\ -0.116\ -0.153}$	$0.163^{+0.064\ +0.121\ +0.135}_{-0.057\ -0.103\ -0.146}$	$0.145^{+0.066\ +0.125\ +0.152}_{-0.056\ -0.109\ -0.142}$	$0.201^{+0.057\ +0.091\ +0.098}_{-0.063\ -0.117\ -0.163}$	$0.152^{+0.067\ +0.127\ +0.146}_{-0.056\ -0.101\ -0.136}$
σ_8	$0.945^{+0.089\ +0.187\ +0.290}_{-0.080\ -0.150\ -0.212}$	$0.895^{+0.033\ +0.067\ +0.104}_{-0.031\ -0.059\ -0.089}$	$0.920^{+0.040\ +0.084\ +0.12}_{-0.041\ -0.072\ -0.093}$	$0.890^{+0.030\ +0.063\ +0.099}_{-0.028\ -0.056\ -0.089}$	$0.897^{+0.033\ +0.068\ +0.104}_{-0.031\ -0.059\ -0.088}$
h	$0.699^{+0.027\ +0.054\ +0.080}_{-0.026\ -0.050\ -0.073}$	$0.708^{+0.023\ +0.046\ +0.069}_{-0.022\ -0.044\ -0.064}$	$0.736^{+0.039\ +0.080\ +0.119}_{-0.038\ -0.069\ -0.112}$	$0.726^{+0.025\ +0.050\ +0.078}_{-0.024\ -0.048\ -0.072}$	$0.707^{+0.024\ +0.049\ +0.074}_{-0.023\ -0.046\ -0.066}$
r	0	0	0	$< 0.51(0.67)$	0
$10^2\alpha_s$	0	0	0	$-1.07^{+1.24\ +2.64\ +4.15}_{-1.16\ -2.26\ -3.31}$	0
w	$-1.009^{+0.096\ +0.18\ +0.26}_{-0.112\ -0.24\ -0.38}$	$-0.990^{+0.086\ +0.16\ +0.22}_{-0.093\ -0.20\ -0.35}$	$-1.080^{+0.149\ +0.24\ +0.31}_{-0.193\ -0.37\ -0.54}$	$-0.908^{+0.077\ +0.14\ +0.19}_{-0.091\ -0.19\ -0.32}$	$-0.981^{+0.193\ +0.38\ +0.57}_{-0.193\ -0.37\ -0.52}$
w_1	0	0	0	0	$0.05^{+0.83\ +1.92\ +2.88}_{-0.65\ -1.13\ -1.38}$

Table 4.4: Dark energy constraints. Same format as for Table 4.1. All columns except last one assume constant equation of state w. Last column gives constraints for the case where dark energy is time dependent as $w = w_0 + w_1(1 - a)$.

independent analyses of different data, SDSS-gal+bias and SDSS-lya, lead to essentially the same value. Both improve upon previous constraints, by a factor of 1.5-2 for WMAP+SDSS-gal+bias and a factor of 3-4 for WMAP+SDSS-lya. These new constraints remove almost all of the degeneracy between σ_8 and optical depth τ (figure 4.1).

There are many recent determinations of σ_8 in the literature, which vary between 0.6 and 1.1. Recent discussion of some of these methods and results, such as weak lensing, cluster abundance, galaxy bias determination, and SZ power spectrum can be found in [39, 47]. The value found here is in good agreement with most of these constraints: it is on the low end of the SZ constraints and on the upper end of some of the cluster abundance constraints. It is also in good agreement with the 2dF bias constraints and with several weak lensing constraints.

While in the tables we do not present results for the amplitude of metric (described here with curvature fluctuation $\mathcal{R}$) fluctuations at the pivot point we find it is also tightly constrained to

$$\Delta^2_{\mathcal{R}}(k_{\rm pivot} = 0.05/{\rm Mpc}) = (2.45 \pm 0.23) \times 10^{-9}. \tag{4.3}$$

4.3.2 Optical depth

The optical depth due to reionization is a parameter that has a strong effect on the CMB. It suppresses the CMB on small scales and thus leads to a strong degeneracy with amplitude. This degeneracy can be lifted by the polarization observations [106], but for WMAP 1st year these are noisy and may contain significant contamination from foregrounds. The current analysis based on 1st year data is rather unsatisfactory, since it is based on the existing temperature-polarization cross-correlation analysis, which on large scales may suffer from similar problems as the temperature auto-correlation analysis [4]. The upcoming 2nd year data release of WMAP should provide polarization maps and the corresponding analysis may help improve the situation. Until then we will use the current WMAP provided likelihood code [21], but this should be taken as preliminary and the constraints on optical depth from polarization, both the best fitted value and the associated errors, may change.

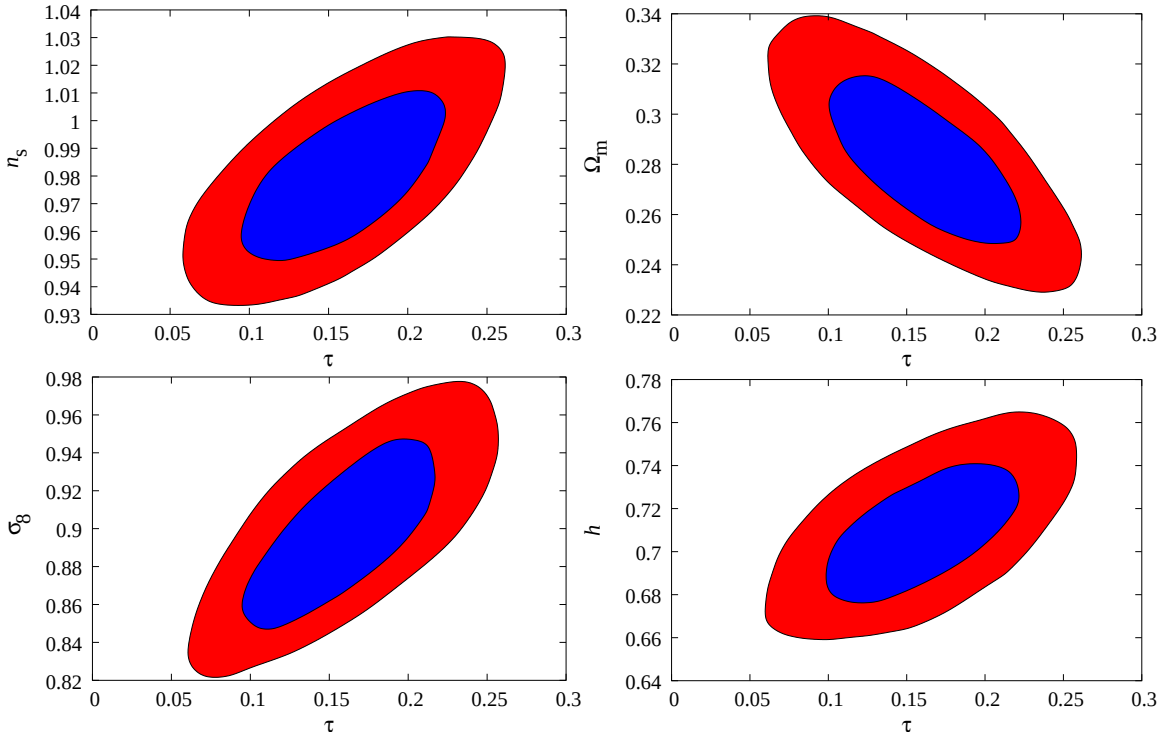

Figure 4.1: 68% (inner, blue) and 95% (outer, red) contours in the plane of τ versus Ω_m, h, σ_8 and n_s, respectively, using all measurements.

With the addition of new constraints from the Lyα forest and SDSS bias there remain correlations between optical depth τ and several other parameters from 6-parameter analysis on all data in Table 4.1. Results are shown in figure 4.1. The degeneracies are significantly less severe than before, since the parameters are better determined with the new data. Still, there is room to improve the constraints with a better determination of the optical depth. For example, if the optical depth ends up being at the lower end of its allowed range this would lead to a decrease in the best fitted value of n_s, h and σ_8 and to an increase in the best fitted value of Ω_m. Note that the values of τ do not extend up to the cutoff value $\tau = 0.3$ for the 95% contours, so these distributions are not affected by the choice of the prior $\tau < 0.3$. However, in chains with more parameters, such as dark energy equation of state w, this is no longer the case. At the moment the only argument for adopting this prior is that if $\tau > 0.3$ this would possibly have led to detectable auto-correlation of polarization in the WMAP data, but this argument is inconclusive since the polarization maps are not available and such analysis has not been published yet. In the absence of any published results we follow the WMAP team approach and adopt $\tau < 0.3$.

4.3.3 Neutrino mass

Both the CMB and LSS are important as tracers of neutrino mass. At the time of decoupling, neutrinos are still relativistic, but become nonrelativistic later in the evolution of the universe if their mass is sufficiently high. Neutrinos free-stream out of their potential wells, erasing their own perturbations on smaller scales. Below this suppression scale the power spectrum shape is the same as in regular CDM models, so on small scales the only consequence is the suppression of the amplitude relative to large scales. In the matter power spectrum neutrinos leave a characteristic feature at the transition scale. The actual shape of the transition depends on the individual masses of neutrinos and not just on their sum. For masses of interest today the transition is occurring around $k = 0.1h/\mathrm{Mpc}$, which are the scales measured by SDSS-gal. Neutrinos with mass below 2eV are still relativistic when they enter the horizon for scales around $k = 0.1h/\mathrm{Mpc}$ and are either relativistic or

quasi-relativistic at the time of recombination, $z \sim 1100$. As a result neutrinos cannot be treated as a nonrelativistic component with regard to the CMB and are not completely degenerate with the other relativistic components in the CMB.

From the joint analysis we find for the sum of all masses (Table 4.3)

$$\sum m_\nu < 0.42\text{eV } (0.67\text{eV}) \text{ (3 families)}, \tag{4.4}$$

at 95% (99.9%) c.l. for a single component and assuming no running, as was done in all of the work to date. Our constraints improve upon WMAP+SDSS-gal, where we find $m_\nu < 1.54$eV and upon WMAP+2dF constraints, where $m_\nu < 0.69$eV was found by combining WMAP and 2dF with the bias determination from the bispectrum analysis [98].

If running and tensors are allowed, the parameter space expands. In this case, we find $m_\nu < 0.66$ (0.93)eV. Much of this is caused by running: as discussed in [47] running and neutrino mass are anti-correlated. Negative runnings as large as -0.04 and neutrino masses as high as 1.5eV are allowed at 2-sigma. Running is poorly motivated by inflationary models and there is no evidence for it in the current data, so adopting the inflationary prior with no running is reasonable, but one should be aware that the limits are model dependent.

The constraint from equation (4.4) is remarkably tight and implies the upper limit on neutrino mass assuming degeneracy is 0.14eV at 95% c.l. Our constraint has been obtained assuming 3 degenerate mass neutrino families, but if the neutrino mass splittings are small the constraints on the sum are almost the same even if individual masses are not identical. If the masses are very large compared to mass splittings then the neutrino masses are close to degenerate. However, our upper limit is so low that including mass splittings is necessary. Super-Kamionkande (SK) results find neutrino mass squared difference $\delta m_{23} = 2.5 \times 10^{-3}\text{eV}^2$ [91, 92], while solar neutrino constraints find neutrino mass squared difference $\delta m_{12} = 8 \times 10^{-5}\text{eV}^2$ [107, 93]. This gives one neutrino family with minimum mass around 0.05eV and another with minimum mass close to 0.007eV. Since only the mass difference is measured, it is in principle possible that the actual neutrino masses are larger than that. Our constraints in combination with SK and solar neutrino constraints limit the mass of

the neutrino families to

$$m_1 < 0.13\text{eV}, \quad m_2 < 0.13\text{eV}, \quad m_3 < 0.14\text{eV}, \tag{4.5}$$

all at 95% c.l. These limits essentially exclude the range of masses argued by the Heidelberg-Moscow experiment of neutrinoless double beta decay if neutrinos are Majorana particles [108], although the two results may still be compatible given all the uncertainties in nuclear matrix element calculations. From $\Delta m/m \sim \Delta m^2/2m$ with $m \sim 0.13$eV we find the neutrino masses are not degenerate, but the limits are still weak: the ratios must satisfy

$$\frac{m_3}{m_1} > 1.1, \quad 1.1 < \frac{m_3}{m_2} < 7, \tag{4.6}$$

where the upper limit on m_3/m_2 is determined solely from SK and solar neutrino constraints.

The mass limits presented above are based on 3 degenerate massive neutrino families. If one assumes a model with 3 massless families and 1 massive family (such as a sterile neutrino model), as motivated by LSND results [95], then the mass limits on the sum change, since both the CMB and the matter power spectrum change (see figure 6 in [47]). These limits are improved as well with the addition of SDSS-lya and SDSS-bias. We find

$$m_\nu < 0.79\text{eV } (1.55\text{eV}) \ (3+1 \text{ families}), \tag{4.7}$$

at 95 % (99.9%), compared to the WMAP+2dF analysis without bias where the 95% confidence limit is 1.4eV [96] and to the SDSS+WMAP analysis where the limit is 1.37eV [47]. We have subtracted from the total sum in Table 4.3 the masses of the active neutrinos to obtain the limit in equation (4.7). These limits are improved by almost a factor of 2 compared to previous analyses. These limits are more model independent, as there is little correlation with running and/or tensors in this model: for the chains with running and tensors we find $m_\nu < 0.88$eV (1.40eV) at 95% (99.9%) c.l.

From the LSND experiment the allowed regions are four islands with the lowest mass $m_\nu = 0.9$eV and the next lowest 1.4eV [109, 95, 96, 110]. Thus the lowest island allowed by LSND results is excluded at 95% c.l. and all the others at 99.9%. Our derived limits will be tested directly with MiniBoone Experiment at Fermilab [111].

4.3.4 Tensors

Gravity waves (tensors) are predicted in many models of inflation. The simplest single field models of inflation predict a tight relation between tensor amplitude and slope, which we assume here. We choose to parametrize them at the pivot point $k = 0.05$/Mpc, just as for the amplitude, slope and running. This pivot differs from that in the WMAP analysis [23]. While tensors have their largest effect on large scales, within the single field model adopted here the slope is assumed to be determined from the tensor amplitude. Thus there is no need to parametrize tensors on large scales.

For 7-parameter model without running or neutrino mass, the limit on tensors is (Table 4.1)

$$T/S < 0.36(0.51) \tag{4.8}$$

at 95% (99.9%) c.l. This does not change significantly if neutrinos or running are added to the mix (Tables 4.2–4.3), in the latter case we find $r < 0.45(0.64)$. This constraint is nearly a factor of two better than from WMAP analysis, a consequence of tighter constraint on running from the Lyα forest. We return to these constraints below where we discuss inflation.

4.3.5 Spectral index

Constraints on the scalar spectral index are primarily driven by the WMAP and SDSS-lya combination. Using these two experiments alone one finds $n_s = 0.990^{+0.032}_{-0.029}$ for the chains with running, compared to $n_s = 0.962^{+0.054}_{-0.056}$ for WMAP+SDSS-gal+SDSS-bias without SDSS-lya and to $n_s = 0.975^{+0.028}_{-0.024}$ for the case where all observations are included (Table 4.2). The inclusion of the SDSS Lyα forest thus reduces the error on the primordial slope by a factor of 2. In the absence of running and with bias and SNIa, this constraint improves further to

$$n_s = 0.981^{+0.019\ +0.040\ +0.061}_{-0.018\ -0.037\ -0.053}. \tag{4.9}$$

Note that the scale invariant model $n_s = 1$ is only 1-sigma away from the best fit. It is remarkable that such a vast range of observational constraints can be reproduced with a

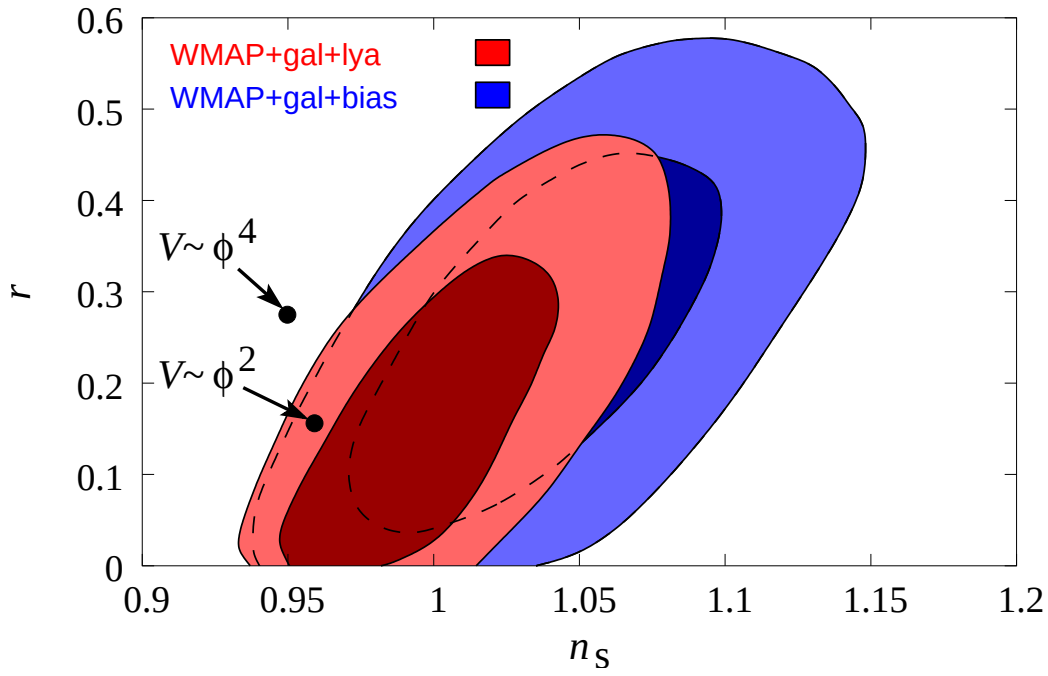

Figure 4.2: 68% (inner, dark) and 95% (outer, light) contours in the $(r = T/S, n_s)$ plane with and without SDSS-lya. There is a correlation between tensors and slope n_s. Inclusion of the Lyα forest significantly reduces the allowed region in this plane. Also shown are the positions of two chaotic inflation models, $V \propto \phi^2$ with $N = 50$ and $V \propto \phi^4$ with $N = 60$.

scale invariant power spectrum with 4 parameters only, Ω_b, Ω_m, h and amplitude $\Delta^2_{\mathcal{R}}$ (plus possibly optical depth τ to explain the polarization data).

Tensors are positively correlated with the slope (Figure 4.2) and their inclusion increases the best fit slope value to $n_s = 1.00^{+0.034}_{-0.028}$. All of these are consistent with a scale invariant spectrum and are in a good agreement with the WMAPext+2dF constraint $n_s = 0.97 \pm 0.03$ [2]. While 2dF gives a slightly redder spectrum than SDSS the differences in different values quoted in the literature reflect mostly the differences in the assumed parameter space, as shown here for the example of tensors.

4.3.6 Running of the spectral index

The issue of the running of the primordial slope has generated a lot of interest lately. WMAP argued for some weak evidence for negative running in their combined analysis, but some of that evidence was based on Lyman alpha constraints by previous workers [86, 112], which

were shown to underestimate the errors [3]. It was argued that even from WMAP alone, or WMAP+2dF, there is some evidence for running, and the WMAP+SDSS-gal analysis without bias information gave $\alpha_s = -0.071 \pm 0.044$ [39]. Similar values have been found from the recent analyses including CBI [101] and VSA [102] data. However, much of this effect comes from low l multipoles and a full likelihood analysis of WMAP+SDSS-gal changes this value to -0.022 ± 0.033 [4]. Including the biasing constraints does not really change this result. In the absence of massive neutrinos and tensors we find $\alpha_s = -0.022^{+0.030}_{-0.032}$, so $\alpha_s = 0$ is within one sigma of 0 and the error has not been reduced.

Including SDSS-lya reduces the errors dramatically. The constraint on running from WMAP+SDSS-lya alone is $\alpha_s = -0.0026^{+0.013}_{-0.011}$. Including everything this changes slightly to

$$\alpha_s = -0.0029^{+0.011\ +0.023\ +0.036}_{-0.010\ -0.018\ -0.026}, \tag{4.10}$$

which is a factor of 3 improvement over previous constraints. Even with this significant improvement we find no hint of running in the joint analysis. The result is in perfect agreement with no running and 95% of chain elements have $\alpha_s > -0.015$. This should be compared to values as low as $\alpha_s \sim -0.10$ in figure 4.3. Similarly low values have been found in recent analyses [101, 102]. Figure 4.3 shows old and new constraints in the (α_s, n_s) plane, highlighting the dramatic reduction of available parameter space when CMB and Lyα forest data are combined together. The implications of this result for inflation are discussed in the next section.

If tensors are also included they induce weak anti-correlation with running, so the best fit value becomes $\alpha_s = -0.006^{+0.012}_{-0.011}$, which is still perfectly consistent with no running. This is shown in figure 4.4, where we see that adding SDSS-lya to the mix dramatically reduces the allowed region of parameter space. Specifically, without SDSS-lya, runnings as negative as -0.15 are in the 95% confidence region, a consequence of strong correlation between running and tensors. Our joint analysis eliminates these large negative running solutions. We find no evidence for running in the current data, with or without tensors, despite a factor of 3 reduction in the errors.

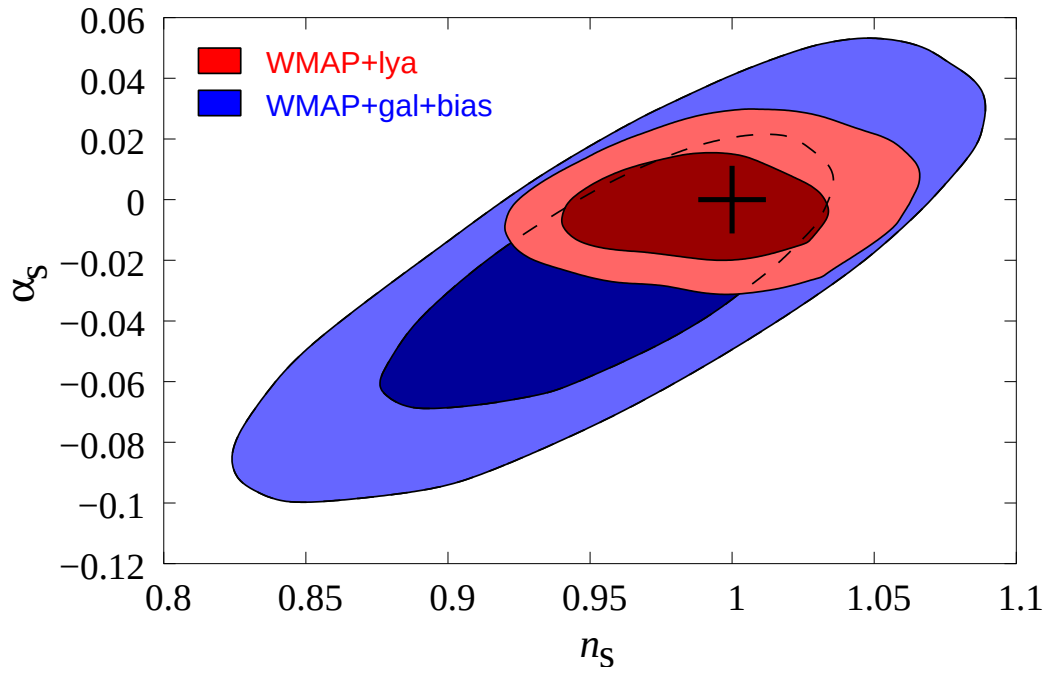

Figure 4.3: 68% (inner, dark) and 95% (outer, light) contours in the (α_s, n_s) plane using WMAP+SDSS-lya versus WMAP+SDSS-gal+bias. Adding the SDSS Lyα forest dramatically reduces the allowed region of parameter space in this plane. Note that the simplest model with $n_s = 1$ and $\alpha_s = 0$ is within 68% interval.

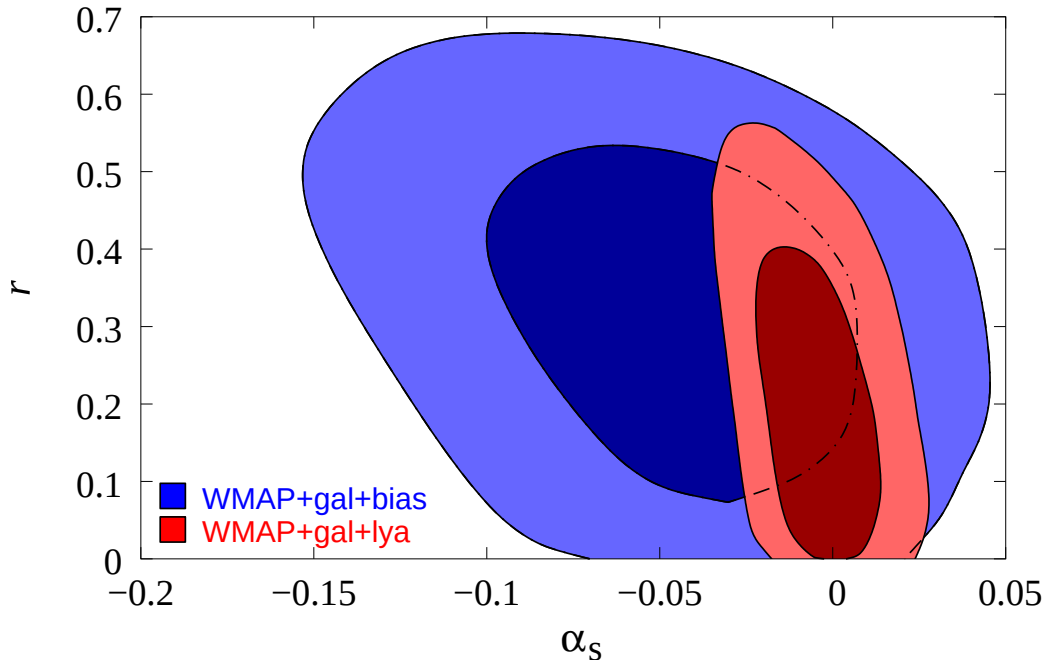

Figure 4.4: 68% (inner, dark) and 95% (outer, light) contours in the (α_s, r) plane using WMAP+SDSS-lya versus WMAP+SDSS-gal+bias. Adding the SDSS Lyα forest dramatically reduces the allowed region of parameter space in this plane. Note that the simplest model with $\alpha_s = 0$ and $r = 0$ is within the 68% interval.

Running is correlated with some of the "nuisance" parameters we marginalize over in the analysis and additional observations constraining these could lead to a further reduction of errors on the primordial slope and its running even with no additional improvements in the observations. For example, in our current treatment of the filtering parameter k_F (a generalization of the Jeans length), we assume that the minimum reionization redshift is around 10 with a reheating temperature of 25,000K. If we change the redshift to 7, this leads to an increase in the maximum value of k_F allowed. In this case we find for WMAP+SDSS-lya analysis the running changes from $\alpha_s = 0.0017$ to -0.0045, with an error around 0.01 (see Table 4.2). If we change this redshift to 4, below its theoretically allowed lower limit of 6.5, to allow for any residual resolution issues in numerical simulations, we find $\alpha_s = -0.009$ with comparable errors. All the other parameters change much less. While these changes are small and do not qualitatively change our conclusions, they may be important for the future analyses where smaller errors may be obtained. In all these cases the data prefer a high value of k_F, i.e. a late epoch of reionization. Independent constraints on the tempetarure evolution of IGM would be helpful to constrain this further.

4.3.7 Matter density and Hubble parameter

The matter density parameter Ω_m has contributions from cold dark matter, baryons, and neutrinos. We assume spatially flat universe, so matter density Ω_m is related to dark energy density $\Omega_m = 1 - \Omega_\lambda$. As emphasized in [113], the matter density is still allowed to cover a wide range of values from the present data: in 7-parameter models with running WMAP+SDSS-gal gives $\Omega_m = 0.269^{+0.041}_{-0.033}$. WMAP+SDSS-lya gives a slightly lower value with comparable error, $\Omega_m = 0.257^{+0.055}_{-0.048}$ in models with running. Combining WMAP, SDSS-gal and SDSS-lya gives $\Omega_m = 0.299^{+0.037}_{-0.032}$. Including the bias and SNIa and ignoring running brings the value to

$$0.282^{+0.021\ +0.043\ +0.066}_{-0.020\ -0.043\ -0.067} \tag{4.11}$$

which is a factor of 2 improvement over previous constraints. The matter density is correlated with r and inclusion of tensors in the parameter space slightly reduces the density

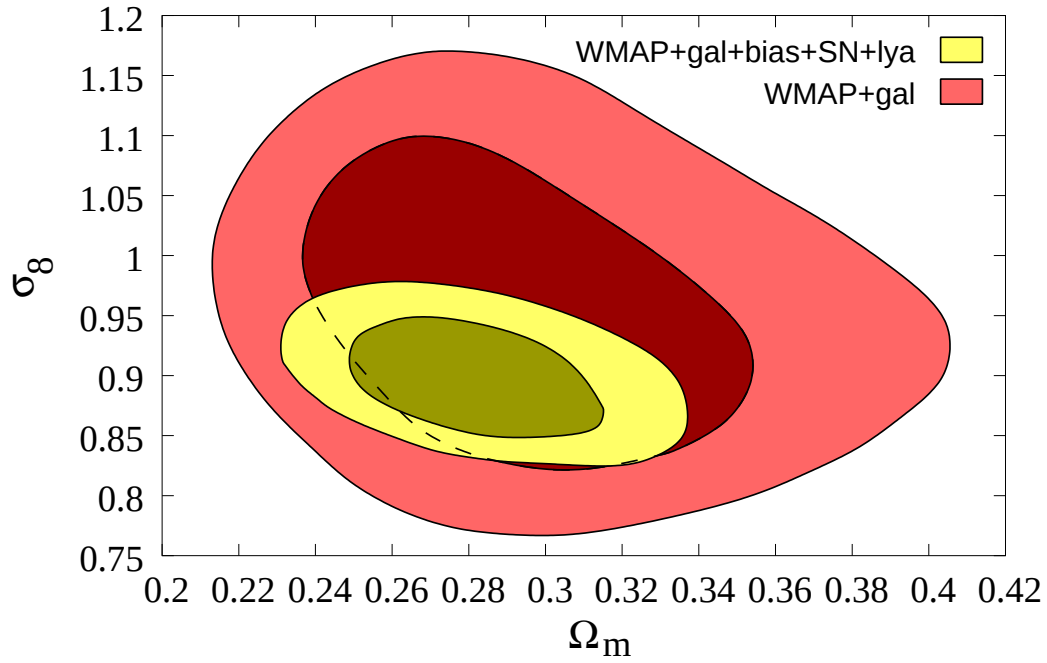

Figure 4.5: 68% and 95% contours in the (Ω_m, σ_8) plane showing previous constraints from WMAP and galaxy clustering with the new data.

parameter. There is a significant improvement in (σ_8, Ω_m) plane with the addition of new data (figure 4.5).

Despite the improvements the matter density remains strongly correlated with the Hubble parameter h, as expected from the fact that $\Omega_m h^2$ is better determined from the CMB than each parameter separately. This is shown in figure 4.6 for 6-parameter models for the analysis with and without inclusion of SDSS-lya.

For the Hubble parameter the best fit value and its error is $h = 0.71 \pm 0.02$ in 6-parameter space. In 9-parameter space with tensors, massive neutrinos and running we find $h = 0.74 \pm 0.05$. All of these fits are statistically acceptable and are in good agreement with the HST key project value $h = 0.72 \pm 0.08$ [114], although a different group using almost the same data continues to find a significantly lower value $h = 0.58 \pm 0.06$ [115].

The new data also improve significantly the age of the universe constraint. We find $t_0 = 13.6^{+0.19}_{-0.19}$Gyr, compared to $14.1^{+1.0}_{-0.9}$Gyr found from the WMAP+SDSS-gal analysis [39].

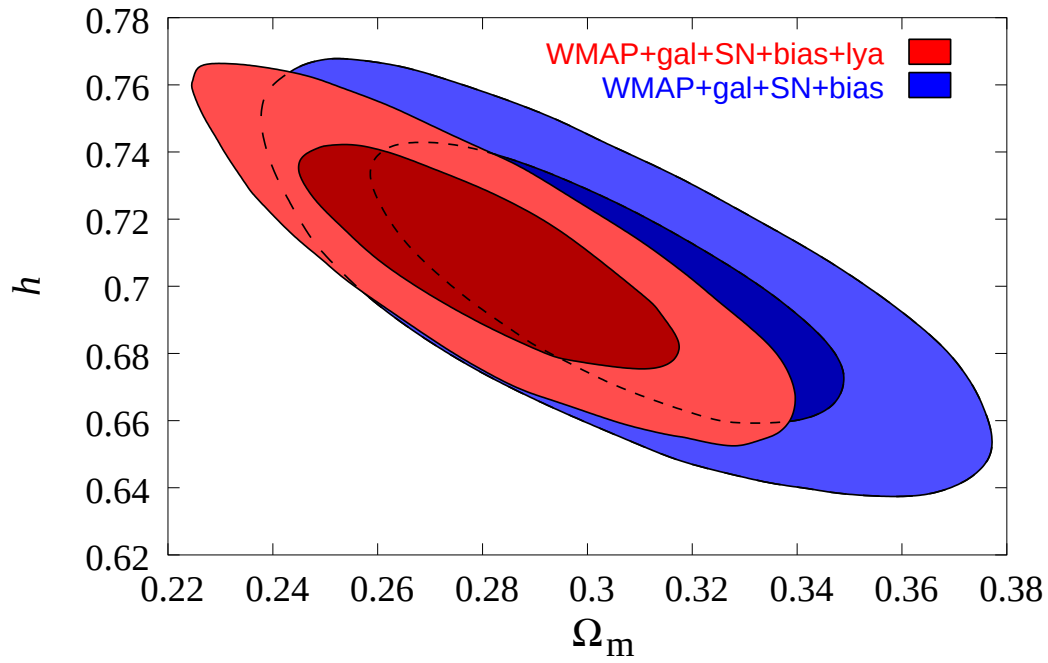

Figure 4.6: 68% (inner, dark) and 95% (outer, light) contours in the (Ω_m, h) plane with and without SDSS-lya. There is a strong correlation between the two parameters because WMAP constrains best the combination $\Omega_m h^2$.

4.3.8 Dark energy

So far we have assumed dark energy in the form of a cosmological constant, $w = -1$. We now relax this assumption and explore the constraints on w. To maximize the constraints we add to some of the analyses the "gold" SNIa data [77]. Because we do not want to limit ourselves to $w > -1$ we assume dark energy does not cluster (ndyn = 3 option in CMBFAST4.5). Note that clustering of dark energy vanishes for w=-1 and so if w is close to -1 then it makes very little difference if clustering is included or not. Figure 4.7 shows the constraints in the (w, Ω_m) plane. We find

$$w = -0.990^{+0.086\ +0.16\ +0.222}_{-0.093\ -0.201\ -0.351}. \tag{4.12}$$

We see that $w = -1$ is an acceptable solution. This should be compared to $w = -1.01^{+0.097}_{-0.12}$ we find in the absence of bias and Lyα forest constraint, to $w = -0.91^{+0.13}_{-0.15}$ using the new SNIa data but just some of the LSS constraints [116], to $w = -1.02^{+0.13}_{-0.19}$ using a simple Ω_m prior [77], and to $w = -0.98^{+0.12}_{-0.12}$ from the WMAP 1st year analysis [2]. It is worth

emphasizing the agreement and complementarity of the LSS, CMB, and SNIa constraints: in the absence of SNIa data the constraint is $w = -1.02^{+0.15}_{-0.19}$ and w is positively correlated with Ω_m (figure 4.7). These solutions allow phantom energy models ($w < -1$) with w as low as -1.5 for low matter density values. On the other hand the two are anticorrelated for the WMAP+SDSS-gal+SNIa data constraints, and phantom energy solutions are allowed for high values of the matter density. Combing the two sets of constraints significantly reduces the parameter space of allowed solutions. All of these different combinations give very consistent results and the median value hardly changes at all and is in all cases very close to $w = -1$. Our constraints are a factor of 1.5-2 better than previously published constraints on the dark energy equation of state. Some of the improvement comes from our more sophisticated analysis which includes all of the information previously available and some from the new constraints from the bias and Lyα forest, which further reduce the errors. This is an example of how combining different data sets leads not only to a significant improvement in the accuracy of cosmological parameters, but also how consistency among the different methods gives confidence in the resulting constraints.

The results are weakly model dependent, in the sense that they are sensitive to the parameter space over which one is projecting. If we include tensors and running in the analysis we find

$$w = -0.908^{+0.077\ +0.143\ +0.192}_{-0.091\ -0.197\ -0.324}\ , \tag{4.13}$$

roughly a 1-sigma change in the central value compared to the case without tensors in equation (4.12). Figure 4.8 shows that tensors and the equation of state are correlated. The shift in the best fitted value of w reflects a large volume of parameter space associated with $r > 0$ models and not any fit improvement when adding tensors and running: χ^2 changes only by 1 and there is no need to introduce tensors (or $w \neq -1$) to improve the fit to the data. We also find no correlation between the equation of state and running.

Our constraints eliminate a significant fraction of previously allowed parameter space, with 95% contours at $-1.19 < w < -0.83$ without tensors and at $-1.11 < w < -0.77$ with tensors. Thus a large fraction of the parameter space of "phantom energy" models with

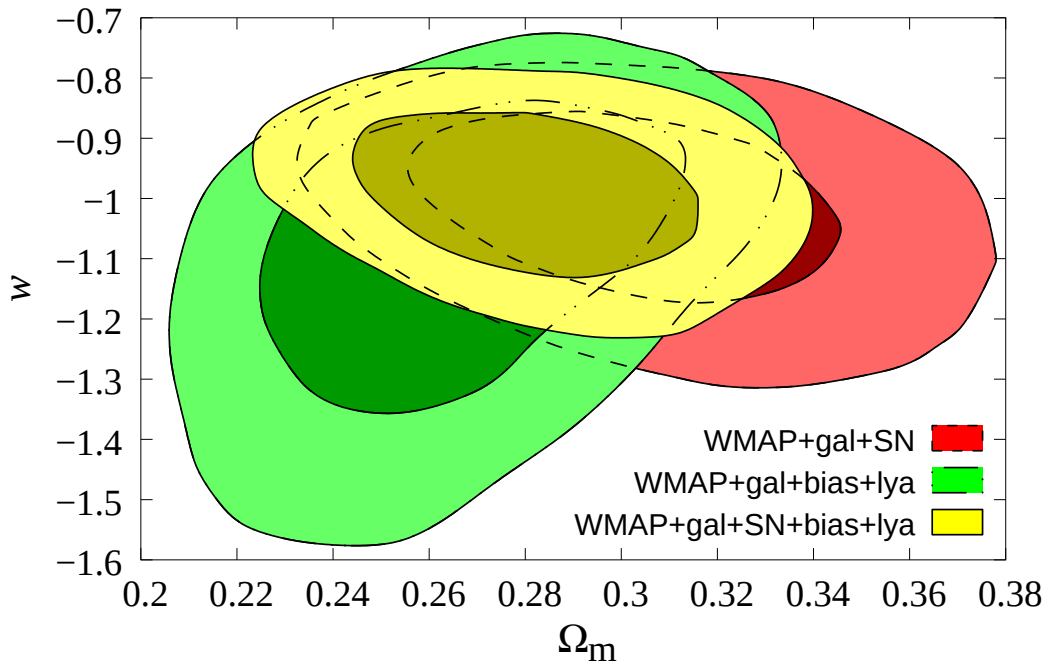

Figure 4.7: 68% and 95% contours in the (Ω_m, w) plane showing previous constraints without SDSS-lya and bias, constraints without SNIa, and combined constraints. In all cases the data are consistent with a cosmological constant model ($w = -1$).

$w < -1$ [117] and tracker quintessence models with $w \sim -0.7$ [118] appears to be excluded. Other dark energy models which predict $w \sim -1$ remain acceptable. It is interesting to note that simplest quintessence solutions with $w > -1$ are more acceptable if tensors are present at a level predicted by some inflationary models ($r \sim 0.2$).

We also ran a MCMC simulation exploring a non-constant equation of state. We use a second order expansion

$$w = w_0 + (a-1)w_1 + (a-1)^2 w_2, \tag{4.14}$$

where $a = 1/(1+z)$ is the expansion factor [119]. The advantage of this expansion is that it is well behaved throughout the history of the universe from early times, when $a \sim 0$, to today ($a = 1$). This is in contrast to the often adopted expansion in terms of the redshift, $w = w_0 + w'z$, which diverges at high redshift and so can give artificially tight constraints on w' if CMB (or even BBN) constraints at high redshift are used, without actually saying much about the time dependence of w in the relevant regime $0 < z < 1$. In contrast, using

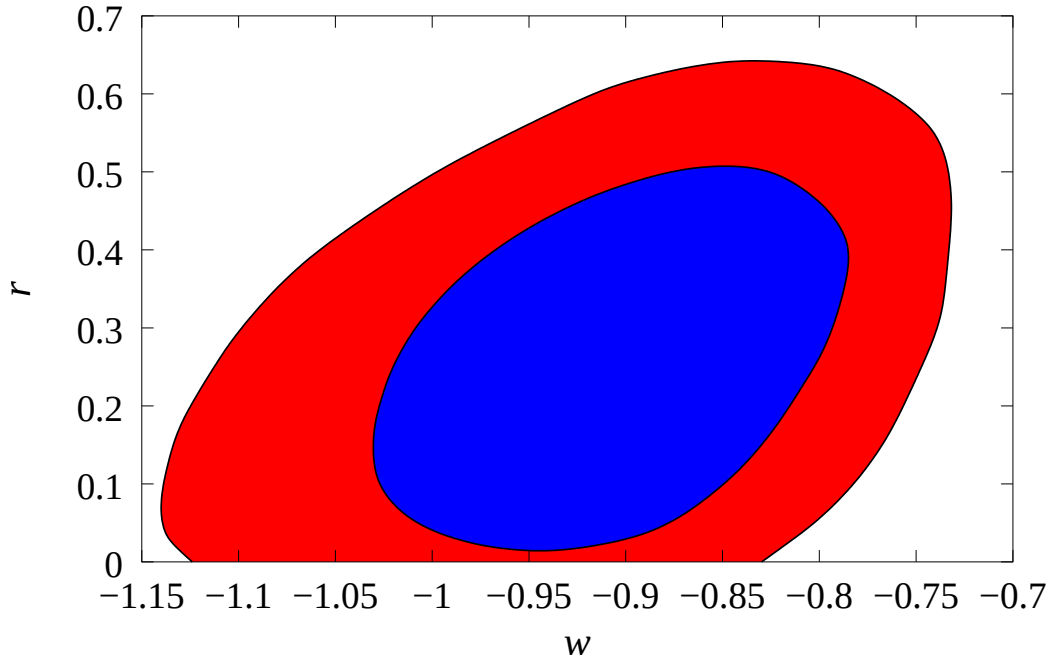

Figure 4.8: 68% and 95% contours in the (w, r) plane using the WMAP+SDSS-gal+bias+lya+SNIa constraints. The presence of tensors favors a slightly lower value of w, but the quality of the fit is only marginally improved and the cosmological constant model ($w = -1$) is near the 68% contours.

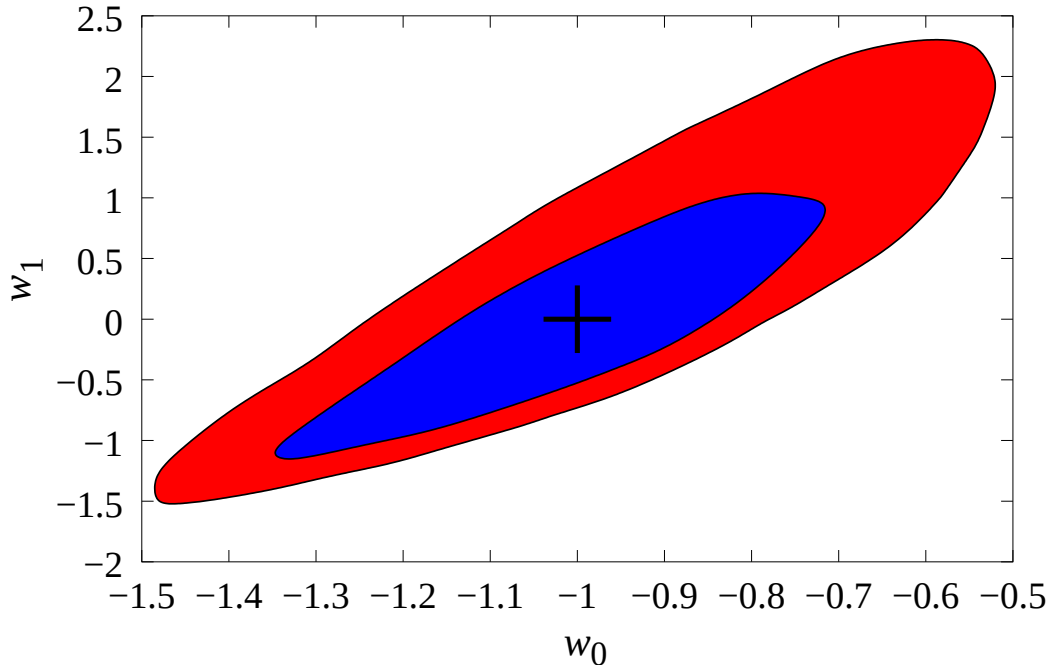

Figure 4.9: 68% (inner, blue) and 95% (outer, red) contours in the (w_0, w_1) plane using WMAP+SDSS-gal+bias+lya+SNIa measurements. We find that the simplest solution, $w_0 = -1$, $w_1 = 0$ (marked by a cross), fits the data best.

our expansion $0 < z < 1$ covers half of the full range of w so w_1 is being constrained in the regime of interest. If we impose $w_2 = 0$ then the best fit values and errors we find using all the data are

$$\begin{aligned} w_0 &= -0.981^{+0.193\ +0.384\ +0.568}_{-0.193\ -0.373\ -0.521} \\ w_1 &= 0.05^{+0.83\ +1.92\ +2.88}_{-0.65\ -1.13\ -1.38}. \end{aligned} \tag{4.15}$$

We find that $w_0 = -1$, $w_1 = 0$ is well within 1-σ contour and very close to the best fit model (figure 4.9).

The parameters w_0, w_1 and w_2 are strongly correlated, as shown in figure 4.9 for the first two, so the error on w_0 has expanded by a factor of 2 compared to the constant equation of state case. We can explore less model dependent constraints on $w(z)$ by computing the median and 1, 2-σ intervals from MCMC outputs at any redshift. Over a narrow range of redshift these contours will be nearly model independent as long as the equation of state is a relatively smooth function of redshift. We find that the data constrain best the equation

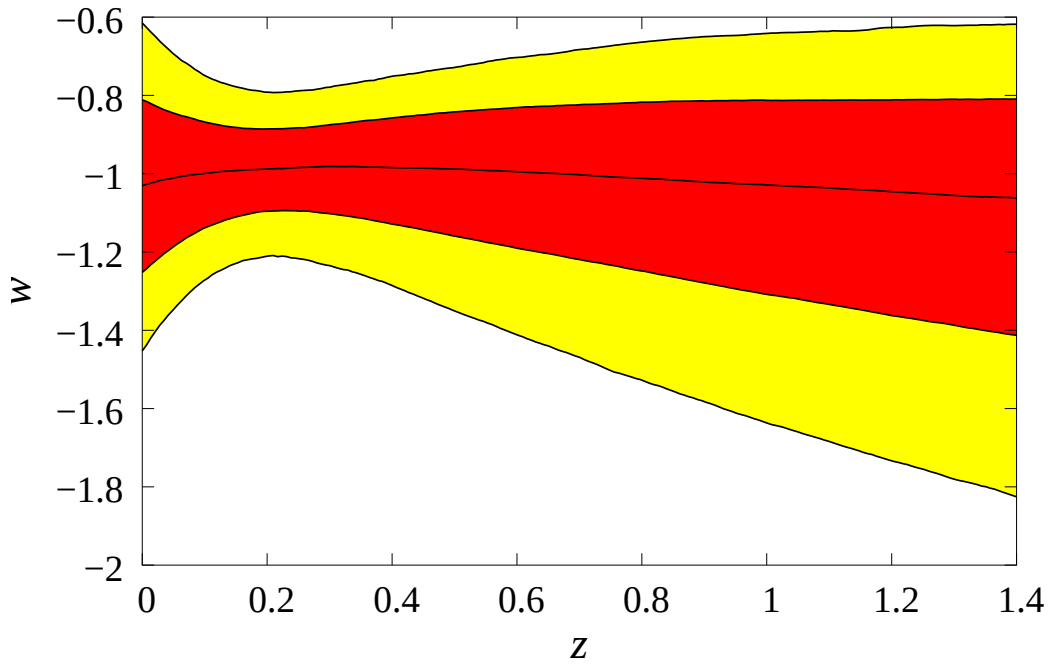

Figure 4.10: Median (central line), 68% (inner, red) and 95% (outer, yellow) intervals of $w(z)$ using all the data in the chains without tensors and with a 3 parameter expansion of equation of state with respect to the expansion factor. Very similar results are found for the 2 parameter expansion of w, so the constraints are reasonably model independent as long as w is a smooth function of redshift. We find that the simplest solution, $w = -1$, fits the data at all redshifts.

of state w at $z = 0.3$, where we find $w(z = 0.3) = -1.011^{+0.095\ +0.176\ +0.264}_{-0.099\ -0.215\ -0.357}$. Thus $z = 0.3$ is the pivot point for the current measurements of equation of state and the constraint here is nearly model independent. This is confirmed by our analysis with w_2. In this case we find severe degeneracies among the 3 paramaters, but the value at $z = 0.3$ is

$$w(z = 0.3) = -0.981^{+0.106\ +0.205\ +0.269}_{-0.120\ -0.249\ -0.386}, \tag{4.16}$$

which is nearly the same as for the two parameter analysis with $w_2 = 0$. These constraints are shown in figure 4.10.

The corresponding constraint at $z = 1$ for two parameter (w_0, w_1) analysis is $w(z = 1) = -1.00^{+0.17\ +0.27\ +0.33}_{-0.28\ -0.66\ -1.00}$. Adding w_2 we find

$$w(z = 1) = -1.03^{+0.21\ +0.39\ +0.52}_{-0.28\ -0.58\ -0.85}, \tag{4.17}$$

so 1-σ contours are nearly the same, while 2 and 3-σ contours expand in the positive direction

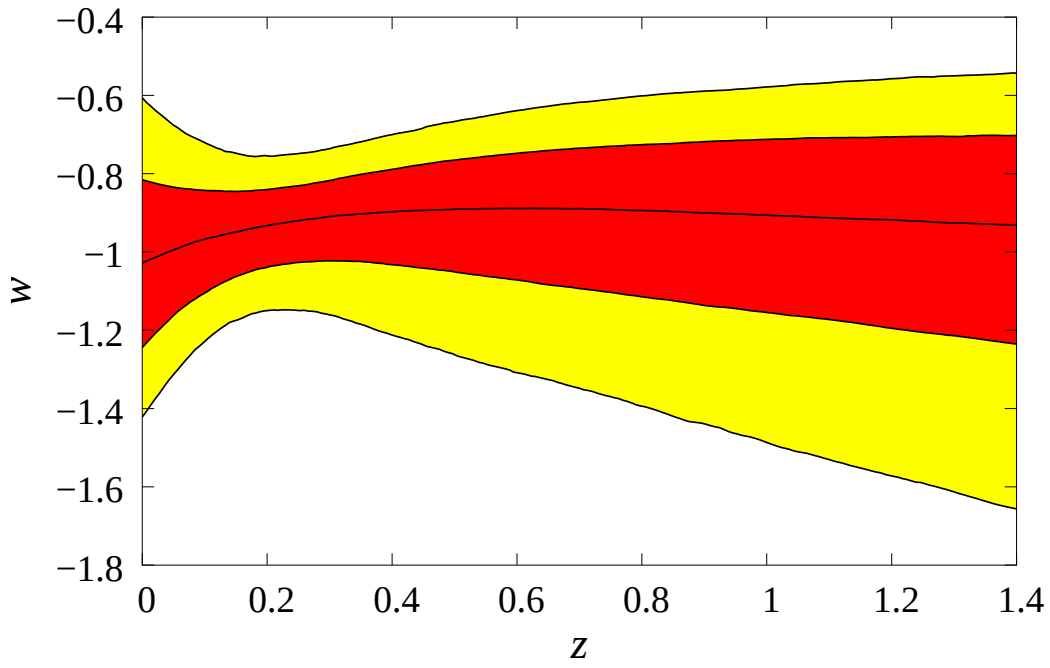

Figure 4.11: Same as Figure 4.10 but for MCMC with tensors.

and shrink in the negative direction compared to 2-parameter analysis. This value is thus also relatively independent of parametrization.

Adding tensors and running to the 3-parameter expanasion of w gives,

$$w(z = 0.3) = -0.914^{+0.089\ +0.169\ +0.229}_{-0.106\ -0.225\ -0.343} \tag{4.18}$$

and

$$w(z = 1.0) = -0.93^{+0.21\ +0.35\ +0.48}_{-0.25\ -0.56\ -0.90}. \tag{4.19}$$

This is shown in figure 4.11. Thus, in either case, there is no evidence for any time dependence of the equation of state and its value is remarkably close to -1 even at $z = 1$. As for a constant w analysis we find that tensors increase the preferred value of w by about 0.1. These constraints on the time dependence of w are significantly better compared to the 0.8-0.9 allowed variation between $z = 0$ and $z = 1$ found previously [77]. Lyα forest analysis measures the growth of structure in the range $2 < z < 4$ and so helps in constraining models with a significant component of dark energy present at $z > 2$ [120].

4.4 Implications for inflation

Inflation is currently the leading paradigm for explaining the generation of structure in the universe. Inflation, an epoch of accelerated expansion in the universe, explains why the universe is approximately homogeneous and isotropic and why it is flat [6, 7, 8, 9]. During this accelerated expansion quantum fluctuations are transformed into classical fluctuations when they cross the horizon (i.e., their wavelength exceeds the Hubble length during inflation) and can subsequently be observed as perturbations in the gravitational metric [11, 12, 13, 14, 15]. A generic prediction of a single field inflation models is that the perturbations are adiabatic (meaning that all the species in the universe are unperturbed on large scales except for the overall shift caused by the perturbation in the metric) and Gaussian. These predictions, together with flatness ($K = 0$), have been explicitly assumed in our analysis.

We note here that cyclic/ekpyrotic models [121] are an alternative to inflation, which, despite a very different starting point and without a period of accelerated expansion, lead to almost identical predictions as inflation [79]. Specifically, these models predict no observable tensor contribution, spectral index n_s close to unity, and negligible running [80]. Very specific forms of cyclic potentials have not been explored in much detail in these models and for this reason we will not discuss them explicitly below, but most of our constraints on the form of the inflationary potential can easily be translated into the corresponding constraints on the form of cyclic model potential.

Here we will explore a class of single field inflation models, in which there is a single field responsible for the dynamics of inflation (even though additional fields may be present or even required to end inflation, as in the case of hybrid inflation [122]). We will assume the early universe is dominated by a minimally coupled scalar field ϕ, which we will express in Planck mass units setting $8\pi G = 1$. During inflation the energy density is dominated by potential V. The Hubble parameter $H^2 = V/3$ is nearly constant and the equation of state is $w = p/\rho \sim -1$. Since $H = d\ln a/dt$ it follows that the expansion factor is exponentially increasing with time, $a = a_{\rm end}e^{H(t-t_{\rm end})}$. One can introduce the number of e-folds before

the end of inflation at time t_0 as

$$N = \ln(a_{\rm end}/a_0) = \int_{t_0}^{t{\rm end}} H(t)dt = \int_{\phi_0}^{\phi_{\rm end}} \frac{V}{V'}d\phi, \tag{4.20}$$

which can be computed for any specific form of the potential. Here we will define it to be the number of e-folds before the end of inflation when the pivot point, $k_{\rm pivot} = 0.05/{\rm Mpc}$, crosses the horizon. Note that the usual definition is with respect to the largest observable scale, $k \sim 10^{-3}/{\rm Mpc}$, which corresponds to $\Delta N = 4$ larger number of efolds. The latter number is expected to be between 50-60 efolds for standard inflation (64 for $V \propto \phi^4$), but could be as low as 20 or as high as 100 in special cases [123, 124]. For our pivot point choice we will thus adopt $N = 50$ as the standard value (60 for $V \propto \phi^4$), but also explore more general constraints on it.

If the kinetic energy density were negligible all the time the universe would keep exponentially expanding and there would be no end to inflation. Typically therefore one must have deviations from the pure $w = -1$ case. These deviations lead not only to a finite number of efolds, but also break the scale invariance of the primordial power spectrum. Since we know from current observational constraints that $r < 1$ and $n_s \sim 1$ we can adopt the slow-roll approximation to relate the form of the potential to the observed quantities r, n_s, α_s, and $\Delta^2_{\mathcal{R}}$. The slow-roll parameters are defined as [27]

$$\begin{aligned} \epsilon_V &= \frac{1}{2}\left(\frac{V'}{V}\right)^2 \\ \eta_V &= \frac{V''}{V} \\ \xi_V &= \frac{V'V'''}{V^2}. \end{aligned} \tag{4.21}$$

Note that in some early literature the 3rd slow-roll parameter ξ was denoted as ξ^2 to emphasize the point that it is generically of second order in ϵ or η [125]. We will not use this notation since ξ can be positive or negative and since it does not have to be of second order in the slow-roll expansion.

The relations between the slow-roll parameters and observables are

$$\begin{aligned} \Delta^2_{\mathcal{R}} &= \frac{V}{24\pi^2\epsilon_V} \\ r &= 16\epsilon_V \\ n_s - 1 &= -6\epsilon_V + 2\eta_V \\ \alpha_s &= 16\epsilon_V\eta_V - 24\epsilon_V^2 - 2\xi_V. \end{aligned} \tag{4.22}$$

As mentioned in the previous section, we assume $r = -8n_T$ and do not consider the running of the tensor spectral index, both of which should be valid for single field inflation in the relevant regime.

Traditionally the inflationary models are divided into separate classes depending on the value of first two slow-roll parameters [126, 127, 27]. Figure 4.12 shows the distribution in the (ϵ_V, η_V) plane. We see that both positive and negative values of η are allowed and that there is a strong correlation between the two from the observational constraints, a consequence of positive correlation between tensors and primordial slope. Figure 4.13 shows the distribution in the (η_V, ξ_V) plane. Both parameters are consistent with 0. The basic constraints are $\epsilon < 0.03$, $-0.04 < \eta < 0.12$ and $-0.015- < \xi_V < 0.035$, so all slow roll parameters are small.

4.4.1 Large field models

The simplest inflationary models are the monomial potentials, $V = V_0\phi^p$, for which the first two parameters are comparable, $\epsilon \sim \eta$, and the curvature is positive, $\eta > 0$. These potentials occur in chaotic inflation models [128]. In these models a deviation from scale invariance, $n_s - 1 = -(2+p)/2N$, also implies a significant tensor contribution, $r = 4p/N$, while running is negligible, $\alpha_s = -2(n_s-1)^2/(p+2) = -(p+2)/2N^2$. Because both slow-roll parameters are of order $(p/\phi)^2$ these chaotic inflation-type potentials require a large field, $\phi > 1$, to satisfy observationally required $r < 1$ and $n_s \sim 1$. For this reason these models are sometimes called large field models. While this may limit their particle physics motivation there are brane inspired models where this property can be justified [129]. More

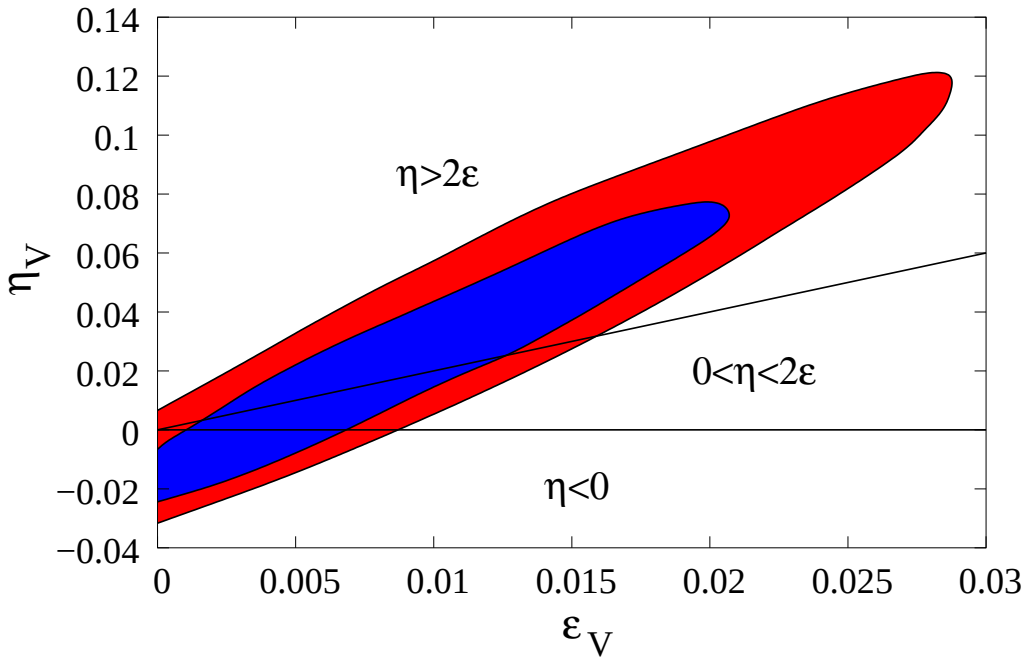

Figure 4.12: 68% (inner, blue) and 95% (outer, red) contours in the (ϵ_V, η_V) plane using all the measurements without running (Table 4.1, 5th column). Also shown are the regions occupied by the 3 classes of inflationary models. All 3 classes of models are allowed, but individual models within each class are constrained. Note that the solutions disfavor low energy models ($\epsilon_V = 0$) with large positive curvature ($\eta_V > 0$), typical of hybrid inflation models, as well as models where both ϵ_V is large and $\eta_V < \epsilon_V/2$, typical of chaotic inflation models with steep potentials.

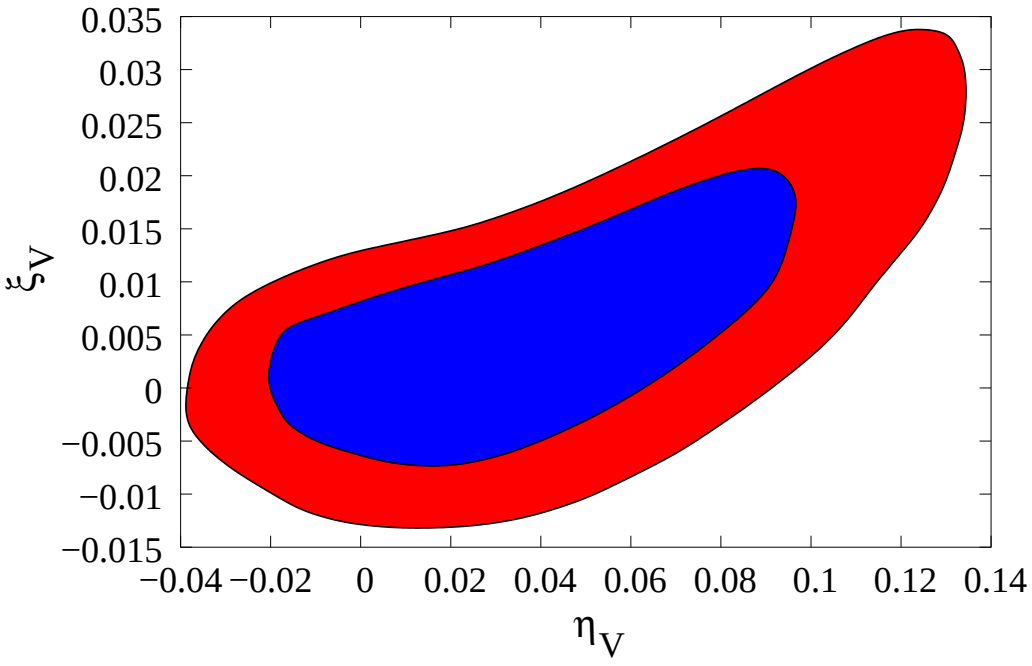

Figure 4.13: 68% (inner, blue) and 95% (outer, red) contours in the (η_V, ξ_V) plane from MCMC with running and tensors.

generic parametrization of these models in terms of curvature is $0 < \eta_V < 2\epsilon_V$.

With the exception of $p = 2$, chaotic models are not particularly favored from our analysis. Figure 4.2 shows the position in the (r, n_s) plane for two representative cases, $p = 2$ and $p = 4$. We find that the $V \propto \phi^2$ model ($n_s = 0.96$, $r = 0.16$ for N=50) is within the 2-sigma contour, while the $V \propto \phi^4$ model ($n_s = 0.95$, $r = 0.27$ for N=60) is outside the 3-sigma contour, since it predicts more tensors and a redder spectrum for that tensor amplitude than observed. Figure 4.14 shows all chain elements with $n_s < 1$ converted to (p, N) values using the expressions above. For standard inflation we require $N < 60$ and this limits us to $p < 3$. Similarly, figure 4.12 shows that $\epsilon_V > \eta_V/2$ with large ϵ_V models are disfavored.

For specific models we also minimized χ^2 by exploring all of the parameter space of the remaining parameters and compared that to the global minimum in χ^2. We find $\Delta\chi^2 = 5$ for the $V \propto \phi^2$ model and $\Delta\chi^2 = 13$ for the $V \propto \phi^4$ model. These results are in agreement with the MCMC results and show that the latter case is excluded at more than $3 - \sigma$

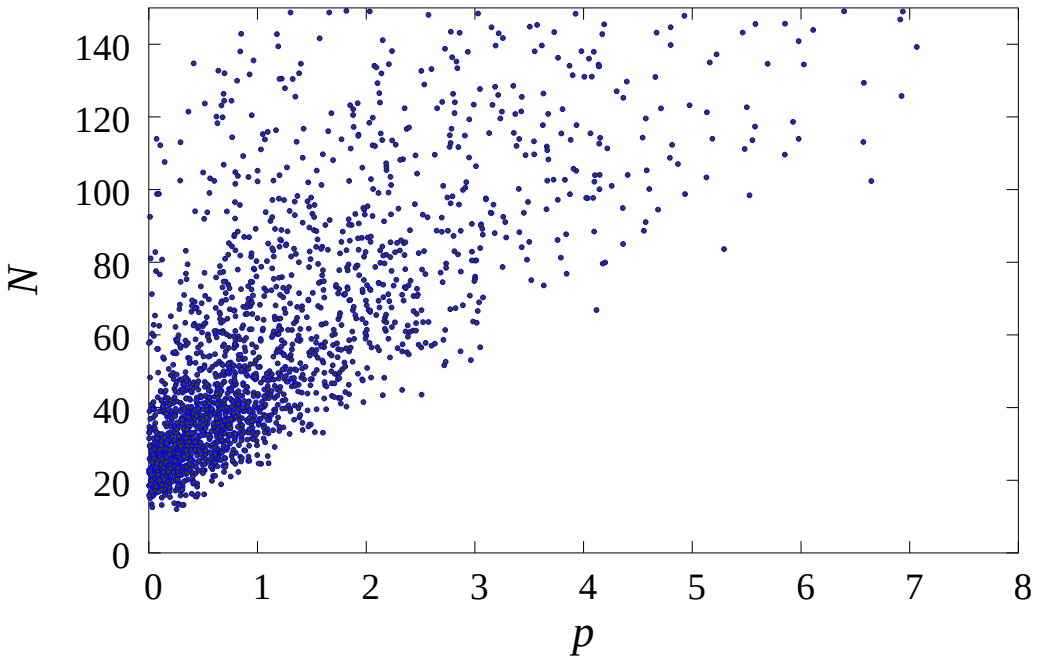

Figure 4.14: Scatter plot of MCMC solutions with $n_s < 1$ converted into the (p, N) plane assuming relations valid for chaotic inflation models. Here p is the slope of the inflationary potential and N is the number of e-folds. For $N < 60$ we require $p < 3$.

confidence.

4.4.2 Large positive curvature models

We turn next to models with positive large curvature, $\eta > 2\epsilon$. A generic potential of this type can be obtained by adding a constant to the monomial potential, $V = V_0(1 + c\phi^p)$, where c is a positive dimensionless constant. These models allow small field solutions to inflation, $\phi \ll 1$, and so are popular for model building in the context of supersymmetry. In this limit, and if dimensionless c is not too large, one has $\epsilon \ll 1$. In such models, inflation never ends (since the potential never drops to zero), so another field must be brought in to accomplish this. Hybrid inflation is an example of such a mechanism [122]. If ϵ is small then these models predict $r \sim 0$ and $n_s > 1$ (equations (4.22), the latter condition requires $\epsilon < \eta/3$). For $p = 2$ the slope is constant, $n_s - 1 = 2c$ and there is no running, while for $p > 2$ running is negative and is given by $\alpha_s = -(p-2)/(p-1)[(n_s-1)]^2/2$. This is always small since a large deviation in the $n_s > 1$ direction is strongly disfavored, so $\alpha_s \sim 0$. Some

of these models are disfavored: for $r = 0$ and in the absence of running we find $n_s < 1.0$ at 90% confidence and $n_s < 1.04$ at 99.9% confidence, so if $\epsilon_V \sim 0$ then $\eta_V > 0.02$ is excluded at 3 sigma. Thus the deviations from scale invariance have to be very small for these models to be acceptable.

4.4.3 Large negative curvature models

The most promising models from the observational perspective are negative curvature models, $\eta < 0$. As noted above, the main reason that large positive curvature models are disfavored is that in the absence of tensors the data favor $n_s < 1$, while small positive curvature models are disfavored because they predict large tensors and a red spectrum at the same time, whereas the data are more consistent with blue spectrum if tensors are significant. A generic potential of negative curvature models can be obtained by switching the sign on the hybrid potential form, $V = V_0(1 - c\phi^p)$, where c is a positive dimensionless constant. In these models the field ϕ is slowly rolling from low to high values until reaching the point where the potential vanishes at $c\phi^p = 1$, at which point inflation stops. This is a generic scenario of spontaneous symmetry breaking models as in the first working inflation model, that of new inflation [8]. For $p = 2$ the slope is again constant at $n_s - 1 = -2c$ and there is no running.

In these models one has $n_s - 1 = -2(p-1)/(p-2)/N$ and $\alpha_s = -(p-2)/(p-1)[(n_s - 1)]^2/2$. The running is of order $(n_s - 1)^2/2$ and the prefactor is unity at best, so running is negligible. The slope n_s ranges between 0.96 (in the limit of $|p| \to \infty$,where $n_s - 1 = -2/N$) and 1, in excellent agreement with observational constraints.

One finds good agreement using other potentials proposed in the literature, such as the potential based on one-loop correction in a spontaneous symmetry broken SUSY [130]. The potential is of the form $V = V_0[1 + \alpha \ln(\phi/Q)]$. In this model the number of e-folds is of the order $N = \phi^2/2\alpha$ (this expression works best if $\alpha \ll 1$). This model predicts $n_s - 1 = -2\alpha[1 + 3\alpha/2]/\phi^2$ and $\alpha_s = -(n_s - 1)^2[2\alpha + 3\alpha^2/2 + 1/2]/[1 + 3\alpha/2]^2$. Running is again negligible. Solutions with $\phi \ll 1$ require $\alpha \ll \phi^2 \ll 1$, in which case the slope

becomes $n_s - 1 = -1/N = -0.02$ for $N = 50$, in excellent agreement with the observed value $n_s = 0.971^{+0.023}_{-0.019}$.

Many other models in this class also work. A model often mentioned as an example of allowing a large running is the softly broken SUSY model with $V = V_0(1 - c\phi^2(\ln(\phi/\phi_*) - 1/2)/2$. This model has a large 3rd derivative for small field ϕ, $V'''/V_0 = -c/\phi$, so it can lead to large ξ and large runnings. For this model there is an inequality relation between slope and running of the form $\alpha_s > -\frac{1}{4}(n_s - 1)^2 > -2 \times 10^{-3}$, so a large negative running cannot be accommodated in this model for the allowed values of n_s. Our solutions do not favor large negative runnings anyways, unless one is willing to consider models with massive neutrinos whose mass exceeds 0.3eV, so this model is acceptable, but it can overpredict the running on the positive side.

There are also examples of models which can change from one inflationary case to the other, such as hybrid model with one-loop correction [131],

$$V = V_0 \left[1 + \alpha \left(\ln(\phi/Q) + \frac{c}{4}\left(\frac{\phi}{\phi_0}\right)^p\right)\right],$$

which under specially arranged conditions causes the slope to change from $n_s > 1$ on large scale to $n_s < 1$ on small scale. Again, there is no evidence for such a transition in the data, so there is no need to consider these special cases.

Finally, there are models that predict the simplest possible case of $r = 0$, $n_s = 1$ and $\alpha_s = 0$ [132]. These models are perfectly acceptable from our data.

While we only surveyed a small subset of inflationary models here, it is clear that their generic prediction is a nearly scale invariant spectrum, $|n_s - 1| < 0.05$, little or no tensors, $r < 1$ and small running, $\alpha_s \sim 10^{-3}$. All of these predictions agree with our constraints. Running is a particularly powerful test of standard inflationary (and cyclic) models in the sense that if running turned out to be large, a large class of inflationary models would have been eliminated. The original suggestions of running in the WMAP data sparked a lot of theoretical interest in inflationary models with running [24, 25], but such models are unnatural in the sense that they require a feature in the potential at exactly the scale of observations today. Our results suggest that the natural prediction of inflation, small

running, is confirmed by observations.

4.5 Conclusions

In this paper we performed a joint cosmological analysis of WMAP, the SDSS galaxy power spectrum and its bias, the SDSS Lyα forest power spectrum, and the latest supernovae SNIa sample. We work in the context of current structure formation models, such as inflation or cyclic models, so we assume spatially flat universe and adiabatic initial conditions. We also ignore more exotic components such as warm dark matter. The new ingredients, SDSS Lyα forest and SDSS bias, lead to a significant reduction of the errors on all the parameters. Many parameters are improved in accuracy by factors of two or more. For example, for the amplitude of fluctuations we find $\sigma_8 = 0.90 \pm 0.03$ and for the matter density we find $\Omega_m = 0.28 \pm 0.02$, both a significant improvement over previous constraints. From the fundamental physics perspective the highlights of the new constraints are:

1) The scale invariant primordial power spectrum is a remarkably good fit to the data and there is no evidence that the spectral index deviates from the scale invariant value $n_s = 1$, nor is there any evidence of its running with scale. We also find no evidence of tensors in the joint analysis. The constraints on running have improved by a factor of 3 compared to an analysis without the new Lyα forest constraints. These provide a data point at $2 < z < 4$ and $k \sim 1$/Mpc, a significantly smaller scale than scales traced by the CMB and galaxies.

2) There is no cosmological evidence of neutrino mass yet. In the standard models with 3 neutrino families we find for the total neutrino mass $\sum m_\nu < 0.42$eV (95% c.l.). When our analysis is combined with atmospheric and solar neutrino experiments [92, 93] we find that neutrino masses are not degenerate: the most massive neutrino family has to be at least 10% more massive than the least massive family, $m_3/m_1 > 1.1$: the mass of the least massive neutrino family has to be $m_1 < 0.13$eV, and that of the most massive neutrino family $m_3 < 0.15$eV, both at 95 % c.l. In alternative models with a 4th massive neutrino family in addition to 3 (nearly) massless ones we find $m_\nu < 0.79$eV, excluding all of the

allowed LSND islands at 95% c.l.

3) Dark energy continues to be best characterized as a standard cosmological constant with constant energy density and equation of state $w = -1$. When all the data is combined together the error on w is 0.09, a reduction compared to previously published values [2, 116, 77]. A cosmological constant with $w = -1$ is remarkably close to the best fit value for a variety of different subsamples of the data. A significant region of phantom energy parameter space with $w < -1$ is excluded, as are some of the tracker quintessence models with $w \sim -0.7$. The current data do not support any time dependence of the equation of state.

As the statistical errors are being reduced the required level at which systematics must be controlled increases as well. Our limits on cosmological parameters assume that the errors from the SDSS Lyα forest SDSS power spectrum shape, SDSS bias, WMAP CMB power spectrum, and the SNIa data are all properly characterized by the authors and that there are no additional sources of systematic error. Each one of these ingredients has to be tested and redundancy is necessary for the results to be believable. In our extensive tests we find no evidence of a disagreement between the different observational inputs, but further tests with these and other data sets are needed to verify and confirm our results. In addition, the upcoming 2 year analysis of WMAP polarization will improve the constraints on the optical depth and reduce the errors on parameters correlated with it.

Tests of the basic model are particularly important for Lyα forest , which is responsible for most of the improvement on the primordial power spectrum shape and amplitude. Despite the extensive tests presented in [90], more work is needed to investigate all possible physical effects that can modify its distribution and to see how these may affect the conclusions reached in this paper. Some of these tests will come from the ongoing work on SDSS data, such as the bispectrum analysis. Similarly, more work is needed to verify the accuracy of simulations with independent hydrodynamic codes. The present analysis, together with its sister papers [89, 90], is not the final word on this subject, but merely a first attempt to take advantage of the enormous increase in statistical power given by the SDSS data [82].

Current analysis marginalizes over many physical processes that have little or no external constraints and as a result the statistical power of cosmological constraints from the Lyα forest is weakened. Better theoretical understanding of these processes together with external constraints from additional observational tests could lead to a significant reduction of observational errors on the primordial slope and its running even with no additional improvements in the observations.

In summary, adding SDSS Lyα forest and SDSS bias constraints to cosmological parameter estimation leads to a significant improvement in the precision with which the cosmological parameters can be determined. Despite these improvements we find no surprises. Many of these results are not unexpected, but the tightness of the constraints is rapidly eliminating many of the alternative models of structure formation, neutrinos and dark energy. Future cosmological observations and improvements in theoretical modelling will allow us to verify the constraints found here and improve them further. As the constraints become tighter there may be additional surprises awaiting us in the future.

Chapter 5

Progress in Measuring the Probability Distribution Function of Ly-α forest flux from SDSS quasars sample

5.1 Introduction

Ly-α forest absorption is usually observed in quasar spectra. It arises from continuosly fluctuating photoionized gas in the intergalactic meduim, with density near the universal mean and temperatures around 10^4 K. The behavior of the absorption field can be acquired from primordial spectrum of fluctuations with reasonable accuracy using numerical simulations [89, 133].

The observations of the Ly-α forest are usually described in the form of transmitted flux fraction, $F(\lambda) = \exp[-\tau(\lambda)]$. Usually power spectrum $P_F(k, z)$ of the transmitted flux fraction is used to compare the observations [133]. There have been attempts to study the bispectrum of Ly-α forest [120].

In this chapter we present our progress in measuring the probability distribution function

$p(F)$ of the flux F. Measurement of the probability distribution function of the transmitted flux should help to constrain better the mean transmitted flux, which is one of the essential parameters in the measurement of the power spectrum. Better measurement of Ly-α forest absorption lets us better constrain the primordial spectrum of fluctuations, and, therefore, lets us better constrain the inflationary potential.

In order to apply our method for measuring the probability distribution function, we first investigate how well it works on simulated MOCK spectra.

5.2 Theoretical PDF of Ly-α forest

The linear theory of Ly-α forest used for the generation of the MOCK spectra is based on the following equations:

$$F = e^{-\tau}, \tag{5.1}$$

$$\tau = A\rho^{\alpha}, \tag{5.2}$$

$$\rho = e^{\delta + C}. \tag{5.3}$$

Here δ is a Gaussian random variable with variance σ, τ is the optical depth to Ly-α absorption, and ρ is the mass density. The value of α usually lies in the range between 1.6 and 2.0. In Mock spectra simulations we used $C = -\sigma^2/2$ and $\alpha = 2$. The probability distribution function of δ is given by the expression

$$p(\delta) = \frac{1}{\sigma\sqrt{2\pi}} \exp\left(-\frac{\delta^2}{2\sigma^2}\right). \tag{5.4}$$

In order to find the distribution of F, we just use the fact that

$$p(\delta)d\delta = p(F)dF. \tag{5.5}$$

After plugging in the expression for F through δ

$$F = \exp\left(-Ae^{\alpha(\delta+C)}\right) = \exp\left(-Ae^{\alpha C}\ e^{\alpha\delta}\right). \tag{5.6}$$

Now for simplicty we denote $A' = Ae^{\alpha C}$ and $\sigma' = \alpha\sigma$. Then for the probability distribution function of F we get

$$p(F) = \frac{1}{\sigma'\sqrt{2\pi}} \frac{1}{F(-\ln F)} \exp\left(-\frac{1}{2\sigma'^2} \ln^2 \frac{-\ln F}{A'}\right). \tag{5.7}$$

From here we see that the original values of σ, α, C and A do not significantly matter since they are swept into just two variables σ' and A'.

It is easy to check that the following equalities for equation (5.7) hold:

$$\ln A' = \int_0^1 \ln(-\ln F)\ p(F)dF, \tag{5.8}$$

$$\sigma'^2 = \int_0^1 \left(\ln(-\ln F) - \ln A'\right)^2\ p(F)dF. \tag{5.9}$$

Equation (5.7) is what one could observe with ideal instruments. After pixelizations and smoothing the spectra by SDSS resolution, the probability distribution function function changes: the peak of the function becomes narrower and taller, and the tails get more power. Nevertheless we will use these formula (5.7) in order to estimate the tilt and the curvature of our probability distribution function within the bins.

5.3 Reconstruction technique

We divide all the data into 13 redshift bins of width 0.2 between redshifts 2.1 and 4.7. Within each redshift bin we use maximum likelihood method in order to reconstruct the probability distribution function (pdf) of Ly-α forest flux. We parametrize the pdf in the form of N bins each with equal width of dF within each redshift bin.

We choose dF to be less than 95–65% flux rms errors for all the pixels in one redshift bin. Lower redshift bins contain up to $200,000$ pixels from about 2000 spectra, higher redshift bins contain down to $7,000$ pixels from about 50 spectra.

5.4 Smoothing the spectra

We know the flux at each pixel up to some "constant". If the "constant" is the same everywhere, we can just found the average of the flux all over the pixels and get rid of the

constant by making the transformation

$$f_j = F_j/\bar{F}. \tag{5.10}$$

In this case the value of f_j would not depend on the normalization "constant." The flux from the quasar is not exactly flat and one needs to take into account the deviations from being exactly flat.

In order to take into account the changing mean flux due to different effects in the emission quasar spectra, we find the "local" mean flux by averaging the flux around the point of interest:

$$\bar{F}_l = \sum_{j=0}^{N-1} F_j \frac{\Delta v}{v_{\rm sm}\sqrt{2\pi}} e^{-\Delta v_{lj}^2/2v_{\rm sm}^2} \tag{5.11}$$

Here summation is assumed over every pixel j. The value $\bar{F}_l$ is the mean flux at pixel l. The comoving difference in speeds between pixels l and j can be expressed as

$$\Delta v_{lj} = c\frac{\Delta\lambda_{lj}}{\lambda}, \tag{5.12}$$

where c is the speed of light and λ is the wavelength. Usually we have $\Delta\lambda \ll \lambda$, therefore it does not make difference if we take λ_i or λ_j as λ. Since pixels are about the same wavelength apart from each other, we can assume that

$$\Delta v_{lj} = (l-j)\Delta v, \tag{5.13}$$

where $\Delta v \approx 68 - 72$ km/s is the comoving velocity difference between any two adjacent pixels.

We take the smoothing velocity $v_{\rm sm} = 750$ km/s, this is the characteristic scale beyond which Ly-α forest power is not significant. This scale is also used in the reconstruction of the Ly-α forest power spectrum in [133].

If F_j has a Fourier transform F_k in the form of

$$F_j = \frac{1}{N}\sum_{k=0}^{N-1} F_k e^{i2\pi\frac{k}{N}v_j}, \tag{5.14}$$

and $\bar{F}_i$ is transformed through $\bar{F}_k$ in the form of

$$\bar{F}_l = \frac{1}{N}\sum_{k'=0}^{N-1} \bar{F}_{k'} e^{i2\pi \frac{k'}{N} v_l}. \tag{5.15}$$

Equation (5.11) is equivalent to

$$\bar{F}_k = F_k e^{-\frac{4\pi^2 k^2}{N^2 \Delta v^2} v_{\rm sm}^2/2}. \tag{5.16}$$

for Fourier transforms of the original and smoothed fluxes F and $\bar{F}$.

Let us now assume that each pixel with flux F_j has an error of the flux measurement of σ_j. Let us find the error of the "local" average flux $\sigma_{\bar{F}_l}$.

We assume the errors of the adjacent pixels to be independent, then accoring to the rule of summing independent measurements from equation (5.11) we get

$$\sigma_{\bar{F}_l}^2 = \sum_{j=0}^{N-1} \left(\sigma_j \frac{\Delta v}{v_{\rm sm}\sqrt{2\pi}} e^{-\Delta v_{lj}^2/2v_{\rm sm}^2} \right)^2. \tag{5.17}$$

Bringing equation (5.17) to the form of equation (5.11) we find that

$$\sigma_{\bar{F}_l}^2 = \frac{\Delta v}{2v_{\rm sm}\sqrt{\pi}} \sum_{j=0}^{N-1} \sigma_j^2 \frac{\Delta v\sqrt{2}}{v_{\rm sm}\sqrt{2\pi}} \exp\left(-\frac{\Delta v_{lj}^2}{2(v_{\rm sm}/\sqrt{2})^2} \right), \tag{5.18}$$

i.e. that the variance of the average is the smoothed with kernel $v_{\rm sm}/\sqrt{2}$ variance of individual pixels multiplied by a constant.

Since we are primarily interested in the value of

$$f = \frac{F}{\bar{F}}, \tag{5.19}$$

its error is given as

$$\frac{\sigma_f^2}{f^2} = \frac{\sigma_F^2}{F^2} + \frac{\sigma_{\bar{F}}^2}{\bar{F}^2} - {\rm corr}(F,\bar{F}) \sqrt{\frac{\sigma_{\bar{F}}^2}{\bar{F}^2}\frac{\sigma_F^2}{F^2}}. \tag{5.20}$$

We will use these expressions to estimate the errors of the value of f for reconstructing the probability distribution function. By our estimates the correlation ${\rm corr}(F,\bar{F})$ between F and $\bar{F}$ is of the order of 1/10 and we disregard it. Taking the average error into account increases the error by 1–2% for an average spectrum.

5.5 Subtracting the noise through maximizing the likelihood

The likelihood function for all the pixels in one redshift bin can be written as

$$\mathcal{L} = \prod_{\lambda} \left[\int_0^{f_{max}} p(f) \exp\left(-\frac{1}{2} \frac{(f - f_\lambda)^2}{\sigma_\lambda^2} \right) \, df \right]. \tag{5.21}$$

(we are looking into option of considering $\sigma_{\lambda,f}$ instead of σ_λ in order to take into account not exactly "gaussianity" of the noise due to poisson noise contribution from the quasar continuum)

In equation (5.21) we have a product of likelihoods of individual pixels λ. The value of f_{max} is chosen to cover the whole range of possible values of fluxes. Function $p(f)$ is the probability distribution function we are looking for.

5.5.1 Parameterization of PDF

At first we parameterize $p(f)$ to be constant within each bin dF, we also choose numbers $x_0, x_1, \ldots, x_n$ corresponding to each bin so, that

$$p(f \in i\text{-th bin}) = \frac{x_i^2}{\sum\limits_j x_j^2}. \tag{5.22}$$

We assign x_i for one of the bins in the center of the probability distribution function ($f = 1$) where we most certainly have non-zero value of probability distribution function to 1 and assign number N to it. This way our parameterization looks as

$$\begin{array}{cccccc} i & 0 & \ldots & N & \ldots & N-1 \\ p_i & \dfrac{x_0^2}{1 + \sum\limits_j x_j^2} & \cdots & \dfrac{1}{1 + \sum\limits_j x_j^2} & \cdots & \dfrac{x_{N-1}^2}{1 + \sum\limits_j x_j^2} \end{array}. \tag{5.23}$$

This parameterization provides us with always non-negative probability distribution function and it also constrains the integral of the probability distribution function $p(f)$ over f to 1:

$$\int_0^{f_{max}} p(f) \, df = 1. \tag{5.24}$$

Using this parameterization, the logarithm of the likelihood function (5.21) looks as

$$\ln \mathcal{L} = \sum_{\lambda} \ln \left[\frac{\sum_i \alpha_{i,\lambda} x_i^2}{1+\sum_i x_i^2} + \frac{\alpha_{N,\lambda}}{1+\sum_i x_i^2} \right]$$
$$= \sum_{\lambda} \left[\ln(\alpha_{N,\lambda} + \sum_i \alpha_{i,\lambda} x_i^2) - \ln(1+\sum_i x_i^2) \right] \quad (5.25)$$

Here we defined $\alpha_{i,\lambda}$ as

$$\alpha_{i,\lambda} = \frac{\int\limits_{df_i} p(f) \exp\left(-\frac{1}{2}\frac{(f-f_\lambda)^2}{\sigma_\lambda^2}\right) df}{\int\limits_{df_i} p(f)\, df}. \quad (5.26)$$

with the integration performed over i-th bin. Equation (5.26) can be simplified in case of a constant $p(f)$ within the bin:

$$\alpha_{i,\lambda} = \frac{\int\limits_{df_i} \exp\left(-\frac{1}{2}\frac{(f-f_\lambda)^2}{\sigma_\lambda^2}\right) df}{\int\limits_{df_i} df}. \quad (5.27)$$

For minimization routine we will need the first derivatives of the logarithm of the likelihood function (5.25) over x_j:

$$\frac{\partial \ln \mathcal{L}}{\partial x_j} = 2x_j \sum_{\lambda} \left[\frac{\alpha_{j,\lambda}}{\alpha_{N,\lambda} + \sum_i \alpha_{i,\lambda} x_i^2} - \frac{1}{1+\sum_i x_i^2} \right] \quad (5.28)$$

We use standard minimization routines from Gnu Scientific Library which require the calculation of the function and its derivatives for the minimization.

5.6 Corrections to the likelihood function

While testing our noise subtraction routine on simple distributions, we found that for such large volumes of data as we have in the first several redshift bins from SDSS with, it is not enough to consider the probability distribution function to be a constant within a f-bin. We cannot reduce the size of the bin, since the minimization routine becomes highly unstable and produces a "forest"-like probability distribution function . For the low-redshift bins we have the rms of about 90% pixels larger than the width of our parameterization bin. It is impossible to reduce the size of the bins for the level of noise we have in our data.

We found disagreement with our test models in the bins where the slope of the probability distribution function is large, i.e. where there is a big sudden change in the value of probability distribution function between adjacent bins. In order to correct for this effect we take a function which somewhat looks like a pdf we need to reconstruct. It is important to note that we neither require this function $A(f)$ to be exactly like the probability distribution function we are trying to reconstruct, nor do we even need it to have properties of probability distribution function such as e.g.

$$\int_0^{f_{max}} A(f)\, df = 1. \tag{5.29}$$

We just require that the function approximately had a slope similar to the slope of the underlying probability distribution function in the problematic bins.

It is easy to correct for this effect if one takes a look at equation (5.26), we can just substitute $p(f)$ with $A(f)$ as

$$\alpha_{i,\lambda} = \frac{\int\limits_{df_i} A(f) \exp\left(-\frac{1}{2}\frac{(f-f_\lambda)^2}{\sigma_\lambda^2}\right) df}{\int\limits_{df_i} A(f)\, df}. \tag{5.30}$$

In this case our underlying probability distribution function will be approximated within the bins in the following manner:

$$p(f) = p_i \frac{A(f) df_i}{\int\limits_{df_i} A(f)\, df} \tag{5.31}$$

5.7 Results

Current results are present at Figure 5.2. At first glance one can wrongly assume that our reconstruction (`"mock.noiseless.averages.dat" u 1:2:3`) is a good fit to the original noiseless MOCK spectra (`"mock.fake.PDF.00.dat" in 0 u 1:2`). Actually, one should compare our results to the same binning noiseless MOCK spectra probability distribution function histotram (`"mock.fake.PDF.00.dat.1" in 0 u 1:2`). For 15 data points we get χ^2 value of 150 if one takes the correlations between the bins into account (see Figure-fig:correlation). Without taking the correlations between the bins χ^2 reduces to 50.

Apparently the MOCK simulations produce spectra with correlated flux and its noise due to Poisson noise simulation from the quasar continuum. We tried to simulate uncorrelated noise for each pixel and in this case our noise subtraction procedure worked fine. Currently we are trying to include the Poisson noise correction into our algorithm.

To conclude, in this chapter we demonstrated that our approach of finding the probability distribution function through minimizing the likelihood function using the parameterization (5.23) workse reliably well. We managed to reconstruct the probability distribution function from data which contained 95% pixels with noise level larger than the width of the bin.

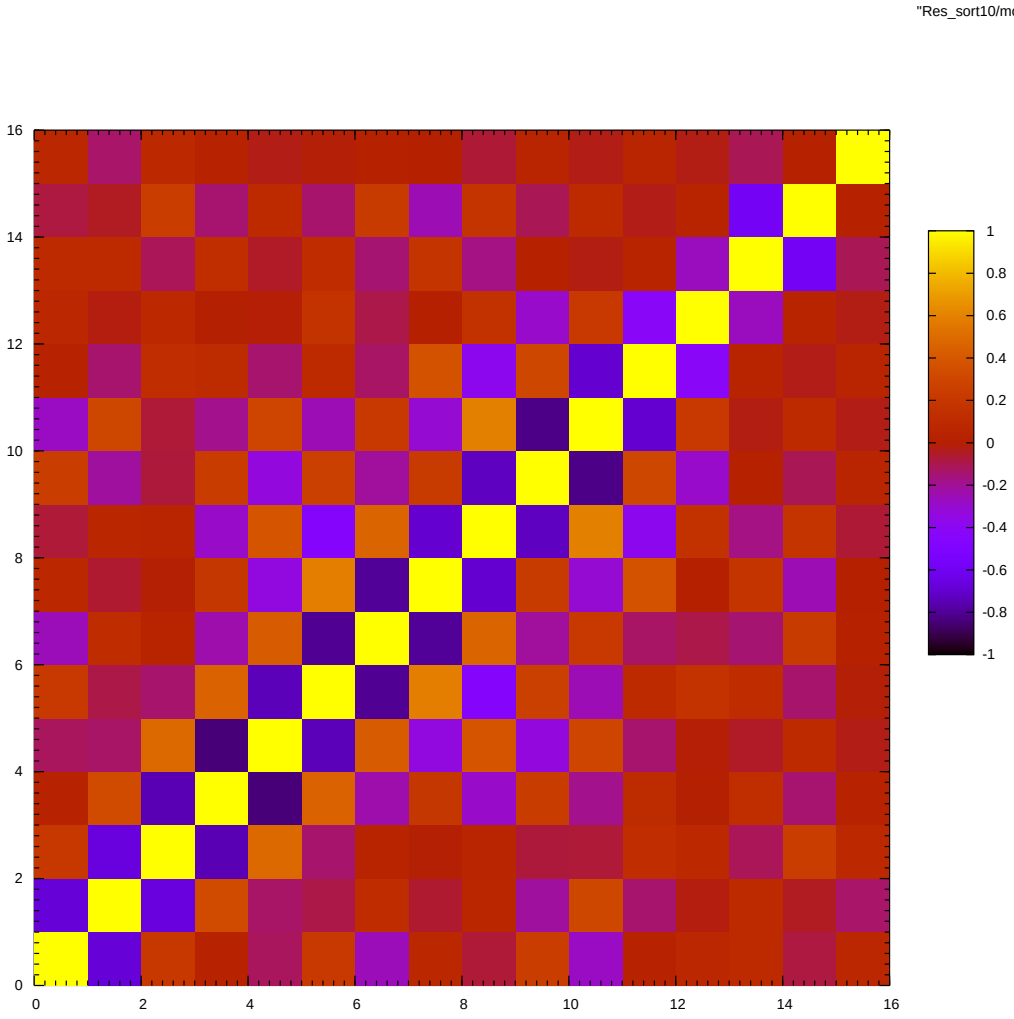

Figure 5.1: An example of correlations between different pdf bins within one redshift bin.

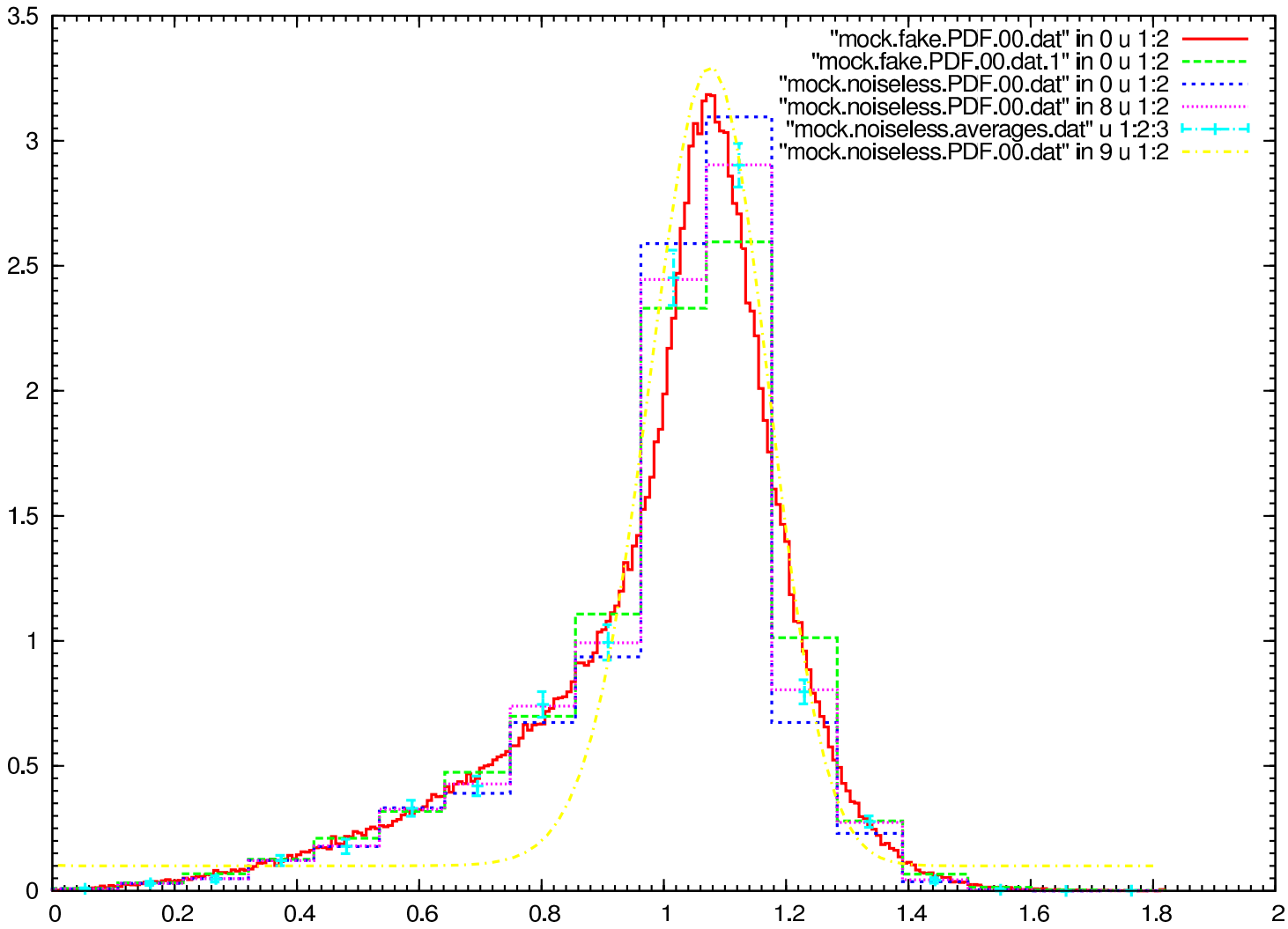

Figure 5.2: `"mock.fake.PDF.00.dat" in 0 u 1:2` is the fine-binning histogram of the noiseless MOCK data. `"mock.fake.PDF.00.dat.1" in 0 u 1:2` is our reconstruction algorithm binning histogram of the noiseless MOCK data. `"mock.noiseless.PDF.00.dat" in 0 u 1:2` is the result after the subtraction of noise under the assumption of constant probability distribution function within each bin width. `"mock.noiseless.PDF.00.dat" in 8 u 1:2` is the similiar to `"mock.noiseless.PDF.00.dat" in 0 u 1:2`, but if you assume that the probability distribution function behaves like `"mock.noiseless.PDF.00.dat" in 9 u 1:2` within each bin. `"mock.noiseless.averages.dat" u 1:2:3` shows the errors on the probability distribution function in each bin found from bootstrapping over all the quasars.

Appendix A

Inflationary Equations

In this appendix we describe the technical details of the code we ran to get the results presented in the main part of the paper. The code is given a potential $V(\phi)$ and some point ϕ_0 which lies in the observable range of wave-modes and, say, corresponds to the moment when wavelengths with $k = 0.05$ Mpc^{-1} exit the horizon. We want to find the power spectrum produced by inflation with the potential $V(\phi)$. For this purpose we first have to go backwards in time about 50 e-folds and then start the inflation there. This guarantees that the inflationary dynamics are not affected by the choice of the initial condition and we indeed have the attractor solution.

Now we evolve the universe from our "beginning of inflation" to the end of inflation, the moment which is determined by the violation of the inequality $\ddot{a} > 0$. This part is described below in the "non-perturbed inflationary equations" section. Usually we require 50 to 70 e-folds between ϕ_0 and the end of inflation.

After we already have the complete background history of the evolution of the universe during the inflationary stage of the expansion, we can start working out the evolution of the perturbations during inflation, as discussed in the second part of the appendix.

A.1 Non-perturbed inflationary equations

The unperturbed dynamics of inflation are described by the equation of motion of the scalar field ϕ with potential $V(\phi)$ in the expanding universe with the Hubble parameter $H \equiv \dot{a}/a$

$$\ddot{\phi} + 3H\dot{\phi} + V'(\phi) = 0 \tag{A.1}$$

and the Friedman equation with only the scalar field component present in the universe

$$H^2 = \frac{8\pi}{3m_{\rm pl}^2}\left[V(\phi) + \frac{1}{2}\dot{\phi}^2\right]. \tag{A.2}$$

The equations (A.1, A.2) are equivalent to the pair of Hamilton-Jacobi equation (2.1) and

$$\dot{\phi} = -\frac{m_{\rm pl}^2}{4\pi}H'(\phi). \tag{A.3}$$

The Hamilton-Jacobi equation connects the Hubble parameter and the value of the potential of the scalar field during the inflation. In the case when we know the behavior of the Hubble parameter it is easy to find the potential. The method of flow equations is entirely based on this fact. In contrast, if we know the shape of the potential and want to reconstruct the behavior of the Hubble parameter, the problem is not as simple. First of all, as for any first order differential equation, we would like to have an initial condition $H_0 = H(\phi_0)$. Due to the attractor nature of the equation (2.1) its solution does not really depend on the initial condition H_0 (we have found from numerical simulations that one needs about 6 e-folds to forget the history). Thus it does not really matter which initial condition we choose.

Hamilton-Jacobi equation requires that

$$H^2(\phi) \geq \frac{8\pi}{3m_{\rm pl}^2}V(\phi). \tag{A.4}$$

If we are going to use a method such as Runge-Kutta for the integration of the differential equation(2.1), we might try values of H which would violate the inequality (A.4).

To avoid this complication, we reparametrize our equation using a new function $\delta(\phi)$ so that

$$H^2(\phi) = \frac{8\pi}{3m_{\rm pl}^2}V(\phi)\left(1 + e^{\delta(\phi)}\right). \tag{A.5}$$

Then substituting our new definition into equation (2.1) we get

$$H'(\phi) = -\frac{4\pi\sqrt{2}}{m_{\rm pl}^2}\sqrt{V(\phi)}e^{\delta(\phi)/2}. \tag{A.6}$$

Combining this with the expression for H' obtained from the direct differentiation of H in (A.5), we get a differential equation for $\delta'(\phi)$

$$\delta' = -\sqrt{1+e^{-\delta}}\left[\frac{V'}{V}\sqrt{1+e^{-\delta}} + \frac{4\sqrt{3\pi}}{m_{\rm pl}}\right]. \tag{A.7}$$

This equation is much more pleasant to deal with numerically than equation (2.1), since it does not have a weird boundary for δ, as H did before. One can also check the attractor nature of the equation (A.7), that it does not remember the prior history. We see now that in the case when the potential is changing slowly $\delta' \approx 0$ and we have

$$e^{\delta} = \left[\frac{48\pi}{m_{\rm pl}^2\left(V'/V\right)^2} - 1\right]^{-1} \approx \frac{m_{\rm pl}^2}{48\pi}\left(\frac{V'}{V}\right)^2. \tag{A.8}$$

We can use this approximate solution of the equation as the initial condition for our differential equation since it is quite close to the true solution and it will make our numerical solution evolve into the attractor solution faster.

One can check that the expressions for ϵ_H, η_H and ${}^2\xi_H$ are given by the following formulae

$$\epsilon = \frac{m_{\rm pl}^2}{4\pi}\left(\frac{H'}{H}\right)^2 = \frac{3}{1+e^{-\delta}}, \tag{A.9}$$

$$\begin{aligned}\eta &= \frac{m_{\rm pl}^2}{4\pi}\frac{H''}{H} \\ &= 3 + \frac{m_{\rm pl}}{4}\sqrt{\frac{3}{\pi}}\frac{V'}{V}\frac{1}{\sqrt{e^{\delta}(1+e^{\delta})}},\end{aligned} \tag{A.10}$$

$$\begin{aligned}{}^2\xi &= \frac{m_{\rm pl}^4}{16\pi^2}\frac{H'H'''}{H^2} \\ &= 3(\epsilon+\eta) - \eta^2 - \frac{3m_{\rm pl}^2}{8\pi}\frac{V''}{V}\frac{1}{1+e^{\delta}}.\end{aligned} \tag{A.11}$$

From these expressions we can expect that in general ϵ and η are continuous functions, whereas ${}^2\xi$ does not have to be continuous at points where V'' is not continuous.

The condition for inflation to take place ($\ddot{a} > 0$) follows from the derivative of the Friedman equation

$$\frac{\ddot{a}}{a} = \frac{8\pi}{3m_{\rm pl}^2}\left[V(\phi) - \dot{\phi}^2\right] = H^2(\phi)(1-\epsilon), \tag{A.12}$$

or

$$\frac{\ddot{a}}{a} = \frac{8\pi}{3m_{\rm pl}^2}\left[V(\phi) - \frac{m_{\rm pl}^4}{16\pi^2}\left(H'(\phi)\right)^2\right] = \frac{8\pi}{3m_{\rm pl}^2}V(\phi)(1-2e^{\delta}). \tag{A.13}$$

The first of these two equations implies that the end of inflation happens when the inequality $\epsilon < 1$ is violated. The same thing occurs when the inequality $\delta < -\ln 2$ is violated in the second equation. The latter also means that the inflation continues while the kinetic energy of the inflaton is less than half of its potential energy

$$\frac{K}{\Pi} = \frac{\dot{\phi}^2/2}{V(\phi)} = e^{\delta(\phi)} < \frac{1}{2}. \tag{A.14}$$

Thus we come to a physical definition of our parameter $e^{\delta(\phi)}$ as the ratio of the kinetic energy $\dot{\phi}^2/2$ to the potential energy $V(\phi)$.

In the next subsection we will be working with inflationary perturbations and it will not be very convenient for us to work with the value of the scalar field ϕ as an independent variable. For this purpose we will use the number of e-folds defined as

$$\tilde{N} = \ln\frac{(aH)}{(aH)_0}. \tag{A.15}$$

Note that this is the actual number of e-folds and is not the same as $N = \ln(a/a_0)$. The connection between $\tilde{N}$ and ϕ is determined through the derivative

$$\frac{d\tilde{N}}{d\phi} = \frac{2\sqrt{\pi}}{m_{\rm pl}}\frac{1-\epsilon(\phi)}{\sqrt{\epsilon(\phi)}}. \tag{A.16}$$

We are almost done describing the background evolution of the universe, except we have not yet chosen the initial value of the scalar field ϕ_i. We only have the value ϕ_0 which corresponds to the moment when the mode $k = 0.05$ Mpc^{-1} exits the horizon. We want to move backwards in time for about 50 e-folds. Equation (A.7) has an attractor behavior

only when we are moving in the positive direction along the ϕ-axis. It diverges from the attractor solution in the negative direction. As a useful trick, let us modify equation (2.1) to the following form

$$[H'(\phi)]^2 = \frac{12\pi}{m_{\rm pl}^2}\left[\frac{8\pi}{3m_{\rm pl}^2}V(\phi) - H^2(\phi)\right]. \tag{A.17}$$

In this form, when we move backwards in time the value of $H(\phi)$ is bound by the value of $\sqrt{8\pi V/3m_{\rm pl}^2}$ from the top and the solution cannot diverge. In addition we temporarily redefine $\delta(\phi)$ to satisfy

$$H^2(\phi) = \frac{8\pi}{3m_{\rm pl}^2}V(\phi)(1 - e^{\delta(\phi)}). \tag{A.18}$$

Thus we get an equation analogous to the equation (A.7)

$$\delta' = \sqrt{1 - e^{-\delta}}\left[\frac{V'}{V}\sqrt{1 - e^{-\delta}} + \frac{4\sqrt{3\pi}}{m_{\rm pl}}\right]. \tag{A.19}$$

Equation (A.19) does not carry any physical meaning; we just use this equation to go "upwards" to the higher values of the potential, still tracking the general behavior of $V(\phi)$. If we go backwards in time 50 e-folds using (A.19) and then forward in time 50 e-folds using (A.7), we will not return to the same point ϕ_0, since the behavior of $\delta(\phi)$ in the equation (A.19) is determined by the area which is to the right of the current value of ϕ and in the equation (A.7) is determined by the area which is on the left side. Nevertheless, this method gives us a good estimate of what initial value of ϕ_i we should take.

It is also worth mentioning that this approach is not more difficult to deal with than the inflationary flow equations (2.29–2.31).

A.2 Perturbation equations

A.2.1 Scalar mode

The algorithm for finding the scalar mode primordial power spectrum is described in the main text (see equation (2.10) and below). Here we will just mention some technical details.

Equation (2.10) is not very convenient to solve in its current form. First of all we would like to set the independent variable, the conformal time τ, in such a way that $\tau \to -0$ as

inflation goes on. In this case we would be able to numerically integrate equation (2.10) up to as small values of τ as we want. But in numerical realizations we cannot really choose such an initial value of τ_i that gives us $\tau \to -0$ at the end of the inflation. Suppose that at the end of the inflation we have $\tau \to 1-0$. In this case the numerical error on τ will be of the order of 10^{-15} which is a reasonable machine precision. Hence the limit on corresponding $d\tau$ is of the same order and we can explore the range of changing the scale factor a from ~ 1 to $\sim 10^{15}$, i.e. about 35 e-folds. This might be enough, but to be safe we will use a different independent variable, the true number of e-folds $\tilde{N}$ defined by equation (A.15) which is the same as

$$d\tilde{N} = \frac{d(aH)}{aH}. \tag{A.20}$$

Then the mode equation (2.10) can be rewritten as

$$(1-a)\frac{d^2u_k}{d\tilde{N}^2} + (1+b)\frac{du_k}{d\tilde{N}} + \left[\left(\frac{k}{k_0}\right)^2 e^{-2(\tilde{N}-\tilde{N}_0)} - 2(1+c)\right] u_k = 0, \tag{A.21}$$

where coefficient a, b and c can be exactly expressed through ϵ_H, η_H and ${}^2\xi_H$ as

$$a = 2\epsilon - \epsilon^2, \tag{A.22}$$

$$b = -2\epsilon - \epsilon^2 + 2\epsilon\eta, \tag{A.23}$$

$$c = \epsilon - \frac{3}{2}\eta + \epsilon^2 - 2\epsilon\eta + \frac{1}{2}\eta^2 + \frac{1}{2}\,{}^2\xi. \tag{A.24}$$

In equation (A.21), k is the wavelength of the interest, while k_0 and $\tilde{N}_0$ are constants conveniently chosen for normalization purposes.

Further, equation (2.10) has a solution

$$u_k \propto \frac{1}{\sqrt{2k}} e^{-ik\tau} \tag{A.25}$$

at the beginning of the inflation when $\tau \to -\infty$ and $k^2 \gg \frac{1}{z}\frac{d^2z}{d\tau^2}$. We also know the approximate behavior of u_k at later times when $\tau \to -0$ and $k^2 \ll \frac{1}{z}\frac{d^2z}{d\tau^2}$:

$$u_k \propto z. \tag{A.26}$$

Thus it is natural to decompose u_k into growing and oscillating parts

$$u_k = e^{A+i\phi}, \tag{A.27}$$

where both functions A and ϕ are real functions of conformal time τ or of the true number of e-folds $\tilde{N}$. Then the equation (A.21) can be split into 4 ordinary differential equations with 2 new functions A_p and ϕ_p defined as below

$$\begin{aligned}
\frac{dA}{d\tilde{N}} &= A_p, && \text{(A.28)}\\
\frac{dA_p}{d\tilde{N}} &= \frac{-\,(k^2/k_0^2)\,e^{-2\tilde{N}} + 2(1+c) - (1+b)A_p}{1-a} \\
&\quad -(A_p^2 - \phi_p^2), && \text{(A.29)}\\
\frac{d\phi}{d\tilde{N}} &= \phi_p, && \text{(A.30)}\\
\frac{d\phi_p}{d\tilde{N}} &= -\phi_p \frac{(1+b) + 2(1-a)A_p}{1-a}. && \text{(A.31)}
\end{aligned}$$

This system of differential equations looks a bit more complicated than the single equation (2.10), but it is actually much easier to solve numerically. Indeed, at earlier times we have $dA/d\tilde{N} \equiv A_p = 0$. This instaneously gives us the initial condition on $d\phi/d\tilde{N} \equiv \phi_p$ from (A.29)

$$\phi_p^2 = \frac{(k^2/k_0^2)\,e^{-2\tilde{N}} - 2(1+c)}{1-a} \tag{A.32}$$

as $\tau \to -\infty$, i.e. $\tilde{N} \to -\infty$. To be consistent with the initial condition on

$$u_k \propto \frac{1}{\sqrt{2k}} e^{-ik\tau}$$

as $\tau \to -\infty$ we also require that

$$A = -\frac{1}{2}\ln k$$

as $\tilde{N} \to -\infty$. As the inflation continues, the terms

$$-\frac{k^2}{k_0^2}\frac{e^{-2\tilde{N}}}{1-a}$$

and ϕ_p^2 will balance each other on the right hand side of the equation (A.29) until A_p is not negligible in comparison to 1 in equation (A.31). Thus, around $\tilde{N} = \ln(k/k_0)$ the oscillating

part ϕ_p will decrease more rapidly than before, finally exponentially dropping to zero. At the same time A_p, and therefore A, start exponentially growing. The final power spectrum is given by

$$\mathcal{P}_k = \frac{k^3}{2\pi^2}\left|\frac{u_k}{z}\right|^2 \propto \frac{k^3}{2\pi^2}e^{2A_k}. \tag{A.33}$$

Thus we even do not need information about the phase ϕ and we can freely drop equation (A.30) from our system. Also while being in the stage of inflation where u_k has an oscillatory behavior, if one were to use the usual method without our substitution, one would have to find the values of u_k for at least 6 points per oscillation period. However with our substitution, we easily pass this area, which does not have any interest for us since we analytically know the behavior of u_k here, and therefore move directly to the place where we cannot solve it analytically. By our estimates this technique gives a gain of a factor of 10 in computational time, which is of particular interest if one wants to calculate the power spectrum for e.g. 100 wavemodes.

A.2.2 Tensor mode

The calculation of the tensor mode power spectrum of perturbations is absolutely analogous to the one for scalars, except instead of equation (2.10) one has to solve

$$\frac{d^2u_k}{d\tau^2} + \left(k^2 - \frac{1}{a}\frac{d^2a}{d\tau^2}\right)u_k = 0 \tag{A.34}$$

with the same initial condition

$$u_k(\tau) \to \frac{1}{\sqrt{2k}}e^{-ik\tau}$$

as $\tau \to -\infty$, where a is the usual scale factor of the Friedman universe. One can show that

$$\frac{1}{a}\frac{d^2a}{d\tau^2} = 2a^2H^2\left(1 - \frac{1}{2}\epsilon\right). \tag{A.35}$$

Mode equations for the amplitude and the phase of the wave (A.28-A.31) of the tensor mode look similar except in the equations (A.22-A.24) where we have to change c to d defined as

$$d = -\frac{1}{2}\epsilon. \tag{A.36}$$

References

[1] M. Tegmark *et al.*, Astrophys. J.**606**, 702 (2004), astro-ph/0310725.

[2] D. N. Spergel *et al.*, Astrophys. J. Suppl. Ser.**148**, 175 (2003).

[3] U. Seljak, P. McDonald, and A. Makarov, Mon. Not. R. Astron. Soc.**342**, L79 (2003).

[4] A. Slosar, U. Seljak, and A. Makarov, Phys. Rev. D**69**, 123003 (2004).

[5] A. Makarov, Phys. Rev. D**72**, 083517 (2005), astro-ph/0506326.

[6] A. H. Guth, Phys. Rev. D**23**, 347 (1981).

[7] K. Sato, Mon. Not. R. Astron. Soc.**195**, 467 (1981).

[8] A. Albrecht and P. J. Steinhardt, Physical Review Letters **48**, 1220 (1982).

[9] A. Linde, Physics Letters B **108**, 389 (1982).

[10] A. A. Starobinskii, JETP Lett.**30**, 682 (1979).

[11] V. F. Mukhanov and G. V. Chibisov, JETP Lett.**33**, 532 (1981).

[12] A. H. Guth and S.-Y. Pi, Physical Review Letters **49**, 1110 (1982).

[13] J. M. Bardeen, P. J. Steinhardt, and M. S. Turner, Phys. Rev. D**28**, 679 (1983).

[14] S. W. Hawking, Physics Letters B **115**, 295 (1982).

[15] A. A. Starobinsky, Physics Letters B **117**, 175 (1982).

[16] S. Habib, A. Heinen, K. Heitmann, G. Jungman, and C. Molina-París, Phys. Rev. D**70**, 083507 (2004).

[17] S. Habib, A. Heinen, K. Heitmann, and G. Jungman, Phys. Rev. D**71**, 043518 (2005).

[18] R. Casadio, F. Finelli, M. Luzzi, and G. Venturi, Phys. Rev. D**71**, 043517 (2005).

[19] L. Wang, V. F. Mukhanov, and P. J. Steinhardt, Phys. Lett. B**414**, 18 (1997).

[20] S. M. Leach, A. R. Liddle, J. Martin, and D. J. Schwarz, Phys. Rev. D**66**, 023515 (2002).

[21] L. Verde *et al.*, Astrophys. J. Suppl. Ser.**148**, 195 (2003).

[22] U. Seljak *et al.*, Phys. Rev. D**71**, 103515 (2005).

[23] H. V. Peiris *et al.*, Astrophys. J. Suppl. Ser.**148**, 213 (2003).

[24] M. Kawasaki, M. Yamaguchi, and J. Yokoyama, Phys. Rev. D**68**, 023508 (2003).

[25] D. J. Chung, G. Shiu, and M. Trodden, Phys. Rev. D**68**, 063501 (2003).

[26] S. Dodelson and E. Stewart, Phys. Rev. D**65**, 101301 (2002).

[27] A. R. Liddle and D. H. Lyth, editors, *Cosmological inflation and large-scale structure*, 2000.

[28] A. R. Liddle and D. H. Lyth, Phys. Lett. B**291**, 391 (1992).

[29] A. R. Liddle, P. Parsons, and J. D. Barrow, Phys. Rev. D**50**, 7222 (1994).

[30] D. J. Schwarz, C. A. Terrero-Escalante, and A. A. García, Phys. Lett. B**517**, 243 (2001).

[31] J. E. Lidsey *et al.*, Rev. Mod. Phys.**69**, 373 (1997).

[32] J. Martin and D. J. Schwarz, Phys. Rev. D**62**, 103520 (2000).

[33] E. D. Stewart and D. H. Lyth, Phys. Lett. B**302**, 171 (1993).

[34] E. D. Stewart and J.-O. Gong, Phys. Lett. B**510**, 1 (2001).

[35] H. Wei, R.-G. Cai, and A. Wang, Physics Letters B **603**, 95 (2004).

[36] I. J. Grivell and A. R. Liddle, Phys. Rev. D**54**, 7191 (1996).

[37] V. F. Mukhanov, JETP Lett.**41**, 493 (1985).

[38] V. F. Mukhanov, Zh. Eksp. Teor. Fiz.**94**, 1 (1988).

[39] M. Tegmark *et al.*, Phys. Rev. D**69**, 103501 (2004).

[40] A. R. Liddle, Mon. Not. R. Astron. Soc.**351**, L49 (2004).

[41] A. R. Liddle, Phys. Rev. D**68**, 103504 (2003).

[42] A. A. Starobinskii, Pis'ma Zh. Eksp. Teor. Fiz.**55**, 477 (1992).

[43] W. H. Kinney, Phys. Rev. D**66**, 083508 (2002).

[44] C. Chen, B. Feng, X. Wang, and Z. Yang, Classical and Quantum Gravity **21**, 3223 (2004).

[45] K. Abazajian, K. Kadota, and E. D. Stewart, ArXiv Astrophysics e-prints (2005), arXiv:astro-ph/0507224.

[46] K. M. Huffenberger, U. Seljak, and A. Makarov, Phys. Rev. D**70**, 063002 (2004), astro-ph/0404545.

[47] U. Seljak *et al.*, Phys. Rev. D**71**, 043511 (2005).

[48] U. Seljak, A. Makarov, P. McDonald, and H. Trac, ArXiv Astrophysics e-prints (2006), astro-ph/0602430.

[49] N. Padmanabhan *et al.*, ArXiv Astrophysics e-prints (2006), astro-ph/0605302.

[50] N. Christensen, R. Meyer, L. Knox, and B. Luey, Classical and Quantum Gravity **18**, 2677 (2001), astro-ph/0103134.

[51] L. Knox, N. Christensen, and C. Skordis, Astrophys. J. Lett.**563**, L95 (2001), astro-ph/0109232.

[52] A. Lewis and S. Bridle, Phys. Rev. D**66**, 103511 (2002), astro-ph/0205436.

[53] A. Gelman and D. B. Rubin, Stat. Sci. **7**, 457 (1992).

[54] U. Seljak and M. Zaldarriaga, Astrophys. J.**469**, 437+ (1996).

[55] W. Hu, U. Seljak, M. White, and M. Zaldarriaga, Phys. Rev. D**57**, 3290 (1998).

[56] A. Kosowsky, A. Mack, and T. Kahniashvili, Phys. Rev. D**66**, 024030 (2002), astro-ph/0111483.

[57] G. Hinshaw *et al.*, Astrophys. J. Suppl. Ser.**148**, 135 (2003).

[58] G. Efstathiou, Mon. Not. R. Astron. Soc.**348**, 885 (2004).

[59] C. L. Bennett *et al.*, Astrophys. J. Suppl. Ser.**148**, 97 (2003).

[60] H. Ebeling *et al.*, Mon. Not. R. Astron. Soc.**281**, 799 (1996), astro-ph/9602080.

[61] N. Afshordi, Y.-S. Loh, and M. A. Strauss, Phys. Rev. D**69**, 083524 (2004), astro-ph/0308260.

[62] T. H. Jarrett *et al.*, Astron. J.**119**, 2498 (2000), astro-ph/0004318.

[63] J. M. Diego, J. Silk, and W. Sliwa, Mon. Not. R. Astron. Soc.**346**, 940 (2003), astro-ph/0302268.

[64] S. L. Snowden *et al.*, Astrophys. J.**485**, 125 (1997).

[65] P. Fosalba, E. Gaztañaga, and F. J. Castander, Astrophys. J. Lett.**597**, L89 (2003).

[66] K. Abazajian *et al.*, Astron. J.**126**, 2081 (2003).

[67] C. Hernández-Monteagudo and J. A. Rubiño-Martín, Mon. Not. R. Astron. Soc.**347**, 403 (2004), astro-ph/0305606.

[68] M. Tegmark, A. de Oliveira-Costa, and A. J. Hamilton, Phys. Rev. D**68**, 123523 (2003).

[69] A. D. Myers, T. Shanks, P. J. Outram, W. J. Frith, and A. W. Wolfendale, Mon. Not. R. Astron. Soc.**347**, L67 (2004), astro-ph/0306180.

[70] S. J. Maddox, G. Efstathiou, W. J. Sutherland, and J. Loveday, Mon. Not. R. Astron. Soc.**243**, 692 (1990).

[71] G. O. Abell, H. G. Corwin, Jr., and R. P. Olowin, Astrophys. J. Suppl. Ser.**70**, 1 (1989).

[72] E. Komatsu and U. Seljak, Mon. Not. R. Astron. Soc.**336**, 1256 (2002).

[73] C. L. Bennett *et al.*, Astrophys. J. Suppl. Ser.**148**, 1 (2003).

[74] A. Kogut *et al.*, Astrophys. J. Suppl. Ser.**148**, 161 (2003).

[75] A. C. Pope *et al.*, Astrophys. J.**607**, 655 (2004), astro-ph/0401249.

[76] W. J. Percival *et al.*, Mon. Not. R. Astron. Soc.**327**, 1297 (2001), astro-ph/0105252.

[77] A. G. Riess *et al.*, Astrophys. J.**607**, 665 (2004), astro-ph/0402512.

[78] R. A. Knop *et al.*, Astrophys. J.**598**, 102 (2003), astro-ph/0309368.

[79] J. Khoury, P. J. Steinhardt, and N. Turok, Physical Review Letters **91**, 161301 (2003), astro-ph/0302012.

[80] J. Khoury, B. A. Ovrut, P. J. Steinhardt, and N. Turok, Phys. Rev. D**64**, 123522 (2001).

[81] R. A. C. Croft, D. H. Weinberg, N. Katz, and L. Hernquist, Astrophys. J.**495**, 44 (1998).

[82] P. McDonald *et al.*, ArXiv Astrophysics e-prints (2004), arXiv:astro-ph/0405013.

[83] D. G. York *et al.*, Astron. J.**120**, 1579 (2000).

[84] J. E. Gunn *et al.*, Astron. J.**116**, 3040 (1998).

[85] K. Abazajian *et al.*, Astron. J.**128**, 502 (2004), astro-ph/0403325.

[86] R. A. C. Croft *et al.*, Astrophys. J.**581**, 20 (2002).

[87] P. McDonald *et al.*, Astrophys. J.**543**, 1 (2000).

[88] T.-S. Kim, M. Viel, M. G. Haehnelt, R. F. Carswell, and S. Cristiani, Mon. Not. R. Astron. Soc.**347**, 355 (2004), astro-ph/0308103.

[89] P. McDonald *et al.*, Astrophys. J.**635**, 761 (2005), astro-ph/0407377.

[90] P. McDonald, U. Seljak, R. Cen, P. Bode, and J. P. Ostriker, Mon. Not. R. Astron. Soc.**360**, 1471 (2005), astro-ph/0407378.

[91] Y. Fukuda *et al.*, Physical Review Letters **81**, 1158 (1998).

[92] S. I. Alekhin and J. Blumlein, Phys. Lett. **B594**, 299 (2004), hep-ph/0404034.

[93] Q. R. Ahmad *et al.*, Physical Review Letters **87**, 071301 (2001).

[94] W. Hu, D. J. Eisenstein, and M. Tegmark, Physical Review Letters **80**, 5255 (1998), astro-ph/9712057.

[95] C. Athanassopoulos *et al.*, Physical Review Letters **77**, 3082 (1996).

[96] S. Hannestad, Journal of Cosmology and Astro-Particle Physics **5**, 4 (2003).

[97] S. Hatton and S. Cole, Mon. Not. R. Astron. Soc.**310**, 1137 (1999), astro-ph/9905186.

[98] L. Verde *et al.*, Mon. Not. R. Astron. Soc.**335**, 432 (2002).

[99] H. Hoekstra, L. van Waerbeke, M. D. Gladders, Y. Mellier, and H. K. C. Yee, Astrophys. J.**577**, 604 (2002).

[100] E. S. Sheldon *et al.*, Astron. J.**127**, 2544 (2004), astro-ph/0312036.

[101] A. C. S. Readhead *et al.*, ArXiv e-print astro-ph/0402359 (2004), astro-ph/0402359.

[102] R. Rebolo *et al.*, ArXiv e-print astro-ph/0402466 (2004), astro-ph/0402466.

[103] C. L. Kuo *et al.*, High Resolution Observations of the CMB Power Spectrum with ACBAR, eprint arXiv:astro-ph/0212289, 2002.

[104] P. McDonald *et al.*, Astrophys. J.**562**, 52 (2001).

[105] T.-S. Kim, M. Viel, M. G. Haehnelt, R. F. Carswell, and S. Cristiani, Mon. Not. R. Astron. Soc.**347**, 355 (2004), astro-ph/0308103.

[106] M. Zaldarriaga, Phys. Rev. D**55**, 1822 (1997), astro-ph/9608050.

[107] J. N. Bahcall, M. C. Gonzalez-Garcia, and C. Peña-Garay, Phys. Rev. C**66**, 035802 (2002), hep-ph/0204194.

[108] H. V. Klapdor-Kleingrothaus, First evidence for neutrinoless double beta decay, in *Identification of Dark Matter*, edited by N. J. C. Spooner and V. Kudryavtsev, pp. 577–588, 2003.

[109] M. Maltoni, T. Schwetz, M. A. Tórtola, and J. W. F. Valle, Nuclear Physics B Proceedings Supplements **114**, 203 (2003).

[110] A. Pierce and H. Murayama, Physics Letters B **581**, 218 (2004), hep-ph/0302131.

[111] R. Stefanski, Nuclear Physics B Proceedings Supplements **110**, 420 (2002).

[112] N. Y. Gnedin and A. J. S. Hamilton, Mon. Not. R. Astron. Soc.**334**, 107 (2002).

[113] S. L. Bridle, O. Lahav, J. P. Ostriker, and P. J. Steinhardt, Science **299**, 1532 (2003), astro-ph/0303180.

[114] W. L. Freedman *et al.*, Astrophys. J.**553**, 47 (2001).

[115] G. A. Tammann, A. Sandage, and A. Saha, H_0 from Type Ia supernovae, in *A decade of Hubble Space Telescope science.*, pp. 222–+, 2003.

[116] Y. Wang and M. Tegmark, ArXiv Astrophysics e-prints (2004), astro-ph/0403292.

[117] R. R. Caldwell, Physics Letters B **545**, 23 (2002), astro-ph/9908168.

[118] P. J. Steinhardt, L. Wang, and I. Zlatev, Phys. Rev. D**59**, 123504 (1999), astro-ph/9812313.

[119] E. V. Linder, Physical Review Letters **90**, 091301 (2003), astro-ph/0208512.

[120] R. Mandelbaum, P. McDonald, U. Seljak, and R. Cen, Mon. Not. R. Astron. Soc.**344**, 776 (2003).

[121] P. J. Steinhardt and N. Turok, Science **296**, 1436 (2002).

[122] A. Linde, Phys. Rev. D**49**, 748 (1994).

[123] A. R. Liddle and S. M. Leach, Phys. Rev. D**68**, 103503 (2003), astro-ph/0305263.

[124] S. Dodelson and L. Hui, Physical Review Letters **91**, 131301 (2003), astro-ph/0305113.

[125] A. Kosowsky and M. S. Turner, Phys. Rev. D**52**, 1739 (1995).

[126] S. Dodelson, W. H. Kinney, and E. W. Kolb, Phys. Rev. D**56**, 3207 (1997), astro-ph/9702166.

[127] D. H. Lyth and A. A. Riotto, Phys. Rep.**314**, 1 (1999).

[128] A. D. Linde, Journal of Experimental and Theoretical Physics Letteres **38**, 176 (1983).

[129] N. Arkani-Hamed, H.-C. Cheng, P. Creminelli, and L. Randall, Physical Review Letters **90**, 221302 (2003), hep-th/0301218.

[130] G. Dvali, Q. Shafi, and R. Schaefer, Physical Review Letters **73**, 1886 (1994), hep-ph/9406319.

[131] A. Linde and A. Riotto, Phys. Rev. D**56**, 1841 (1997), hep-ph/9703209.

[132] N. Arkani-Hamed, P. Creminelli, S. Mukohyama, and M. Zaldarriaga, Journal of Cosmology and Astro-Particle Physics **4**, 1 (2004), hep-th/0312100.

[133] P. McDonald *et al.*, Astrophys. J. Suppl. Ser.**163**, 80 (2006), astro-ph/0405013.